Using Large-Scale Additive Manufacturing for Wind Turbine Blade Core Structures

William Scott Carron, Dave Snowberg, Paul Murdy, and Scott Hughes

National Renewable Energy Laboratory

NREL is a national laboratory of the U.S. Department of Energy
Office of Energy Efficiency & Renewable Energy
Operated by the Alliance for Sustainable Energy, LLC

This report is available at no cost from the National Renewable Energy Laboratory (NREL) at www.nrel.gov/publications.

Contract No. DE-AC36-08GO28308

Technical Report
NREL/TP-5000-85673
August 2023

Using Large-Scale Additive Manufacturing for Wind Turbine Blade Core Structures

William Scott Carron, Dave Snowberg, Paul Murdy, and Scott Hughes

National Renewable Energy Laboratory

Suggested Citation
Carron, William Scott, Dave Snowberg, Paul Murdy, Scott Hughes. 2023. *Using Large-Scale Additive Manufacturing for Wind Turbine Blade Core Structures*. Golden, CO: National Renewable Energy Laboratory. NREL/TP-5000-85673. https://www.nrel.gov/docs/fy23osti/85673.pdf.

NREL is a national laboratory of the U.S. Department of Energy
Office of Energy Efficiency & Renewable Energy
Operated by the Alliance for Sustainable Energy, LLC

This report is available at no cost from the National Renewable Energy Laboratory (NREL) at www.nrel.gov/publications.

Contract No. DE-AC36-08GO28308

Technical Report
NREL/TP-5000-85673
August 2023

National Renewable Energy Laboratory
15013 Denver West Parkway
Golden, CO 80401
303-275-3000 • www.nrel.gov

NOTICE

This work was authored by the National Renewable Energy Laboratory, operated by Alliance for Sustainable Energy, LLC, for the U.S. Department of Energy (DOE) under Contract No. DE-AC36-08GO28308. Funding provided by the U.S. Department of Energy Office of Energy Efficiency and Renewable Energy Wind Energy Technologies Office. The views expressed herein do not necessarily represent the views of the DOE or the U.S. Government.

Acknowledgments

The authors would like to thank:

- Stephen Nolet (senior director at TPI Composites) and Jeremey Haight (principal engineer at Vestas AS), for providing feedback on the techno-economic modeling assumptions.

- The industry advisory committee for their time and valuable feedback

- Brian Post, Vidya Kishore, Chris Hershey, and Amiee Jackson (Oak Ridge National Laboratory) for their assistance with the interlaboratory loan of the American Society for Testing and Materials C273 test fixture, as well as for providing the three-dimensional-printed thermoplastic samples printed at the Manufacturing Demonstration Facility and for their assistance with acquiring the three-dimensional-printed thermoset panels printed with Polynt S.p.A. feedstock.

List of Acronyms

3D	three-dimensional
ABS	acrylonitrile butadiene styrene
ASTM	American Society for Testing and Materials
BAAM	Big Area Additive Manufacturing
BOM	bill of material
CAD	computer-aided design
CNC	computer numerical control
DLC	design load case
DOE	U.S. Department of Energy
IAC	Industry Advisory Committee
IEA	International Energy Agency
IEC	International Electrotechnical Commission
IPA	isopropyl alcohol
NREL	National Renewable Energy Laboratory
NRT	National Rotor Testbed
ORNL	Oak Ridge National Laboratory
PET	polyethylene terephthalate
PMI	polymethacrylimide
PVC	polyvinyl chloride
SAN	styrene acrylonitrile
TDS	technical data sheet
VARTM	vacuum-assisted resin transfer molding

Executive Summary

This report describes the techno-economic potential of using additive manufacturing technologies to design large wind turbine blade structures. After considering all additive technologies, the authors identified large-scale, polymer-based, material extrusion as the three-dimensional (3D) printing technology best suited to meet modern wind turbine blade manufacturing costs, cycle times, and geometric scale. Due to the lower structural performance requirements and the opportunity to reduce resin uptake mass penalties within the blade, the core material within the sandwich composite sections of the wind turbine blade is established as a logical entry point into advanced wind turbine blade manufacturing.

In this work, we considered several promising thermoplastic and thermoset-based 3D printing feedstock materials as an alternative to industry standard balsa and foam core materials. We tested the 3D-printed coupon specimens for in-plane shear strength using the ASTM C273 standard and performed a techno-economic analysis using the 3D-printed material test data to assess 3D-printed blade core technical and economic feasibility. The techno-economic analysis presents the potential of 3D-printed blade core structures to reduce blade cost and blade mass, limit resin uptake in the blade core, and eliminate core storage and staging costs at the blade manufacturing site. The analysis also compares 3D-printed core materials against conventional balsa and foam core materials in both their base state as well as in their infused or manufactured state.

We tested 3D printed coupon specimens comprised of Techmer PM acrylonitrile-butadiene-styrene-based Electrafil J-1200/CF/20 thermoplastic feedstock, and Polynt S.p.A. vinyl-ester-based PRD-EX1631 and PRD-EX1631-LS thermoset feedstocks. Preliminary results showed a significantly lower specific shear strength for the 3D-printed coupon specimens in comparison to conventional balsa core. Specifically, the Electrafil J-1200/CF/20, PRD-EX1631, and PRD-EX1631-LS 3D-printed materials tested showed a decrease of 77.6%, 71.0%, and 88.8%, respectively, in comparison to balsa. In comparison to the specific shear strength of resin infused balsa, incorporating the manufacturing induced mass penalties, the Electrafil J-1200/CF/20, PRD-EX1631, and PRD-EX1631-LS 3D-printed materials showed a decrease of 67.3%, 60.1%, and 84.5%, respectively. Comparisons between the 3D-printed materials and conventional foam cores used in wind turbine blades showed comparable infused specific shear strengths only between the 3D-printed core materials and the polyethylene terephthalate foam core material.

The techno-economic analysis also compared the cost of an infused balsa core solution in the outer span of a 13-meter technology demonstrator wind turbine blade against a 3D-printed honeycomb core alternative. The 3D-printed honeycomb core solution assumes large-scale, material extrusion technologies with a feedstock based on acrylonitrile butadiene styrene (ABS). The cost of the infused balsa core solution is calculated as $209.10, whereas the cost of the ABS-based 3D-printed honeycomb core solution is calculated as $1,463.63. The significantly higher cost for the 3D-printed core solution is found to be largely attributed to the operational and labor costs associated with large-scale, polymer-based additive manufacturing.

Our research discovered new and unforeseen challenges regarding the potential of using additive manufacturing technologies to manufacture mass-critical, high-performance, and cost-constrained large wind turbine blade structures. We found challenges in the areas of additive

manufacturing technologies, material science, material property characterization, structural adhesives, and the design of 3D-printed blade core structures. In this report, we summarize these challenges, and present future research pathways.

Table of Contents

List of Figures

List of Tables

1 Introduction

This report describes the potential of using additive manufacturing technologies to design novel wind turbine blade structures. Currently, large-scale additive manufacturing technologies are being used successfully in rapid prototyping and tooling applications. Yet, advancing large-scale additive manufacturing technologies to structural applications is still a challenge. Wind turbine blade structures have significant cost, mass, and performance criteria and to be certified, very stringent strength, fatigue, and stability requirements must be met.

In this report, the authors considered all of the major additive manufacturing technologies to assess their ability to meet modern wind turbine blade manufacturing costs, cycle times, and geometric scales in addition to structural performance metrics. And within all the structural components of the wind turbine blade investigated, the core materials within the sandwich composite sections are found to be the ideal place to apply large-scale additive manufacturing technologies. This is because not only are the structural performance requirements of the core much lower than the other parts of the blade, but the current balsa and foam core solutions absorb resin during the manufacturing process adding unwanted weight to the blade. Large-scale, polymer-based, material extrusion technologies are explored to enable new core solutions that meet the stringent cost, mass, and performance metrics.

Despite the core material having comparatively lower structural performance requirements than the fiber reinforced materials of the wind turbine blade, there are still structural requirements to satisfy. Within the sandwich composite sections of the blade the core must transfer the shear load between the upper and lower fiber reinforced face sheets, maintain the distance between the face sheets, and enable a structural bond between the core and face sheets. Accomplishing this using additive manufacturing is a challenge due to the layer-by-layer manufacturing process. Manufacturing in a layer-by-layer fashion with polymers creates a weak bond between deposition layers. The extent of the deficiency depends on the additive manufacturing process and the bond made between deposited beads. Historically, this interlayer weakness has not been a concern for large-scale additive manufacturing technologies, as rapid prototypes are primarily for visualization purposes, and tooling applications can be strengthened through additional post processing techniques such as post tensioning, over laminating, and structural adhesives. However, as these additive manufacturing technologies advance from rapid prototyping and tooling applications into high performance wind turbine blade structures the inherent inter-layer weakness must be well understood.

To advance three-dimensional (3D) printing technologies and expand polymer-based extrusion capabilities to large-scale, load-carrying, mass-critical, high-performance structures, we conducted research that investigates the material science, additive manufacturing process, and economics required to enter the wind turbine blade core market. We considered several thermoplastic and thermoset 3D printing materials as an alternative to balsa and foam core solutions in a 13-meter (m) wind turbine blade. We also tested 3D-printed coupon specimens using standardized processes to characterize 3D-printed material shear strength. Furthermore, we performed a detailed techno-economic analysis to assess the technical and economic feasibility of the 3D-printed blade core.

The research identifies the potential of 3D-printed blade core structures to reduce wind turbine blade cost and mass, limit resin uptake in the blade core, and eliminate core storage costs at the manufacturing site. Furthermore, it outlines the additional research needed in 3D-printed material science and large-scale 3D-printing technologies to generate the material property data sets required by computational tools to design lightweight topology optimized wind turbine blade structures.

2 Loads Requirements

2.1 Introduction

The loads used to design the 3D-printed blade core are based on the 13-m U.S. Department of Energy (DOE) National Rotor Testbed (NRT) wind turbine blade. The 13-m blade is much smaller than today's wind turbine blades; however, the thickness of the sandwich composite sections are still found in panel sections of modern wind turbine blades (Bortolotti et al. 2019a). Thus, despite the growth in wind turbine blade size, research on the 13-m blade core thicknesses of 6.35 millimeters (mm) and 12.70 mm applies to both existing blades as well as those that are printed with large-scale, polymer-based, 3D-printing technologies.

In addition, designing a 3D-printed core around the 13-m NRT platform continues to advance DOE research in blade manufacturing and structural testing technologies. Specifically, using the 13-m blade platform builds on previous research conducted by DOE's Wind Energy Technologies Office on large-scale, 3D-printed 13-m blade mold manufacturing (shown in Figure 1) and large-scale 3D- printing applications at Oak Ridge National Laboratory's Manufacturing Demonstration Facility (Post et al. 2017a, 2017b, 2017c). It also leverages the 13-m blade manufacturing capabilities at the National Renewable Energy Laboratory's (NREL's) Composites Manufacturing Education and Technology facility (Murray et al. 2021; Murray, Roadman, and Beach 2019), the 13-m blade structural testing capabilities at NREL's Structural Testing Laboratory (Gage, Beach, and Hughes 2021; Gage, Desmond, and Hughes 2019), and the 13-m-blade performance testing capabilities at the Sandia National Laboratories' Scaled Wind Farm Technology facility (Berg et al. 2013).

Figure 1. The 13-m 3D-printed wind turbine blade mold. ***Image from Oak Ridge National Laboratory***

Ultimate limit state loads are considered in the development and assessment of 3D-printed core designs. Fatigue limit state loads, as well as time- and environmental-dependent polymer effects such as creep are not considered at this low technology readiness level. The ultimate limit state loads will be used to assess 3D-printed core solutions with respect to overall blade deflections, blade strength, and blade stability.

The design loads are developed using the design load cases (DLCs) and partial safety factors detailed in International Electrotechnical Commission (IEC) 61400-1 (2005). The design loads are to be used to perform core design, core topology optimization, and blade structural analysis within computer-aided design (CAD) and finite-element analysis software.

2.2 Design Load Cases

The design loads for the 3D-printed blade core are developed using an abbreviated set of DLCs from IEC 61400-1 (2005). Specifically, they include the power production cases (i.e., DLC 1.1, DLC 1.2, DLC 1.3, DLC 1.4, and DLC 1.5) and the parked rotor cases (i.e., DLC 6.1, DLC 6.2, DLC 6.3, and DLC 6.4). Shutdown and controller fault design load cases are not considered.

2.3 Design Loads

Design loads are calculated at 16 discrete spanwise locations along the 13-m blade. Loads are derived from blade moments (Gage, Beach, and Hughes 2021; Gage, Desmond, and Hughes 2019) in the rotor coordinate system (IEC 2014) using numerical methods such as forward or backward difference along the blade span (Chapra and Canale 2010). The maximum flapwise, edgewise, and resultant design loads calculated are presented in Table 1.

Table 1. Calculated 3D-Printed Core Design Loads for the 13-m Blade

Spanwise Station	Maximum Flapwise		Maximum Edgewise		Maximum Resultant	
(m)	Fx (kilonewton [kN])	Fy (kN)	Fx (kN)	Fy (kN)	Fx (kN)	Fy (kN)
0.000	0.00	28.75	15.90	0.00	7.30	27.23
0.875	0.00	28.75	15.90	0.00	7.30	27.23
1.816	0.00	24.62	16.58	0.00	6.44	24.02
2.599	0.00	25.35	13.93	0.00	7.02	26.20
3.481	0.00	24.07	12.56	0.00	6.48	24.18
4.443	0.00	22.91	11.14	0.00	5.71	21.33
5.459	0.00	21.78	9.71	0.00	5.47	20.40
5.977	0.00	17.05	8.17	0.00	4.80	17.93
7.023	0.00	17.01	6.60	0.00	4.39	16.39
8.055	0.00	14.11	4.94	0.00	3.56	13.29
9.045	0.00	10.68	3.71	0.00	2.66	9.94
9.519	0.00	10.65	3.50	0.00	2.70	10.08
10.401	0.00	6.91	2.11	0.00	1.77	6.61
11.531	0.00	4.47	1.23	0.00	1.17	4.37
12.368	0.00	3.12	0.75	0.00	0.77	2.88
13.000	0.00	0.46	0.08	0.00	0.12	0.43

2.3.1 Blade Design Loop

The role of design loads within the blade structural design process is described in the IEC 61400-5 standard (2020) and is shown in Figure 2. The structural integrity of the 3D-printed core structure is ensured by following this flowchart. Specifically, the design loads are applied to a computational model and the core structure and blade are checked for strength, stability, and critical deflection using the finite-element method.

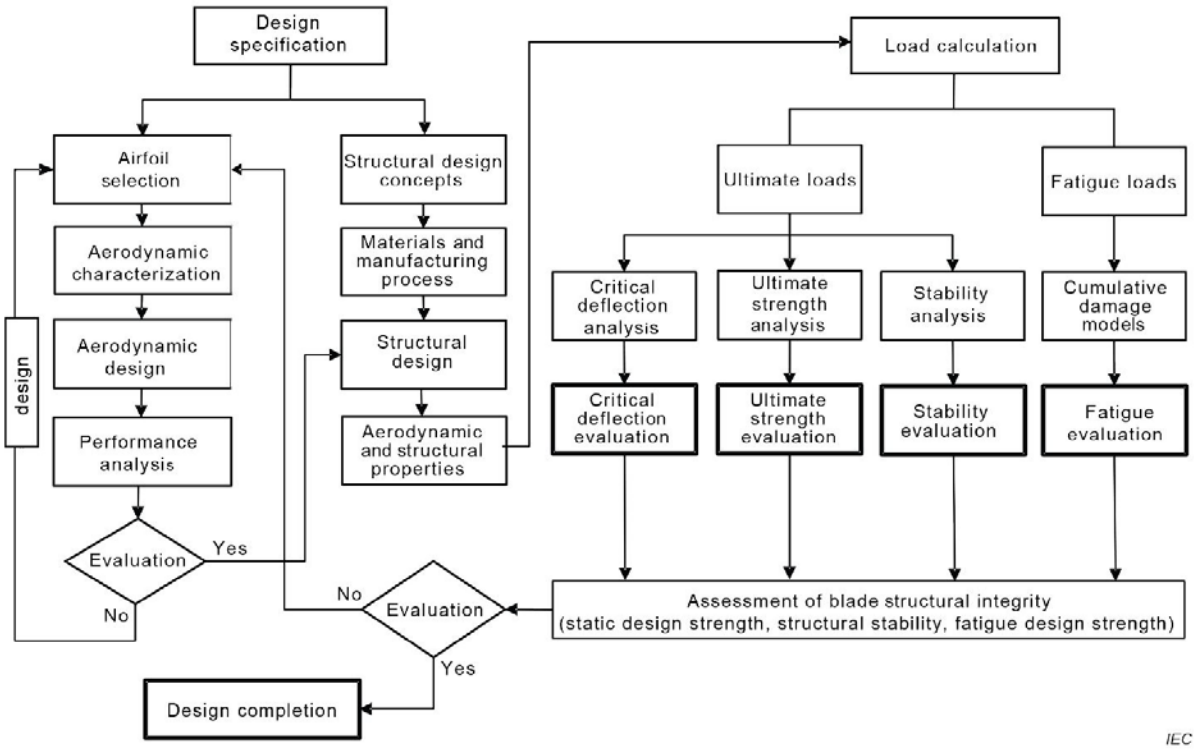

Figure 2. Typical process for design and analytical evaluation of a wind turbine blade. *Figure reproduced from IEC 61400-5 ed.1.0*[1,2]

[1] IEC 61400-5 ed.1.0 "Copyright © 2020 IEC Geneva, Switzerland. www.iec.ch"

[2] The authors thank the International Electrotechnical Commission (IEC) for permission to reproduce Information from its International Standards. All such extracts are copyright of IEC, Geneva, Switzerland. All rights reserved. Further information on the IEC is available from www.iec.ch. IEC has no responsibility for the placement and context in which the extracts and contents are reproduced by the author, nor is IEC in any way responsible for the other content or accuracy therein.

3 Structural Requirements

3.1 Introduction

Structural design requirements depend on the type of structure, loads, and expected failure modes. For lightweight or mass-constrained structures, such as wind turbine blades, there are numerous benefits to using sandwich composite structures characterized by a core material, two high-strength face sheets, and a structural adhesive holding them all together (shown in Figure 3). Historically, sandwich composite structures first emerged in the aircraft industry in the 1930s using balsa wood cores with wooden veneer face sheets. As technology advanced, the aircraft industry turned to honeycomb cores in the 1940s and 1950s as stronger and lighter, but more expensive, alternatives to balsa wood cores. Then, as the plastics industry blossomed in the 1950s and 1960s, polyvinyl chloride (PVC) and polyurethane cellular foam cores emerged, followed by cellular foam cores with variable cell structures, as alternatives to honeycomb and balsa core (Zenkert 1995). The sandwich composite sections of today's wind turbine blades comprise balsa or foam core, glass-fiber-reinforced polymer face sheets, and an epoxy structural adhesive.

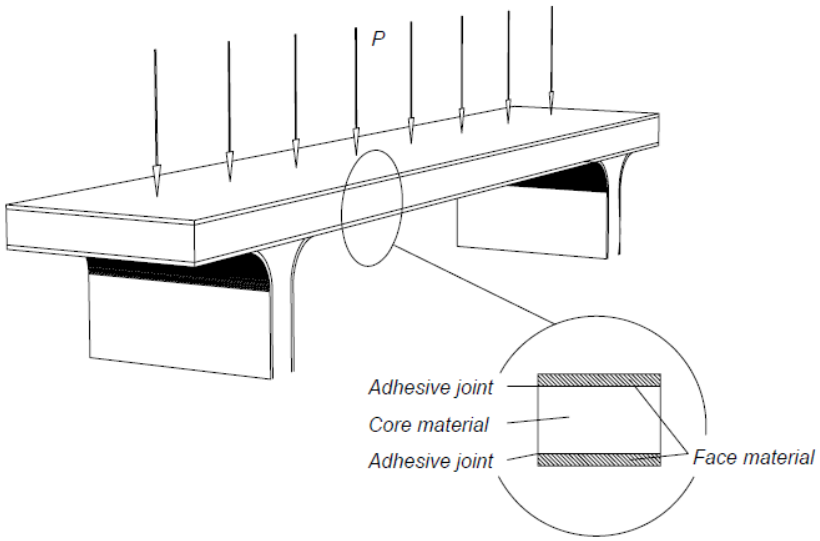

Figure 3. Sandwich structure composition. ***Image reproduced from Zenkert (1995)***

Technically, the merits of sandwich structures have been long understood. Expanding the distance between the load-carrying face sheets of a sandwich composite panel dramatically increases the flexural rigidity (D) and bending strength, as shown in Figure 3. When the core material is low density, extremely high stiffness-to-weight and strength-to-weight ratios can be achieved with an almost negligible mass penalty.

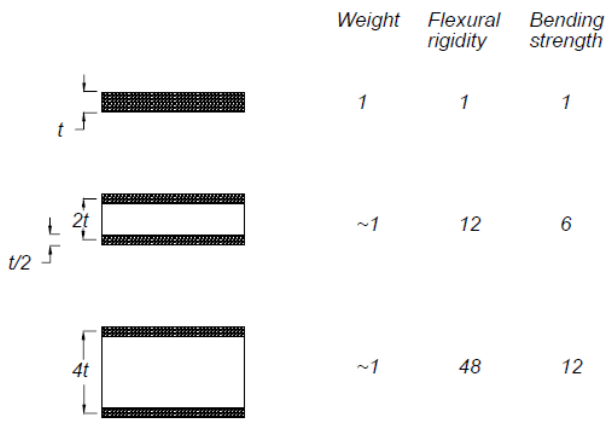

Figure 4. Effects of core thickness on flexural rigidity and bending strength. *Image reproduced from Zenkert (1995)*

Furthermore, using low-density and low-modulus core material in sandwich composite structures can efficiently concentrate the tensile and compressive bending loads in the face sheets and the transverse shear loads in the core material. The resulting tensile and compressive stress as well as the shear stress throughout the sandwich composite is shown in Figure 5 for various face-sheet and core approximations.

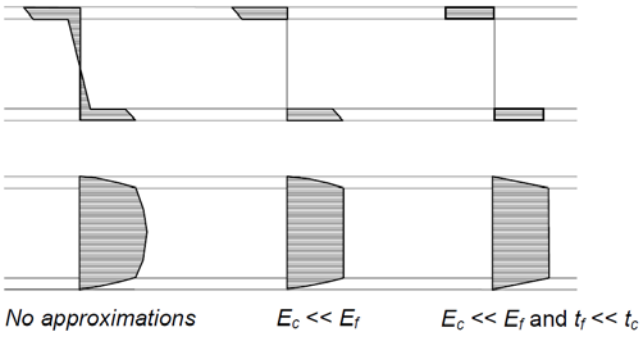

Figure 5. Tensile and compressive (top) and shear (bottom) stress distributions in a sandwich composite structure subject to bending. *Image reproduced from Zenkert (1995)*

3.2 Core Design Options

Today, sandwich composite structures are used in a broad range of applications, from low-cost shipping boxes to high-performance aircraft structures. Wind turbine blades are no exception and commonly use balsa and foam core within their sandwich composite structure sections to improve their strength-to-weight and stiffness-to-weight ratios.

Common structural core solutions include wood, honeycomb, cellular, and corrugated. Due to advancements in 3D-printing technologies, a fifth type of 3D-printed lattice-like core structures is emerging.

This new category may open advanced manufacturing pathways to implementing higher-performance core structures into wind turbine blades. As a result, this may lead to improved stiffness-to-weight and strength-to-weight ratios, lower overall cost, enhanced recyclability, reduced supply chain dependency, and increased domestic manufacturing options for next-generation wind turbine blade structures.

3.2.1 Wood Core

Derived from the fast-growing tree, Ochroma pyramidale, balsa wood is the original core material used in aerospace sandwich composite structures due to its unique properties. The wood fibers have a diameter of approximately 0.05 mm, which are aligned vertically in the direction of growth. The fibers are held together with a cellulose, hemicellulose, and lignan matrix, which provides much of the transverse shear strength (Borrega et al. 2015). Approximately 90% of the commercially produced balsa in the world is sourced from Ecuador, with the rest from Papua New Guinea. The balsa tree is typically harvested after 6 to 10 years of growth. The balsa wood is processed, and the balsa core product is sold as end grain balsa, wherein the tree is cut into cubes and attached to a scrim with the fibers aligned normal to the scrim plane, as shown in Figure 6. Density varies throughout the tree, and the balsa is cut into small blocks to provide a consistent density product. It has excellent mechanical properties and is a cost-efficient core solution. Due to the large surface area and fibrous nature, balsa bonds easily to face sheets when the sandwich composite is manufactured using a resin infusion process. In addition, the balsa core uniformly supports the face sheets, thereby allowing the structure to better maintain a surface or aerodynamic profile and prevent local buckling and indentation.

Due to these factors, balsa is found in the inner span of many modern wind turbine blades. The downside of end-grain balsa is that the resin infusion process often leads to significant resin absorption within the outer surface fibers of the balsa. This resin absorption can impose a significant mass penalty on the structure but can be mitigated to a certain extent by purchasing a higher-cost balsa core with a surface treatment. The surface treatment, typically a fast-curing resin, reduces the resin mass penalty due to the quick cure, but may reduce secondary adhesion properties when infused in the blade mold.

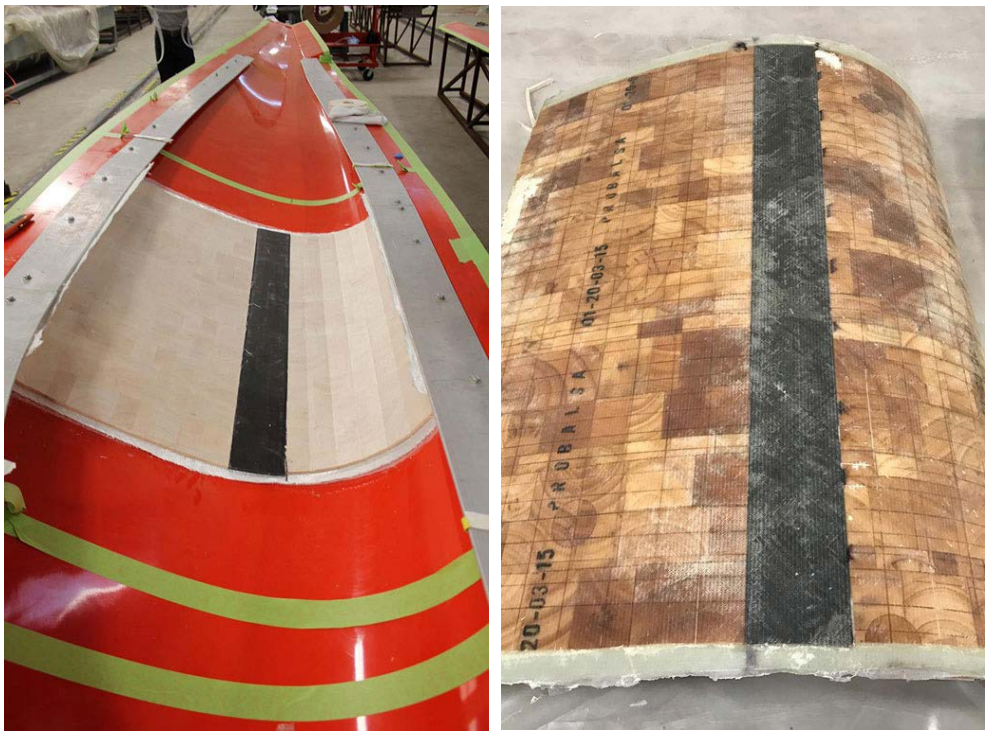

Figure 6. End grain balsa blocks attached to a scrim backing within a blade mold (left) and post infusion (right). *Photos by Ryan Beach, NREL*

3.3 Honeycomb Core

As demonstrated throughout nature, honeycomb core structures are some of the most efficient designs in terms of density, strength, and stiffness. Extremely high stiffness-to-weight and strength-to-weight ratio structures can be achieved using honeycomb cores. It is an expensive core solution when manufactured conventionally, therefore it is mainly found in high-performance aerospace structures. The expense is largely due to the process of joining the honeycomb to the face sheets, although manufacturing, cutting, forming, and curing also add expense. The most common honeycomb core cell shape is the hexagon; however, square, overexpanded, and flex core variations can be manufactured to fit the application and surface curvature as shown in Figure 7 and Figure 8. Honeycomb core materials commonly used in aerospace structures include fiber reinforced Nomex (Toray 2020a) and aluminum (Toray 2020b), such as the products manufactured by Toray Advanced Composites.

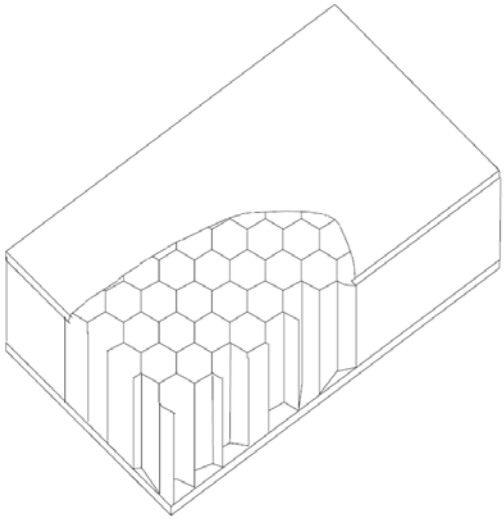

Figure 7. Hexagonal honeycomb core. ***Image reproduced from Zenkert (1995)***

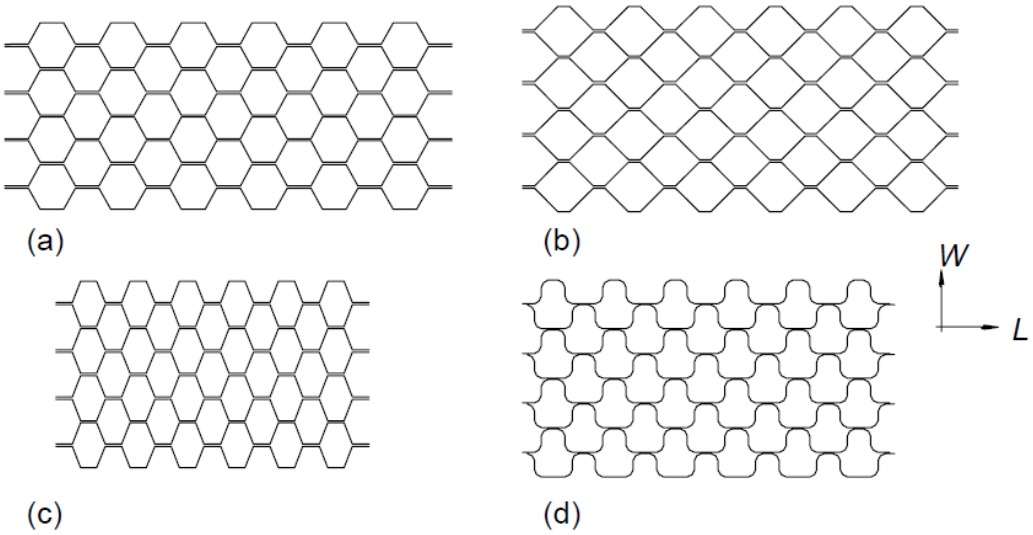

Figure 8. Common honeycomb cell shapes: (a) hexagonal, (b) square, (c) overexpanded, and (d) flex core. ***Image reproduced from Zenkert (1995)***

3.4 Cellular Core

Cellular cores are the next generation of core materials that emerged after balsa and honeycomb. Lightweight cellular cores are generally formed by mixing a thermoset or thermoplastic polymer with a blowing agent to create open-cell or closed-cell foam structures. Alternatively, syntactic foams[3] are created by including hollow or expandable microspheres. Typically, foam cores have lower mechanical properties when compared to balsa but lower cost and mass. They are also easy to form, shape, and bond to face sheets. As such, polyethylene terephthalate (PET), cross-linked PVC, and styrene acrylonitrile (SAN) foam cores can be found in the outer spans of wind turbine blades (Gurit n.d.[a]).

[3] https://en.wikipedia.org/wiki/Syntactic_foam

3.5 Corrugated Core

Corrugated cores are commonly used in the shipping and packaging industry. They are constructed of kraft paper, otherwise known as cardboard. Corrugated cardboard can be optimized for strength by varying the number of layers and flutes. Corrugated cores are low cost but also have low mechanical properties. They are not strong or stiff enough to be used in wind turbine blades.

3.6 Lattice Core

Lattice cores are commonly based on a 3D unit cell that is manufactured by repeating the pattern in all three directions. Lattice-like cores can achieve low densities and create sandwich structures with high stiffness-to-weight and strength-to-weight ratios. Unlike the other core solutions, it is challenging to manufacture lattice cores using conventional manufacturing. However, 3D-printing technologies are emerging as an advanced manufacturing method that can manufacture these complex, lightweight, lattice-like core structures (Feng et al. 2018). 3D-printed lattice cores are being used in high-end aerospace structures, biomedical structures, and high-end cooling and mixing applications. For high-end aerospace structures, powder bed fusion is a common 3D-printing technology used to manufacture this category of core materials. However, the costs and requirements associated with either metal-based or polymer-based powder bed fusion processes is currently far too expensive for wind turbine blade structures. Lower-cost, polymer-based material extrusion 3D-printing processes may enable economical structural solutions if the layer-to-layer and bead-to-bead adhesion properties can be characterized and proven to be structurally adequate for wind turbine blades.

3.7 Stiffened Panels

Finally, stiffened panels, although not technically sandwich composite structures, are considered. Stiffened panels are a sandwich composite alternative, and work by increasing panel stiffness through stiffeners attached to one side of the panel. The performance attributes of the second face sheet and core of the sandwich composite is replaced by the geometric shape of the rib-like stiffeners. Stiffeners are typically named by their geometric shape, such as a J-stiffener, T-stiffener, I-stiffener, or hat stiffener (Borrega et al. 2015). The shapes are traditionally manufactured by either sheet forming or extrusion but can now be 3D printed. On a mass basis, stiffened panels are not as structurally efficient as sandwich composites (Turner and Grande 1978), but they do have their benefits. They can be seen in applications such as aircraft fuselages, or in other applications where damage tolerance, ease of inspection, or lower manufacturing costs are a driver (Meink 1998). Modern wind turbine blades do not use stiffened panels, but rather sandwich composites to achieve their high stiffness-to-weight ratios, maintain their aerodynamic profile, prevent large deflections and tower strikes, prevent buckling modes, prevent structural failure, and enable the use of the low-cost vacuum- assisted resin transfer molding (VARTM) manufacturing process. The wind industry, however, is always adapting and subject to ever-changing energy needs. Concerns surrounding logistics, supply chain, automation, and domestic manufacturing needs are inviting new design for manufacturing strategies. Recent advancements in large-scale, polymer-based, additive manufacturing technologies, coupled with low-viscosity infusible thermoplastic resins, is attracting new research into the techno-economic benefits of 3D-printed stiffened panels in the wind industry (Bortolotti et al. 2023).

3.8 Coordinate Systems

Coordinate systems provide a basis for 3D-printed core geometries, material properties, and stresses.

3.8.1 Core Coordinate System

Sandwich core structures are commonly referenced in a core coordinate system. The coordinate system for wood, foam, and honeycomb core (U.S. Department of Defense [DOD] 1967) is described by a length axis, a width axis, and thickness axis, as shown in Figure 9. Wood- based cores are oriented around the grain direction, foam and cellular cores are oriented around the forming direction, and honeycomb cores are oriented around the ribbon direction.

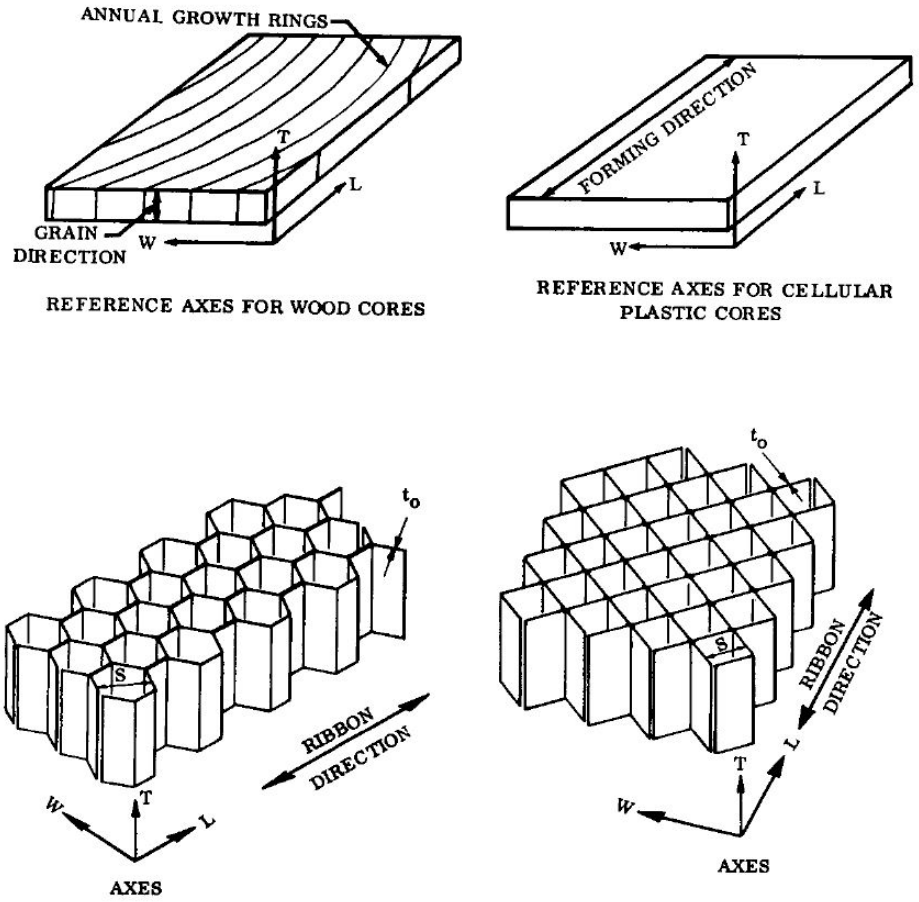

Figure 9. Axes notation for sandwich cores. ***Figure from U.S. Department of Defense (1967)***

Polymer-based feedstock for large-scale 3D printers is significantly denser than balsa and foam cores. As such, 3D-printed cores will require geometries such as a honeycomb to achieve acceptable strength-to-weight and stiffness-to-weight ratios. It is assumed that these 3D-printed geometries can be defined by the same cell geometry as honeycomb core. Honeycomb core is described by a unit cell structure that is commonly a hexagon. The cell size is defined by the cell wall thickness (t), the length of the cell wall (l), and cell size (d), as shown in Figure 10. As a result of the manufacturing process, conventionally manufactured honeycomb cores require the cell walls aligned in the ribbon axis to have a double thickness $(2t)$. In an orthotopic system, this

manufacturing effect leads to a strong direction and a weak direction within the core. The strong direction is defined by the ribbon or length (L) axis, whereas the weak direction is defined by the width (W) axis. The transverse direction is defined by the (T) axis, as shown in Figure 9. It is assumed that the toolpaths of 3D-printed cores will create a similar manufacturing-induced anisotropy or orthotropy. Balsa and foam cores are assumed to have similar properties in both the length (L) axis and width (W) axis due to their microstructures in those axes. If other coordinated systems are desired, the (L, W, T) coordinate system can be transformed to either a cartesian coordinate system (X, Y, Z) or a principal material coordinate system $(1, 2, 3)$. Finally, non-hexagonal honeycomb and 3D-printed honeycomb cores will still be described as best as possible by the (L, W, T) coordinate system where the length (L) axis is defined by the ribbon or primary bead direction.

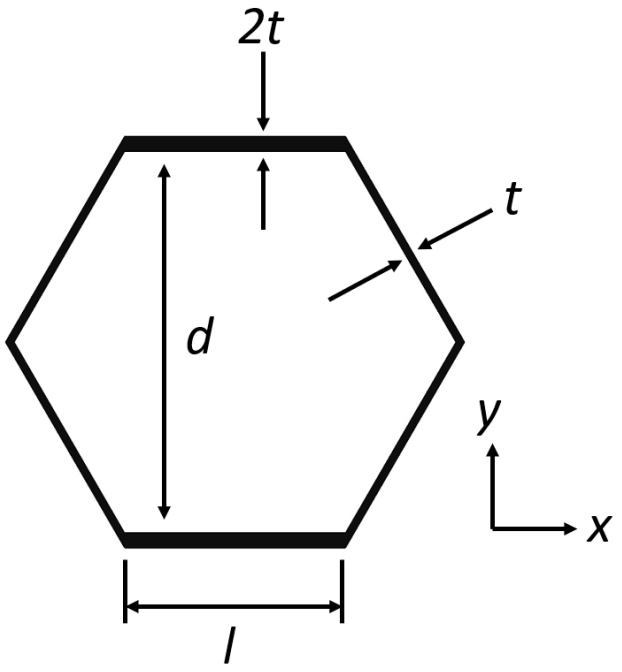

Figure 10. Honeycomb cell geometry. ***Illustration created by W.S. Carron, NREL***

3.8.2 Principal Material Coordinate System

Composite laminates use a principal material coordinate system. The face sheets in wind turbine blade sandwich composite structures are composite laminates comprising fiber and resin material. The laminate is built from individual plies. At the ply level, the principal material coordinate system is aligned with the primary fiber direction. For example, for a unidirectional ply, the 1-axis is aligned with the 0-degree fiber direction. For +/- 45-degree biaxial ply, the 1-axis is shifted 45-degrees. At the laminate level, the principal material coordinate system is commonly aligned with the primary structural load direction, which also typically aligns with the unidirectional fiber alignment within the laminate. The principal material coordinate system $(1, 2, 3)$ for a laminate face sheet is shown in Figure 11.

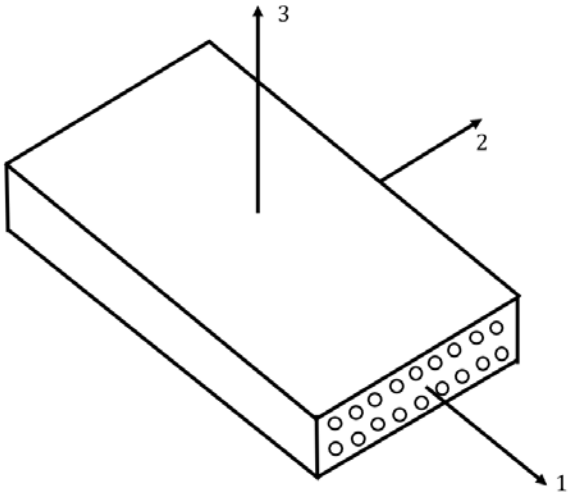

Figure 11. Principal material coordinate system. ***Illustration created by W.S. Carron, NREL***

3.8.3 Three-Dimensional Stress State

The stress state within the principal material coordinate system is defined using an infinitesimally small volume that assumes material properties are smeared over the unit volume, as shown in Figure 3.10. There are three normal stresses, $\sigma_1, \sigma_2, \sigma_3$, and six shear stresses, $\tau_{12}, \tau_{21}, \tau_{23}, \tau_{32}, \tau_{13}, \tau_{31}$. In a state of equilibrium, there are only three normal stresses, $\sigma_1, \sigma_2, \sigma_3$, and three unique shear stresses, $\tau_{12}, \tau_{23}, \tau_{13}$, as $\tau_{xy} = \tau_{yx}$. The convention is such that the first subscript defines the face normal to that axis, and the second subscript defines the direction in which the force acts.

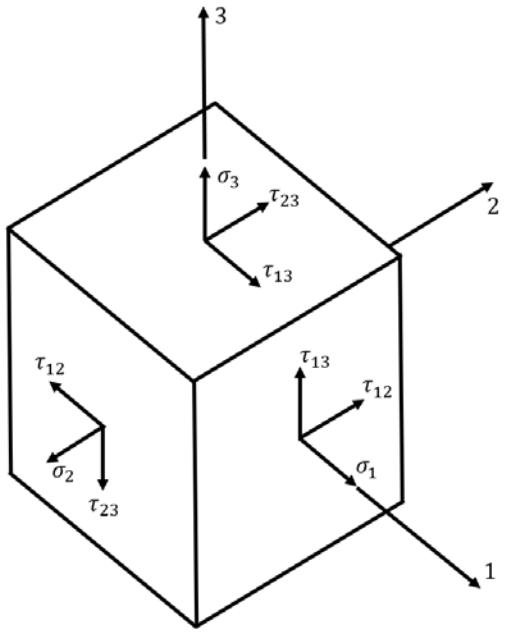

Figure 12. Stress field coordinate system. ***Illustration created by W.S. Carron, NREL***

These stress definitions are important when characterizing and comparing 3D-printed core materials to conventional core material. For example, vendors presenting shear strengths of their core materials characterize them using the American Society for Testing Materials (ASTM) C273 standard (ASTM 2020). The ASTM C273 states, "It covers the determination of shear strength parallel to the plane of the sandwich, and the shear modulus associated with strains in a plane normal to the facings." Thus, shear strength for balsa and foam cores found in the vendor technical data sheet (TDS) characterized under ASTM C273 describes the property τ_{12} in the principal material coordinate system and the property τ_{LW} in the core coordinate system.

3.9 Sandwich Composite Material Properties

To analyze sandwich composite structures using finite-element analysis, material properties are required for the core material, face-sheet material, and structural adhesive or resin.

3.9.1 Core Properties

The role of the core material is to both maintain the distance between the face sheets as well as transfer the shear loads between them. As such, shear and compressive properties are of utmost concern when considering 3D-printed core structures. Unfortunately, due to the layer-by-layer deposition, the shear strength between beads and layers is currently the least understood and characterized property in 3D-printed structures. Historically, most applications have been tooling- or prototyping-related where shear strength is not a concern. In addition, characterizing shear strength can be extremely costly, as the quality and amount of adhesion, fusion, or cross-linking between beads and layers varies significantly between 3D-printing materials and manufacturing processes.

The 13-m wind turbine blade provides the baseline for the structural design of the 3D-printed core. The sandwich structures of the blade are manufactured using 6.35 mm balsa in the outer span and 12.7 mm balsa in the inner span (Kelley 2020). The 13-m NRT blade bill of materials specifies Baltek structural end grain balsa with a density of 150 kg/m^3 (Baltek 2014). The mechanical properties of the Baltek balsa coupled with the balsa density provide the shear and compressive strength-to-weight and stiffness-to-weight targets for the design of 3D-printed core structures.

In-plane and transverse material properties are well-known for balsa, foam, and honeycomb cores. Material properties are presented by vendors in their TDS and are characterized using ASTM test standards. The TDS typically provides everything an engineer needs to perform a structural analysis. In contrast, very little, if any, material property information is provided in terms of shear for engineers designing 3D-printed structures using material extrusion. This lack of information might be attributed to rapid prototype applications that are not highly stressed or tooling applications that can utilize postprocessing techniques such as post-tensioning, structural adhesives, and overlamination to improve the shear strength. Wind turbine blades cannot afford the mass and cost penalties associated with these postprocessing techniques, nor can they design or certify blade structures without fully characterized material properties. Generally, an engineer will need a complete set of material and mechanical properties, as shown in Table 2, to perform the structural analysis required for design and certification.

Table 2. Complete Set of Material and Mechanical Properties for Sandwich Composite Core

Property	Description
ρ	Density (kilogram (kg)/cubic meter [m^3])
$\sigma_{c,1}$	Compressive strength in the 1-axis (megapascal [MPa])
$E_{c,1}$	Compressive modulus in the 1-axis (gigapascal [GPa])
$\sigma_{t,1}$	Tensile strength in the 1-axis (MPa)
$E_{t,1}$	Tensile modulus in the 1-axis (GPa)
$\sigma_{c,2}$	Compressive strength in the 2-axis (MPa)
$E_{c,2}$	Compressive modulus in the 2-axis (GPa)
$\sigma_{t,2}$	Tensile strength in the 2-axis (MPa)
$E_{t,2}$	Tensile modulus in the 2-axis (GPa)
$\sigma_{c,3}$	Compressive strength in the 3-axis (MPa)
$E_{c,3}$	Compressive modulus in the 3-axis (GPa)
$\sigma_{t,3}$	Tensile strength in the 3-axis (MPa)
$E_{t,3}$	Tensile modulus in the 3-axis (GPa)
τ_{12}	Shear strength in the 1–2 plane (MPa)
G_{12}	Shear modulus in the 1–2 plane (GPa)
τ_{13}	Shear strength in the 1–3 plane (MPa)
G_{13}	Shear modulus in the 1–3 plane (GPa)
τ_{23}	Shear strength in the 2–3 plane (MPa)
G_{23}	Shear modulus in the 2–3 plane (GPa)
v_{12}	Poisson's ratio (contraction in the 2-axis under extension in the 1-axis)
v_{13}	Poisson's ratio (contraction in the 3-axis under extension in the 1-axis)
v_{23}	Poisson's ratio (contraction in the 3-axis under extension in the 2-axis)

However, because material characterization in all three axes is both timely and costly, this full set of material and mechanical properties is reduced from 22 to a set of 7. This reduction in the material property set is based on the following assumptions. Tensile strength, as well as tensile stiffness, in both the print bead direction and transverse to the bead direction for 3D-printed polymers, will rely on publicly available and published data, such as those reported by Techmer Engineered Solutions (Duty, Drye, and Franc 2015), and need not be tested. As tensile strength in the out-of-plane direction, known as the z-direction within the 3D-printing industry, is weaker in tension than in compression, the project assumes tensile properties for both out-of-plane tension and compression. Poisson's ratio is assumed to be equal to 0.35 for all polymer and polymer-reinforced feedstock (Callister 2006). The seven outstanding 3D-printed material properties to be characterized from Table 2 are ρ, τ_{12}, G_{12}, τ_{13}, G_{13}, τ_{23}, and G_{23}.

To further reduce material characterization costs to a minimum, we established a set of three critical material and mechanical properties. This minimum set is based on the large uncertainty surrounding in-plane shear strength and transverse shear modulus and their critical role in the design of 3D-printed sandwich core structures. This shear focused set of three material and mechanical properties needed to be characterized from Table 2: ρ, τ_{12}, and G_{23}.

3.9.2 Face Sheet Properties

As the face sheets in a sandwich structure carry the bending moments in the form of tension and compression, the following set of in-plane orthotropic material properties (of the composite face sheets, as shown in Table 3), are required for the finite-element-based codes to perform the structural analysis. These material properties are commonly provided by vendors in their TDS at the ply level for specified fiber and resin volume fractions, thereby minimizing material characterization at the coupon level. The composite laminate scheme of the 13-m blade is already established and provides the baseline for the structural design of the face sheets for this project. The 13-m blade spar cap, face sheets, shear web, and root (Kelley 2020) are manufactured using combinations of Vectorply 12 ounce (oz)/square yard (yd^2) unidirectional e-glass (Vectorply n.d.[a]) and 24 oz/yd^2 biaxial e-glass (Vectorply n.d.[b]), combined with epoxy resin.

Table 3. Set of Material and Mechanical Properties for Sandwich Composite Face Sheets

Property	Description
ρ	Density (kg/m^3)
$\boldsymbol{E_1}$	Elastic modulus in the 1-axis (GPa)
$\boldsymbol{\sigma_{t,1}}$	Tensile strength in the 1-axis (MPa)
$\boldsymbol{\sigma_{c,1}}$	Compressive strength in the 1-axis (MPa)
$\boldsymbol{E_2}$	Elastic modulus in the 2-axis (GPa)
$\boldsymbol{\sigma_{t,2}}$	Tensile strength in the 2-axis (MPa)
$\boldsymbol{\sigma_{c,2}}$	Compressive strength in the 2-axis (MPa)
$\boldsymbol{G_{12}}$	Shear modulus in the 1–2 plane (GPa)
$\boldsymbol{v_{12}}$	Poisson's ratio (contraction in the 2-axis under extension in the 1-axis)
$\boldsymbol{v_{21}}$	Poisson's ratio (contraction in the 1-axis under extension in the 2-axis)

If face-sheet properties are not obtained in the vendor TDS, they can be derived from the base fiber and matrix constituent properties using the rule of mixtures. From this rule, the elastic moduli can be determined (Zenkert 1995) using:

$$E_1 = E_f v_f + E_m v_m \quad (1)$$

$$1/E_2 = v_f/E_f + v_m/E_m \quad (2)$$

where the subscripts f and m denote the fiber and matrix, respectively, and v_f and v_m are the volume fractions, which are calculated (Zenkert 1995) using:

$$v_f = V_f / V_{total} \quad (3)$$

$$v_m = V_m / V_{total} \quad (4)$$

where (V_f) and (V_m) are the volume of fiber and matrix material, respectively, and (V_{total}) is the total volume of the composite laminate. The shear modulus and Poisson's ratio can be determined (Zenkert 1995) using:

$$1/G_{12} = v_f/G_f + v_m/G_m \quad (5)$$

$$v_{12} = (v_f * v_f) + (v_m * v_m) \quad (6)$$

and the ply thickness can be determined (Zenkert 1995) using:

$$t = \sum \frac{W_i}{\rho_i} \quad (7)$$

where W_i denotes the weight per unit area and ρ_i denotes the densities of both the fiber and matrix.

3.9.3 Adhesive Properties

The adhesive bond is critical in keeping the constituents of the sandwich composite together. There are many failure modes that can impact the structural integrity of this interface, such as peel, shear, and improper surface preparation (DOD 1987). Adhesive failure modes can largely be avoided through proper joint design. Computational modeling of the adhesive is a complex analysis (Kumar and Mittal 2013; da Silva 2008). For computational analysis purposes, the adhesive is not considered, and it is assumed that the face sheets and core are connected through a bonded boundary condition. This bonding boundary condition assumes that core failure will occur before an adhesive bond failure.

In practice, obtaining a high-adhesion strength to polymers is a challenge (Hamdi 2020), and adhesive failure modes for polymer-based 3D-printed core structures are not well-understood. Vendor data do not always provide the designer with lap shear strength and peel strength data in their technical data sheets. There can also be uncertainty surrounding the structural adhesive data in the TDS and whether the strength calculated at failure was due to the adhesive or the polymer failing. Neat polymer adherends are often listed in a suppliers TDS; however, there is a lack of data for 3D-printed thermoset and thermoplastics polymers with material additives such as chopped carbon fiber and expandable microspheres, as well as chemical additives such as styrene. Lap shear strength and peel strength will need to be characterized using ASTM standards for structural adhesives on 3D-printed polymer adherends. New specialty formulations or classes of structural adhesives may need to be developed specifically for 3D-printed polymer structures. Other solutions such as polymer welding and film adhesives may need to be investigated.

3.10 Shear Deformation

Analysis of sandwich composite beam structures need to consider Timoshenko beam theory instead of Euler-Bernoulli beam theory (Zenkert 1995; Oñate 2013). This is to account for the

shear deformations in addition to the bending deformations. To assist with the forces within a sandwich structure, the sign convention, as shown in Figure 13, is used. Due to the presence of transverse shear, when the sandwich beam is subject to a bending moment, the response is described by the flexural rigidity (D) as well as the shear stiffness (S).

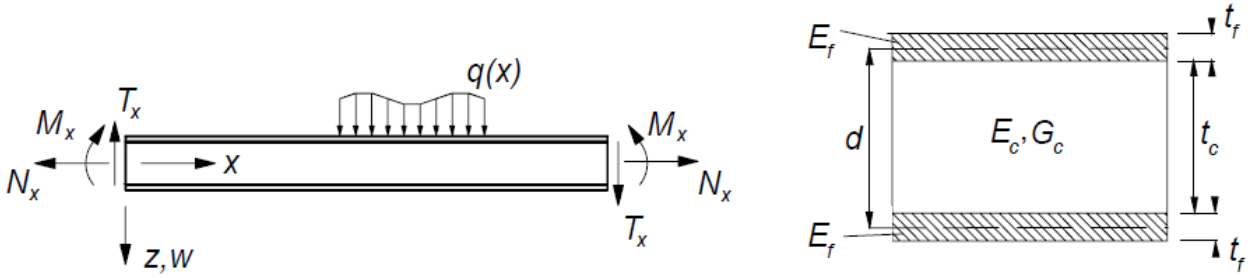

Figure 13. Sandwich composite structural and geometric nomenclature. ***Image reproduced from Zenkert (1995)***

For design purposes, the following assumptions are made to simplify the structural design of a 3D-printed core. First, the thickness of the face sheet is assumed to be much less than the thickness of the core ($t_f \ll t_c$). Second, the elastic modulus of the core is assumed to be much less than the elastic modulus of the face sheet ($E_c \ll E_f$). Under these assumptions, the complex equations defining the flexural rigidity (D) of the sandwich composite beam simplifies (Zenkert 1995) to become:

$$D = \frac{E_f * t_f * d^2}{2} \tag{8}$$

It is important to note that the units for the flexural rigidity (D) of sandwich composite plates and shells are different than the units for the flexural rigidity (EI) of beams with a fixed width. The shear stiffness of the sandwich beam (S) simplifies (Zenkert 1995) to become:

$$S = \frac{G_c * d^2}{t_c} \tag{9}$$

The bending and shear stresses in both the core and face sheets, as represented in Figure 5 also simplify (Zenkert 1995) to become:

$$\sigma_c = 0 \tag{10}$$

$$\sigma_f = \pm \frac{M_x}{t_f * d} \tag{11}$$

$$\tau_c = \frac{T_x}{d} \tag{12}$$

$$\tau_f = 0 \tag{13}$$

These calculations are handled internally within the finite-element analysis code by including shear deformation; however, they are provided for preliminary assessment and to assist in establishing failure criteria. To further illustrate the impact of including shear deformations, the displacement due to bending and shear for a cantilever beam example are shown in Figure 14, where w represents displacement, P is the applied load, and L is the length of the beam.

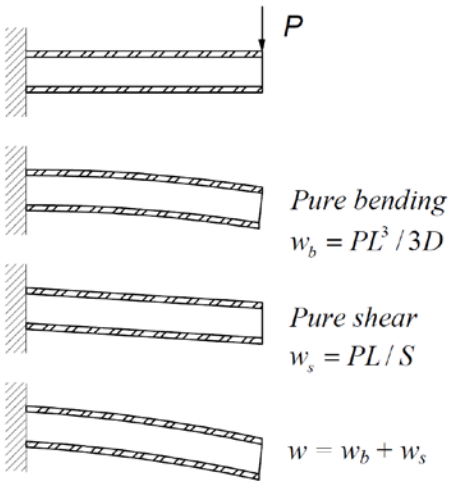

Figure 14. Bending and shear deformation in a cantilever sandwich composite beam. *Image reproduced from Zenkert (1995)*

3.11 Structural Failure Modes

The structural benefits of a 3D-printed core structure are only realized if there are no failures between the face sheets, core, and the adhesive bond holding them together. There are multiple failure modes to check when analyzing sandwich composites. Largely, the failure modes within sandwich composite structures can be described as macro and microbuckling. The primary failure modes considered are described in the following sections.

3.11.1 Face Sheet Failure

The face-sheet failure mode is shown in Figure 15. With a properly designed face-sheet laminate supported uniformly by a conventional core such as in the 13-m wind turbine blade, the risk of this failure mode occurring is low. However, for a 3D-printed honeycomb core, this failure mode requires further investigation. Principal stresses and strains will be extracted from the finite-element model and an appropriate failure criterion such as Tsai-Wu or LARC02 assuming first ply failure will be used to ensure structural integrity and prevent this failure mode.

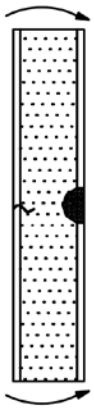

Figure 15. Face-sheet failure mode. ***Image reproduced from Zenkert (1995)***

3.11.2 Core Shear Failure

The core shear failure mode is shown in Figure 16. Core shear failure occurs within the core structure and typically propagates at a 45-degree angle. It will be checked for 3D-printed core structures using the finite-element method to ensure that shear in the core remains below the failure criteria. Structural integrity depends on characterizing the shear strength properties for materials and processes used to 3D print the honeycomb core structures. The equations (Zenkert 1995) driving this failure mode are:

$$\tau_{13} = T_1/d \tag{14}$$

$$\tau_{23} = T_2/d \tag{15}$$

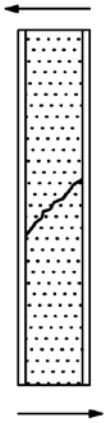

Figure 16. Core shear failure mode. ***Image reproduced from Zenkert (1995)***

3.11.3 General Buckling

The general buckling failure mode of a sandwich composite structure is shown in Figure 17. This failure mode is characteristic of Euler buckling or standard column buckling under compressive loads. General buckling will be checked using the finite-element method to ensure compressive forces remain below the critical buckling load.

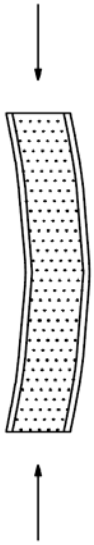

Figure 17. General buckling failure mode. Image reproduced from Zenkert (1995)

3.11.4 Face Sheet Wrinkling

The face-sheet wrinkling failure mode is shown in Figure 18. It is a localized buckling mode of the face sheet due to the transverse stiffness properties of the core material. This failure mode typically occurs in either the compressive face sheet during bending or in either face sheet when subject to in-plane compressive loads. For preliminary design, a practical version of Hoff's method (Hoff and Mautner 1945) is used as the basis to design the 3D-printed honeycomb core. Hoff's method states that the compressive stress in the face sheets must remain below the critical face-wrinkling stress to prevent face wrinkling. Final determination of structural integrity will use the finite-element method. The critical stress to prevent wrinkling is based on the moduli of the face sheets and core materials and is calculated (Zenkert 1995) using:

$$\sigma_{f,critical} = 0.5 * \sqrt[3]{E_f * E_c * G_c} \quad (16)$$

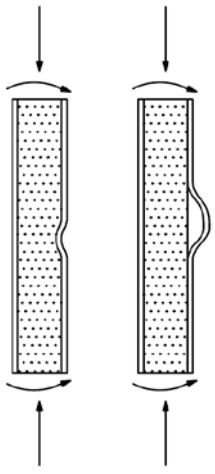

Figure 18. Face-wrinkling failure mode. *Image reproduced from Zenkert (1995)*

3.11.5 Shear Crimping

The shear-crimping failure mode is shown in Figure 19. It is primarily a result of large out-of-plane deformations. Large out-of-plane deformations are prevented by ensuring face-sheet stresses will be kept below the critical stress. Structural integrity will be checked using the finite-element method. For design purposes, the critical face-sheet stress required to prevent shear crimping will be calculated (Zenkert 1995) using:

$$\sigma_{f,critical} = \frac{S}{2 * t_f} \tag{17}$$

Figure 19. Shear crimping failure mode. ***Image reproduced from Zenkert (1995)***

3.11.6 Face-Sheet Dimpling

The face-sheet dimpling failure mode is shown in Figure 20. It is an intracellular buckling mode seen in the face sheets due to the lack of underlying core support. Face dimpling is typically seen in honeycomb cores with open cells. The compressive stress in the face sheets required to cause face dimpling varies with the thickness and modulus of the face material as well as the supporting cell geometry. Structural integrity will be checked using the finite-element method. For the preliminary design of 3D-printed hexagonal honeycomb core structures, the critical stress to cause face dimpling is estimated (Callister 2006; Norris 1964) using:

$$\sigma_{f,critical} = \frac{2 * E_f}{1 - {v_f}^2} \left(\frac{t_f}{s}\right)^2 \tag{18}$$

where (s) is the radius of the honeycomb cell. It is important to note that polymer-based, 3D-printed honeycomb core structures will need open cells to reduce core density and increase specific strength and specific stiffness. It is possible that this failure mode may become the driving failure mode in blade structures using 3D-printed honeycomb core structures.

Figure 20. Face dimpling failure mode. ***Image reproduced from Zenkert (1995)***

3.12 Finite-Element Methods

Finite-element methods are used to ensure the structural integrity of the 13-m wind turbine blade designs with 3D-printed core solutions. Global and local models are developed to perform topology optimization and structural analysis. The global finite-element model uses shell elements that account for transverse shear deformations and composite materials. Individual ply orientation and orthotropic composite material properties are accounted for in the laminate definition within the finite-element code. Global shell model data are mapped to local solid models for more detailed analysis of localized core and face-sheet failure modes. Three-dimensional-printed core design solutions are modeled using solid elements. The unknown material design properties for the 3D-printed core designs are obtained through material property characterization. Characterized material design properties enable advanced computational methods to use topology optimization algorithms within the finite-element analysis software to optimize core designs. The structural optimization process used to optimize core design solutions and ensure structural integrity using computational methods is detailed in Figure 21.

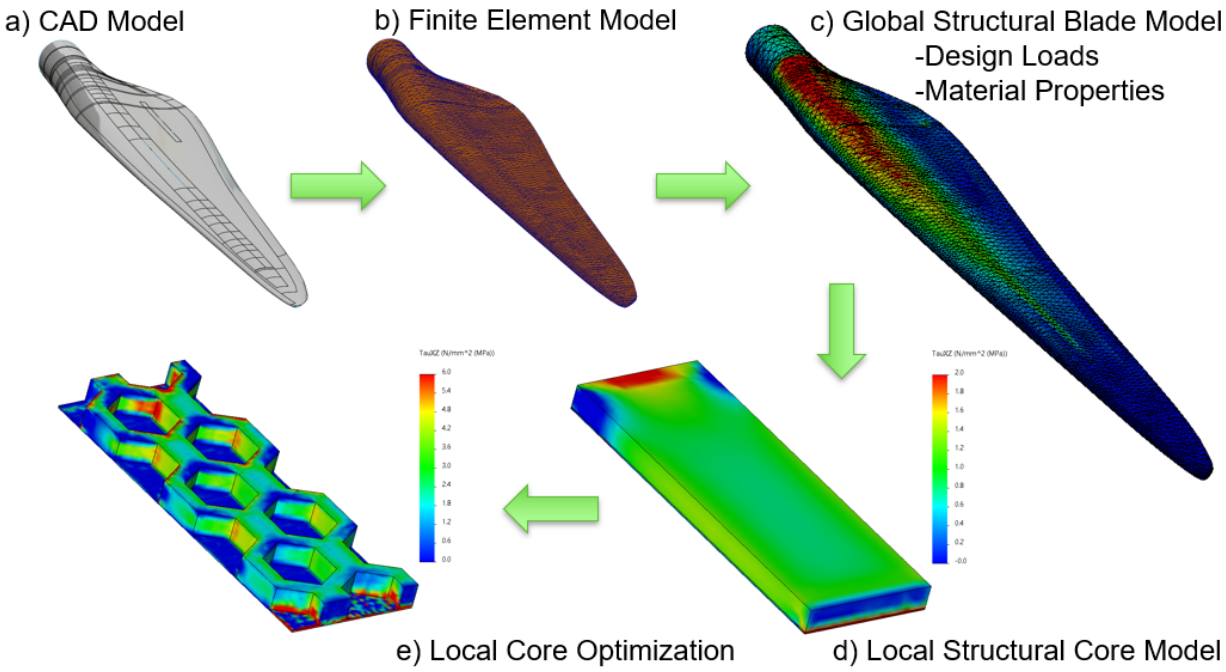

Figure 21. Structural optimization process used to optimize 3D-printed core design solutions.
Illustration created by W.S. Carron, NREL

4 Material Characterization

4.1 Introduction

Material characterization is a necessary step to understanding the fundamental mechanical behavior of 3D-printed structures. However, this behavior can change dramatically depending on process variables. Examples include variations in extruder temperatures, material viscosity, nozzle diameter, deposition layer times, thermal gradients, bead-to-bead fusion, and interlayer cross-linking. This variability is reduced by leveraging the large-scale, 3D-printing knowledge base developed since Oak Ridge National Laboratory 3D-printed the Shelby Cobra demonstrator in 2015 (Love 2015). We chose nozzle diameters, layer times, and tool paths to meet wind industry manufacturing metrics such as cycle time. We also chose thermoplastic and thermoset feedstock formulations to be compatible with wind turbine blade manufacturing processes. Statistical relevance is pursued through the IEC 61400-5 (2020) building block approach as shown in Figure 22. And risk is limited by following the additive manufacturing qualification process specified in DOD Instruction 5000.93 (2021). For coupon testing purposes, fully dense polymer coupons can be described as solid blocks with near-zero porosity. On the other hand, sparse polymer coupons have high porosity and can be described as honeycomb or lattice-like (Hershey et al. 2019). Coupons are tested without face sheets. The mechanical properties of fully dense and sparse coupons are used to calculate relative densities and establish the relationships between relative density and 3D-printed honeycomb core mechanical properties. These mechanical properties are then used by the designer and engineer to perform topology optimization and structural analysis.

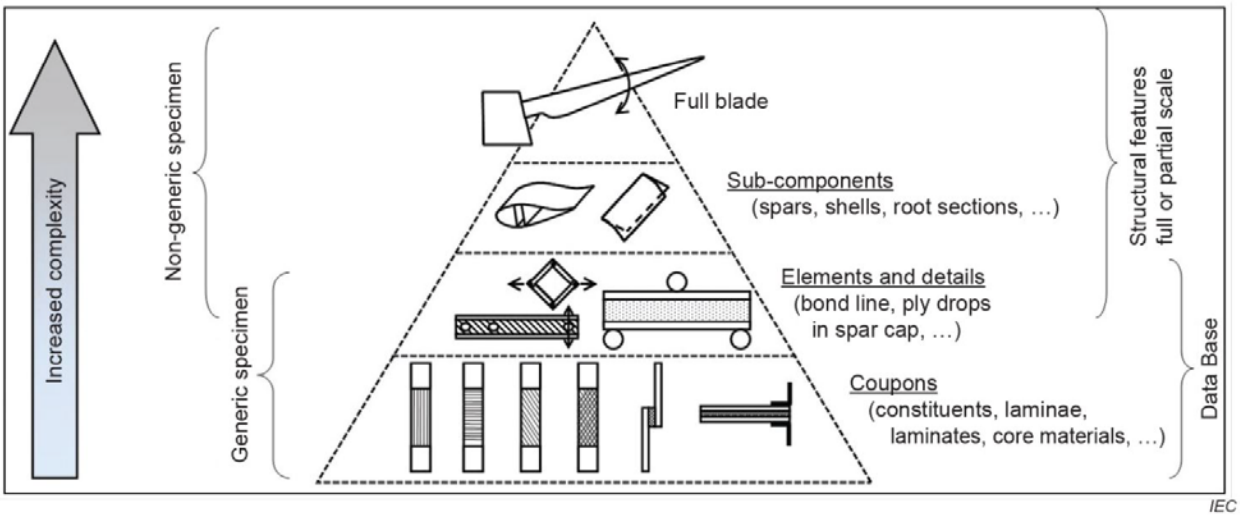

Figure 22. The building block approach for composite structural design. *Figure reproduced from IEC 61400-5 ed.1.0 (2020)*[4,5]

[4] IEC 61400-5 ed.1.0 "Copyright © 2020 IEC Geneva, Switzerland. www.iec.ch

[5] The authors thank the International Electrotechnical Commission (IEC) for permission to reproduce information from its International Standards. All such extracts are copyright of IEC, Geneva, Switzerland. All rights reserved. Further information on the IEC is available from www.iec.ch. IEC has no responsibility for the placement and context in which the extracts and contents are reproduced by the author, nor is IEC in any way responsible for the other content or accuracy therein.

4.2 Testing Standards

A standardized testing process is required to characterize the 3D-printed material shear strength and shear modulus. With a current lack of specific 3D-printed material characterization standards, the program uses existing ASTM standards. There are two primary ASTM standards that can be used to characterize core shear strength, namely ASTM C273 (2020), and ASTM C393 (2016a). ASTM C273 (2020) places the core coupon sample in almost pure shear, whereas ASTM C393 (2016a) places a sandwich composite coupon sample in either three- or four-point bending. The ASTM C273 standard is selected as both shear strength and shear modulus are easily calculated as well as it being the industry standard for characterizing core products. Characterizing core material under ASTM C393 (2016a) is considered more complex, requiring a face sheet with the associated face-sheet-to-core bonding and sizing calculations to ensure core failure. ASTM C393 (2016a) states, "Core shear strength and shear modulus are best determined in accordance with Test Method C273, provided bare core material is available."

4.3 Sample Size

Determining the correct number of coupon specimens to use is a balance between budget and statistical confidence. ASTM C273 (2020) specifies at least five coupon specimens per test condition. However, because little historical data are available regarding 3D-printed polymer shear properties, it is expected that more than five coupon specimens will be required. Assuming a normal distribution of results, we determined that testing 10 coupon specimens will provide the balance between budget and the statistical confidence needed to conduct meaningful design and impactful research.

4.4 Tolerance and Confidence Levels

Test data from coupon specimens require further processing to develop a characteristic material property that can then be used to develop design properties. The wind turbine blade industry follows a standardized material characterization process (Det Norske Veritas 2010; Sutherland and Veers 1999; Tadich Wedel-Heinen, and Petersen 2005; IEC 2019). Specifically, characteristic values for wind turbine blade structures are based on the lower limit of the populations 5th percentile, with 95% confidence. Or in other words, 95% of the population equals or exceeds the characteristic value with 95% confidence (i.e., 95/95). In comparison, the aerospace industry commonly uses a stricter A-basis for primary structures, which is a 95%-lower confidence bound on the first percentile of a specified population (i.e., 95/99) and a less-strict B-basis for secondary structures, which is a 95%-lower confidence bound on the 10th percentile of a specified population of measurements (i.e., 95/90) (DOD 2002).

4.5 Characteristic Material Properties

The general method used to postprocess the coupon specimen test data to derive a characteristic material property value is provided here.

First, compute the sample mean (IEC 2019):

$$\bar{x} = \frac{1}{n} \sum_{i=1}^{n} x_i \tag{19}$$

Next, compute the sample variance (IEC 2019):

$$s^2 = \frac{1}{n-1} \sum_{i=1}^{n} (x_i - \bar{x})^2 \quad (20)$$

Finally, calculate the characteristic value. This requires a k-multiplier. As both the population variance is unknown for the 3D-printed material and additive manufacturing process, and there is no prior knowledge, we assumed a normally distributed population with a k-multiplier for one-sided tolerance. For wind turbine blade structures where 95% of the population equals or exceeds the characteristic value with 95% confidence, the k-multipliers for up to 10 samples is provided in Table 4 (Krishnamoorthy and Mathew 2009; Joglekar 2003; Det Norske Veritas 2010; Herbert and Veers 1999). The characteristic value is then calculated using Eq. 21 (IEC 2019):

$$X_k = \bar{x} - (k * s) \quad (21)$$

Table 4. Wind Turbine Blade Structures 95/95 K-Multipliers for One-Sided Normal Tolerance Limits. Values obtained from Krishnamoorthy and Mathew (2009); Joglekar (2003); Det Norske Veritas (2010); Herbert and Veers (1999).

n	k-multiplier
2	26.26
3	7.656
4	5.144
5	4.203
6	3.708
7	3.399
8	3.187
9	3.031
10	2.911

4.6 Design Material Properties

The characteristic material property is reduced by a material safety factor to obtain a design property. This design property can then be used for structural analysis purposes. For wind turbine blade structures, the material safety factor (γ_m) is calculated using a set of partial material safety factors as described in the IEC 61400-5 (2020) standard. The material safety factor is calculated using the following equation (IEC 2020):

$$\gamma_m = \gamma_{m0} \times \gamma_{m1} \times \gamma_{m2} \times \gamma_{m3} \times \gamma_{m4} \times \gamma_{m5} \quad (22)$$

A description of each partial material safety factor is described in IEC 61400-5 (2020) as well as in Table 4.2. Partial material safety factors are specific to the type of structure and structural analysis. Further, they are derived for sandwich composites in both strength and stability analyses.

Table 5. Descriptions of Partial Material Safety Factors (IEC 2020)

Material Safety Factors	Description
γ m0	Base Material Factor (To Be Included in All Analyses)
γ m1	Factor for environmental degradation (nonreversible effects)
γ m2	Factor for temperature effects (reversible effects)
γ m3	Factor for manufacturing effects
γ m4	Factor for calculation accuracy and validation of method
γ m5	Factor for load characterization

The design material property to be used by designers and engineers for design and structural analysis purposes is calculated using the following equation (IEC 2019), as found in IEC 61400-5 (IEC 2020):

$$X = \frac{X_k}{\gamma_m} \tag{23}$$

4.6.1 Material Safety Factor for Strength Analysis

Table 6 provides the partial material safety factors we chose from IEC 61400-5 (IEC 2020) for strength analysis of sandwich composite blade structures. The total material safety factor (γ_m) for strength analyses is calculated to be 2.7. Therefore, to achieve a required level of safety and reliability for a sandwich composite structure in a wind turbine blade under ultimate limit state loads, the characteristic material property for a 3D-printed core must be reduced by a factor of 2.7.

Table 6. Material Safety Factor for Strength Analysis of Sandwich Composite Blade Structures. Values Chosen from IEC 61400-5 (2020).

Material Safety Factors	Description	Value
γ_{m0}	Base material factor	1.2
γ_{m1}	Factor for environmental degradation (nonreversible effects)	1.1 (closed cell foams with resin infusion)
γ_{m2}	Factor for temperature effects (reversible effects)	1.1 (material testing performed at room temperature)
γ_{m3}	Factor for manufacturing effects	1.3 (the blade analysis is performed using nominal design properties)
γ_{m4}	Factor for calculation accuracy and validation of method	1.2 (for computation using a finite-element analysis using 3D elements for the core and that models geometric nonlinearities but that has not been validated by intermediate-level or full blade testing)
γ_{m5}	Factor for load characterization	1.2 (loads in four main directions)
γ_m	Final partial material safety factor	2.7

4.6.2 Material Safety Factor for Stability Analysis

Table 7 provides the partial material safety factors we chose from IEC 61400-5 (2020) for stability (i.e., buckling) analysis of sandwich composites blade structures. The total material safety factor (γ_m) for stability analyses is calculated to be 1.9. Therefore, to achieve a required level of safety and reliability for a sandwich composite structure in a wind turbine blade under buckling loads, the characteristic material property for a 3D-printed core must be reduced by a factor of 1.9.

Table 7. Material Safety Factor for Stability Analysis of Sandwich Composite Blade Structures. Values Chosen from IEC 61400-5 (2020).

Material Safety Factors	Description	Value
γ_{m0}	Base material factor	1.2
γ_{m1}	Factor for environmental degradation (nonreversible effects)	1.0 (no effect accounted for)
γ_{m2}	Factor for temperature effects (reversible effects)	1.1 (when using core material modulus values at room temperature)
γ_{m3}	Factor for manufacturing effects	1.0 (no effect accounted for)
γ_{m4}	Factor for calculation accuracy and validation of method	1.2 (for computation using finite-element analysis using 3D elements for the core and that models geometric nonlinearities but that has not been validated by intermediate-level or full blade testing)
γ_{m5}	Factor for load characterization	1.2 (loads in four main directions)
γ_{m}	Final partial material safety factor	1.9

5 Coupon Specimen Characterization

5.1 3D-Printed Core Material Properties

As described in IEC 61400-5 (2020), the building block approach is used for designing composite structures. The approach starts with characterizing material properties at the coupon specimen level. As discussed previously, it is extremely important to understand the in-plane shear strength and transverse shear modulus to successfully design 3D-printed sandwich composite core structures. This material uncertainty is largely due to the layer-by-layer deposition process and the amount of adhesion between beads. Continuous fibers within a traditional fiber-reinforced composite blade structure are infused with a matrix material that facilitates uniform load transfer between fibers. The lignan in balsa wood acts the same way. A 3D-printed structure does not have a matrix material connecting the beads, such as epoxy or lignan, and load transfer between beads relies on the bead-to-bead bond. For thermoplastic polymers, this bond can be improved through increased bead contact area and elevated temperatures within the 3D print chamber. For thermoset polymers, this bond can be improved through increased bead contact area and the cure times and temperatures that promote cross-linking. Several thermoplastic and thermoset coupon specimens are validated using the ASTM C273 (2020) test fixture in tension to characterize their in-plane shear strength (τ_{12}) and transverse shear modulus (G_{23}) properties; however, only in-plane shear (τ_{12}) data are presented.

5.2 3D-Printed Thermoplastic Material

The pelletized thermoplastic feedstock used to 3D print the thermoplastic panels is Techmer PM's Electrafil J-1200/CF/20 (ABSCCF20) (Duty, Drye, and Franc 2015). The feedstock contains chopped carbon fiber, 20% by weight, or approximately 13% by volume, and is added for dimensional stability and increased mechanical properties. Panels are printed on the Cincinnati Big Area Additive Manufacturing (BAAM) large-scale 3D printer with a 7.62-mm diameter extruder nozzle. Coupon specimens are machined from the 3D-printed panels. The 3D-printed thermoplastic material tensile strength is reported as 65.7 megapascals (MPa) in the 1-axis and 10.27 MPa in the 3-axis (i.e., z-direction) (Duty, Drye, and Franc 2015). 3D-printed shear strength is not reported (Duty, Drye, and Franc 2015). For reference, the tensile strength of non-3D printed, neat ABS, without chopped carbon fiber, is reported as approximately 34 MPa (Hassen et al. 2016).

5.3 3D-Printed Thermoset Material

The thermoset feedstocks used to 3D print the thermoset panels are Polynt S.p.A. PRD-EX1631 and PRD-EX1631-LS (Polynt 2021). They are both a vinyl-ester-based reactive resin system designed for low-density, 3D-printed tooling and direct-to-part applications using a large-scale 3D printer. Both thermosets contain chopped carbon-fiber additives for dimensional stability and increased mechanical properties. The 3D-printed panels are provided by Polynt S.p.A. Details on the large-scale 3D printing equipment, chemical additives, nozzle diameters, content of chopped carbon fiber by weight, and cure temperatures and times, is not provided. Both PRD-EX1631 and PRD-EX1631-LS resins are reported to have similar cured density and strength characteristics, with the PRD-EX1631-LS being a lower-shear-viscosity alternative. Coupon specimens are machined from the 3D-printed panels. The 3D-printed thermoset material tensile strength is reported as 24.13 MPa in the 1-axis (Polynt 2021). The 3D printed tensile strength in

the 3-axis (i.e., z-direction) is not reported, although data presented by Kunc et al. (2019) indicates it will be significantly less than the 1-axis. The 3D-printed shear strength is not reported.

5.4 Coupon Specimen Bead Orientation

The coupon specimens are machined from larger 3D-printed panels. To characterize the in-plane shear strength (τ_{12}), and transverse shear modulus (G_{23}), the coupons are machined from 3D-printed panels such that the bead orientation is aligned with the load direction as shown in Figure 23.

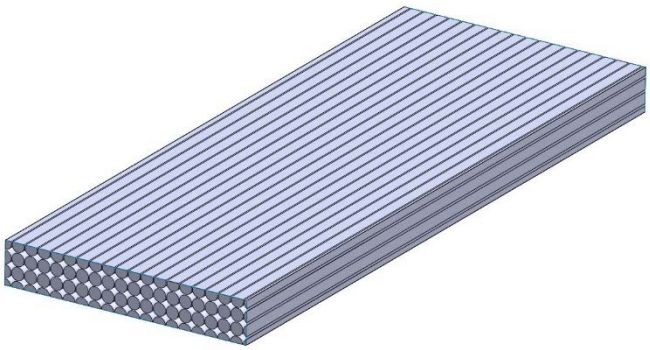

Figure 23. Representative coupon specimen bead alignment for characterizing τ_{12} and G_{23}.
Illustration created by W.S. Carron, NREL

5.5 Coupon Specimen Dimensions

The ASTM C273 (2020) standard requires that the coupon specimen have a thickness equal to the thickness of the sandwich core used in the design, a width not less than 50 mm, and a length not less than 12 times the thickness. The coupon thickness is based on the maximum balsa core thickness of 12.7 mm in the 13-m NRT blade (Kelley 2020). The coupon specimen dimensions are designed to be 152.4 mm long, 50.8 mm wide, and 12.7 mm thick, as shown in Figure 24. Faces are machined flat and parallel for bondline control and to minimize eccentricities or stress concentrations that could initiate peel or adhesive failure under load.

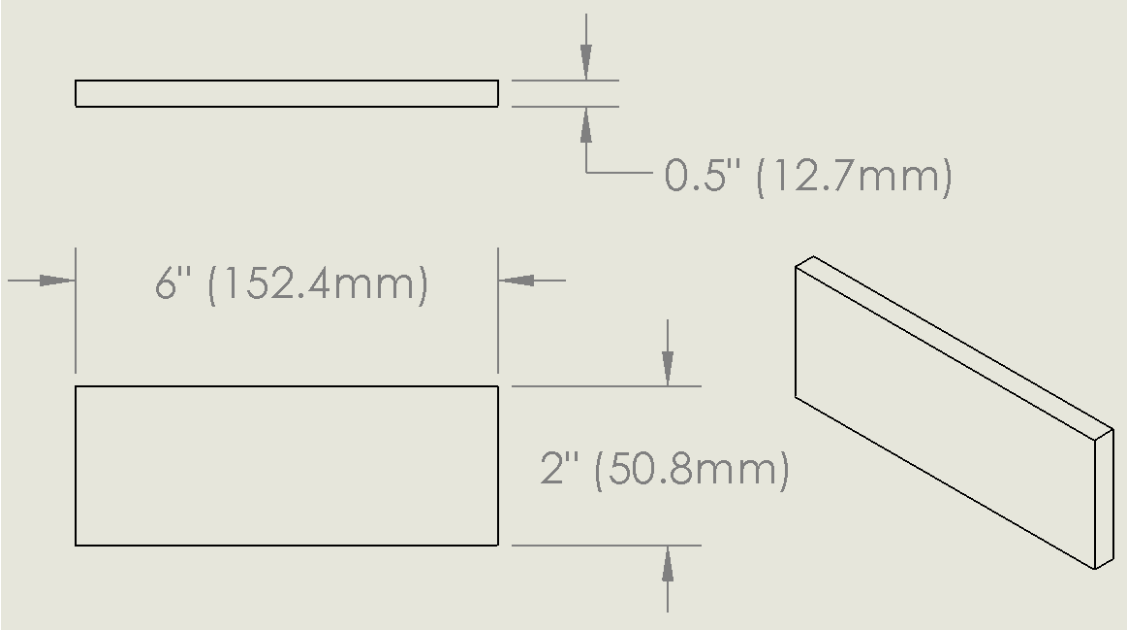

Figure 24. Coupon specimen dimensions. ***Illustration created by W.S. Carron, NREL***

5.6 Coupon Specimen Bonding

The ASTM C273 (2020) standard states that an adhesive failure invalidates the test data. Thus, it becomes essential when testing core materials to prevent adhesive failure. Many causes of an adhesive joint failure such as peel failure, improper surface preparation, and improper adhesive cure can be prevented through proper design and bonding processes. However, there are several failure modes, such as lap shear failure, which depend on sourcing the correct structural adhesive for the adherends being bonded together. Polymers complicate the sourcing of structural adhesives as polymer substrates commonly fail well before the full lap shear strength of a structural adhesive is realized. As a result, it is not always clear from a structural adhesive TDS whether the adhesive lap shear strength is an adhesive failure or polymer substrate failure. Some vendors will denote substrate failure in their TDS, but many will not. This adhesive lap shear strength uncertainty is further complicated when the polymer adherend is a 3D-printed polymer that may contain additional chemical additives, chopped carbon fibers, and expandable microspheres in the feedstock.

The correct method to reduce this uncertainty is to qualify the adhesive for each type of 3D-printed polymer using ASTM standards. Standards such as ASTM D907 (2016b), ASTM D1002 (2019), ASTM D3163 (2014), and ASTM D3164 (2017) can be followed to qualify structural adhesives. Performing these additional tests are extremely costly and time-consuming. Instead, a wide range of commercially available structural adhesives are evaluated to avoid the additional adhesive qualification. Vendor TDS research alongside vendor discussions targeted several structural adhesive chemistries potentially compatible with 3D-printer polymer feedstock such as ABS and vinyl ester. The promising adhesive chemistries identified are methyl methacrylates, ethyl cyanoacrylates, and epoxies.

Cyanoacrylates, such as Henkel's Loctite 401[6] and Loctite 414[7] are found to have high overlap lap shear strength for an ABS polymer substrate but also have short working times and rapid cure times. Epoxies, such as 3M's W1125[8] , Henkel's Loctite E-20HP[9], and Huntsman's Araldite 2013-1[10] are found to have good overlap lap shear strength for an ABS polymer substrate but have long working and fixture times, with full-cure strength occurring within days. Methacrylates, such as ITW Performance Polymers Plexus MA310,[11] Plexus MA8110[12] and Plexus MA8120,[13] are found to have high lap-shear strength for bonding many polymers but also have the added benefit of 10-minute working times and 30-minute fixture times at room temperature. Plexus' MA8110 and MA8120 have the additional benefit of not requiring complicated surface preparation or priming products to bond to the steel load plates. Plexus' MA8110 and Huntsman Araldite 2013-1 were selected as the two structural adhesives for bonding the 3D-printed coupon specimens to the steel load plates.

Adhesive thickness needs be controlled to achieve maximum overlap shear strength. Too little or too much adhesive will weaken the adhesive joint. A vendor TDS will commonly provide bondline or gap thickness recommendations. The ITW Performance Polymers Plexus MA8110 TDS recommends a bondline thickness of 0.762 mm, whereas the Huntsman Araldite 2013-1 TDS recommends a bondline thickness between 0.05 mm and 0.10 mm. Glass microbeads are added to the structural adhesive to maintain the bondline thickness.

5.7 Test Fixture Assembly

The ASTM C273 test requires that the coupon specimen be rigidly supported via steel plates. The coupon specimens are bonded to 10.16-mm-thick, 17-4PH, stainless-steel loading plates from Wyoming Test Fixtures.[14] The coupon specimen is oriented with the bead direction aligned with the loading direction. A schematic of the coupon specimen, adhesive, and steel load plates within the overall test fixture assembly is shown in Figure 25.

[6] https://www.henkel-adhesives.com/us/en/product/instant-adhesives/loctite_401.html
[7] https://www.henkel-adhesives.com/us/en/product/instant-adhesives/loctite_414.html
[8] https://multimedia.3m.com/mws/media/689214O/3m-wind-epoxy-structural-adhesivew1125.pdf
[9] https://www.henkel-adhesives.com/us/en/product/structural-adhesives/loctite_ea_e-20hp.html
[10] https://www.huntsman.com/products/detail/333/araldite
[11] https://itwperformancepolymers.com/products/plexus/general-purpose/plexus-ma310/
[12] https://itwperformancepolymers.com/products/plexus/primerless-to-metal/plexus-ma8110/
[13] https://itwperformancepolymers.com/products/plexus/primerless-to-metal/plexus-ma8120/
[14] https://wyomingtestfixtures.com/products/shear/sandwich-panel-flatwise-shear-test-fixture-astm-c-273/

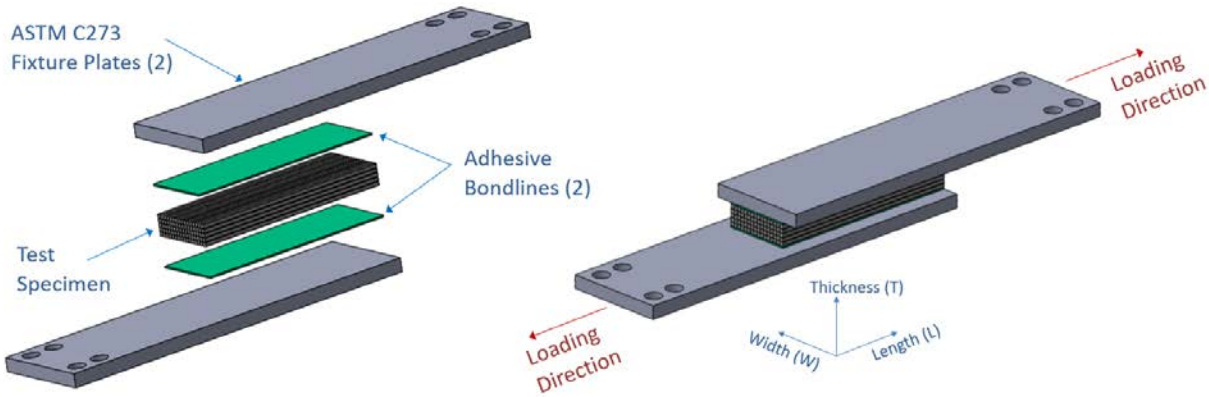

Figure 25. Exploded view (left), and assembled view (right), of the test fixture assembly. ***Illustration created by Scott Hughes, NREL***

Coupon specimens are machined using a TensileMill CNC MINI. The computer numerical control (CNC) mill is used to ensure flatness and parallelism of the bonding surfaces of the coupon specimen, as shown in Figure 26.

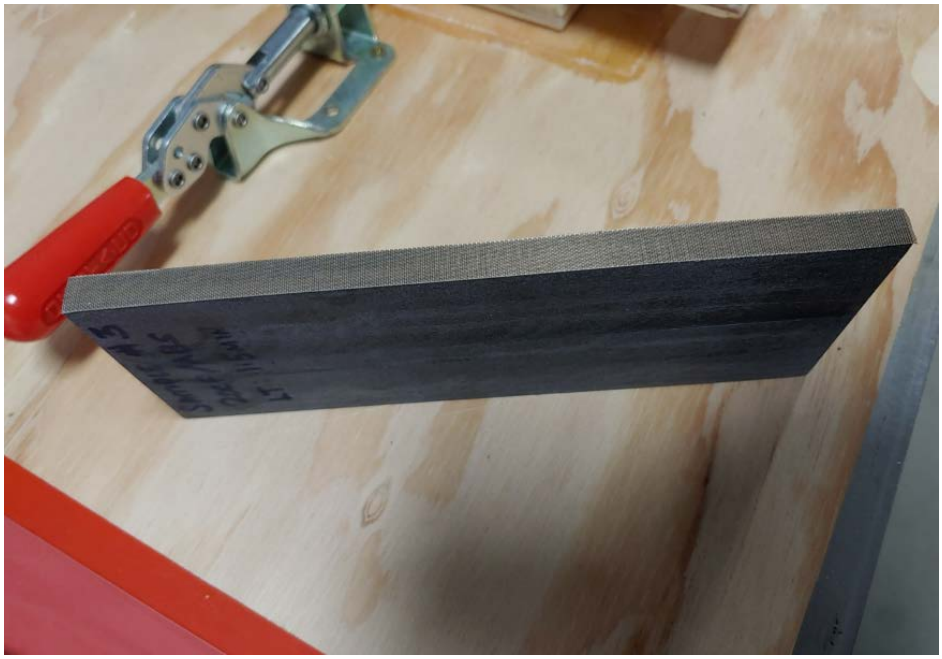

Figure 26. Coupon specimen prior to bonding into the test fixture assembly. ***Photo by NREL***

The final dimensions of the coupon specimen are measured after CNC machining and are provided in Table 8. Each coupon specimen is identified and labeled with a unique identifier. The three thermoplastic coupon specimens are identified by a "ABSCCF20" prefix. The two low-shear viscosity thermoset coupon specimens are identified by a "1631-LS" prefix. And the five thermoset coupon specimens are identified by a "1631-LS" prefix.

Table 8. Coupon Specimen Dimensions

Coupon Specimen ID	Coupon Specimen Length [mm]	Coupon Specimen Width [mm]	Calculated Shear Area [mm^2]	Coupon Specimen Thickness [mm]
ABSCCF20-D	199	71.88	14304	12.90
ABSCCF20-1	198	73.47	14547	10.10
ABSCCF20-3	199	73.55	14637	10.00
1631-LS-2-01	154	50.87	7833	9.16
1631-LS-2-02	154	51.12	7873	13.74
1631-3-01	154	50.54	7783	13.47
1631-3-02	154	50.75	7815	13.53
1631-3-03	152	50.59	7690	12.64
1631-3-04	152	50.71	7708	13.46
1631-3-05	152	50.67	7701	12.40

The process for adhesively bonding the coupon specimens to the steel loading plates evolved during testing. Process improvements focused on surface preparation, bondline control, test fixture assembly alignment, and bonding fixtures. The steel-load-plate surface preparation process involved abrading the steel surface with either sandpaper or grit blasting, and then cleaning with isopropyl alcohol (IPA). Coupon specimen surface preparation involved lightly abrading the polymer surface with sandpaper, cleaning with IPA, and conditioning the specimens. Bondline control is maintained by adding 2%, by weight, glass microbeads to the structural adhesive to maintain a constant adhesive thickness. The structural adhesive is placed under a vacuum to remove air bubbles after mixing in the glass microbeads. An alignment fixture is used to prevent eccentricities and ensure parallel edges of the steel loading plates and coupon specimen. A constant clamping force is provided through the alignment fixture to ensure uniform adhesive squeeze out of the adhesive and a constant bondline thickness. Teflon tape is applied outside the bonded joint to prevent adhesive squeeze out from adhering to unwanted surfaces, and negatively influencing test results.

Figure 27 shows the application of the structural adhesive to the steel-loading plate as well as the alignment fixture applying a clamping force to the test fixture assembly. A completed test fixture assembly is shown in Figure 28, with the steel-loading plates bonded to the coupon specimen.

Table 9 provides the test fixture assembly details, including surface preparation methods, structural adhesive, and bondline control.

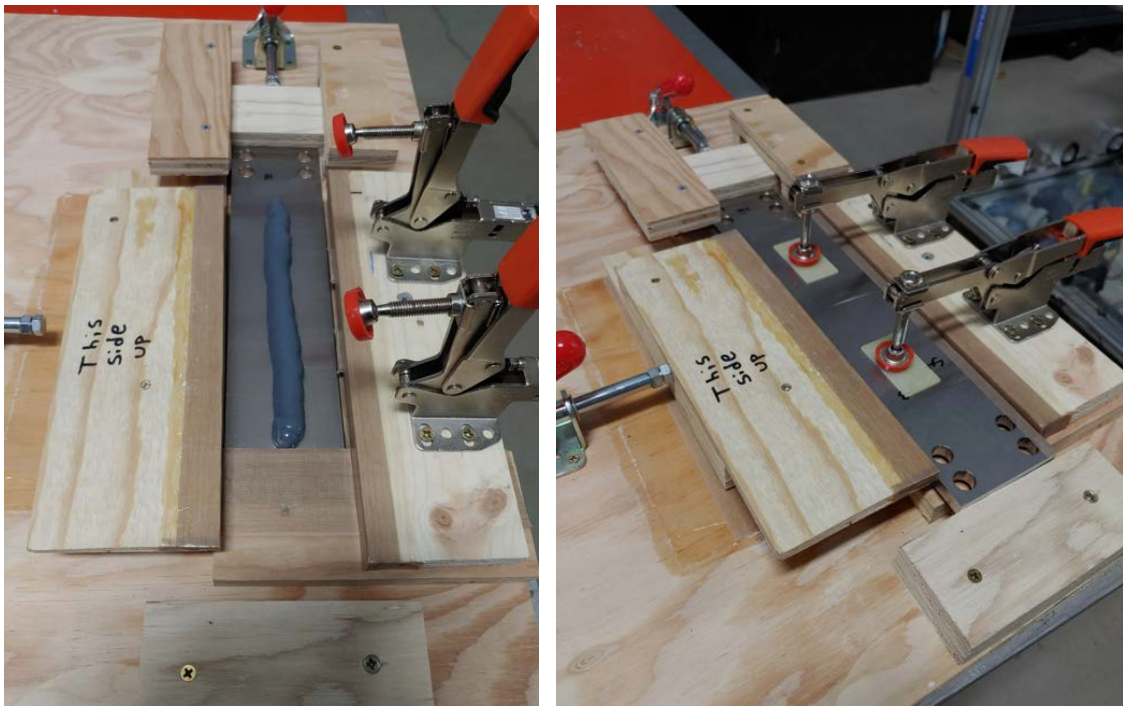

Figure 27. Application of structural adhesive to a steel-loading plate (left) and clamping of a test fixture assembly (right). ***Photo by NREL***

Figure 28. Completed test fixture assembly. ***Photo by NREL***

Table 9. Test Fixture Assembly Details

Coupon Specimen ID	Structural Adhesive	Glass Microbead Diameter and Details	Coupon Specimen Bonded Surface Prep	Steel-Loading Plate Surface Prep
ABSCCF20-D	Plexus 8110	0.686 mm, sprinkled	IPA wipe	IPA wipe
ABSCCF20-1	Plexus 8110	none	CNC mill, IPA wipe	IPA wipe
ABSCCF20-3	Plexus 8110	0.594 mm, 2% by weight	CNC mill, IPA wipe	IPA wipe
1631-LS-2-01	Araldite 2013-1	0.104 mm, 2% by weight	CNC mill, IPA wipe	IPA wipe
1631-LS-2-02	Araldite 2013-1	0.104 mm, 2% by weight	CNC mill, 80-grit sandpaper, IPA wipe	80-grit sandpaper, IPA wipe
1631-3-01	Araldite 2013-1	0.104 mm, 2% by weight	CNC mill, 80-grit sandpaper, IPA wipe	80-grit sandpaper, IPA wipe
1631-3-02	Araldite 2013-1	0.104 mm, 2% by weight	CNC mill, 80-grit sandpaper, IPA wipe	80-grit sandpaper, IPA wipe
1631-3-03	Araldite 2013-1	0.104 mm, 2% by weight	CNC mill, IPA wipe	IPA wipe
1631-3-04	Plexus 8110	0.594 mm, 2% by weight	CNC mill, IPA wipe	IPA wipe
1631-3-05	Araldite 2013-1	0.104 mm, 2% by weight	CNC mill, IPA wipe	Blast 45-grit aluminum oxide, IPA wipe

5.8 Test Setup

Material characterization is performed on the 250-kilonewton (kN) load frame at NREL's Composites Manufacturing and Education Technology facility. Figure 29 provides a schematic of the test setup. At the top of the load path, an alignment fixture and load cell are attached to the crosshead of the load frame. The load frame actuator is at the base of the load path. Universal joints and Type Dm clevises are located between the load cell and test fixture assembly, and between the actuator and test fixture assembly. An extensometer fixture is magnetically connected to the steel-loading plates.

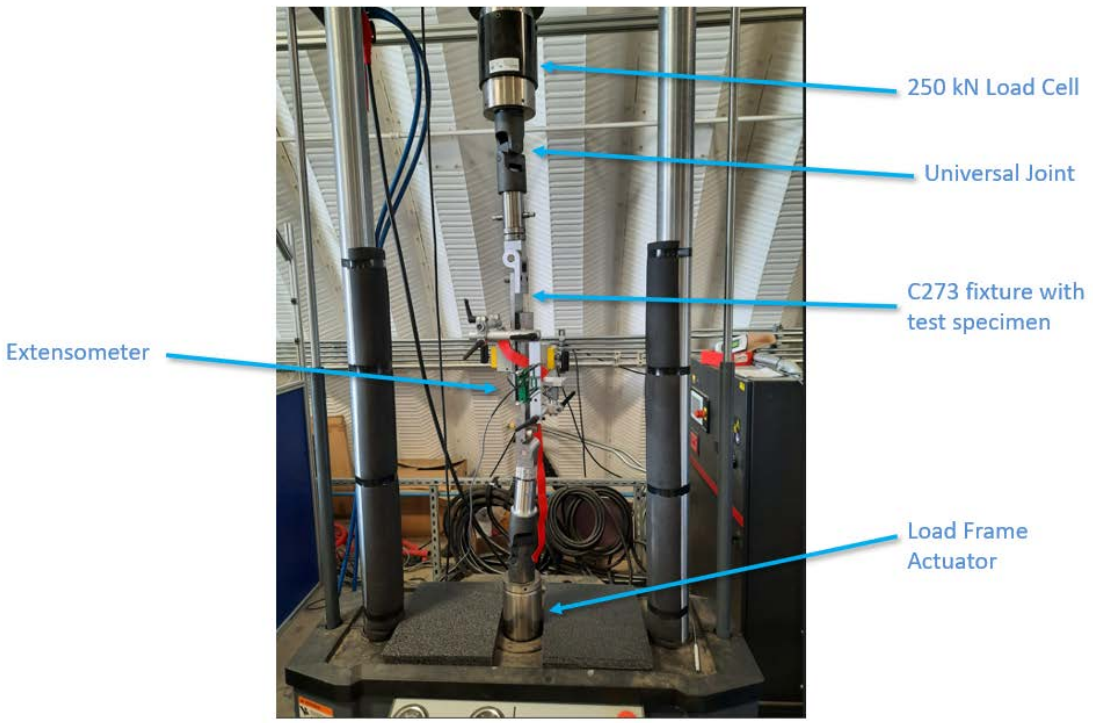

Figure 29. Test setup assembly in the 250-kN load frame. *Photo by NREL*

5.9 Test Procedure and Results

A head displacement rate of 0.50 mm/minute is used for all tests, as suggested in the ASTM C273 standard (2020). Load, actuator displacement, and extensometer data is recorded with an MTS controller. The load cell reading is electronically zeroed with a steel-loading plate and half of the extensometer fixture hanging from the load cell. A data sampling rate of 100 hertz is used for all tests, with all tests run to failure. Table 10 provides the maximum recorded force in the coupon specimen at failure for each test run and a description of the failure mode.

Table 10. Maximum Recorded Force in the Coupon Specimen at Failure

Coupon Specimen ID	Maximum Recorded Force [kN]
ABSCCF20-D	63.4
ABSCCF20-1	70.8
ABSCCF20-3	67.2
1631-LS-2-01	13.9
1631-LS-2-02	13.4
1631-3-01	22.0
1631-3-02	13.5
1631-3-03	7.5
1631-3-04	34.4
1631-3-05	35.0

Ultimate shear strength at failure is provided in Table 11. ASTM C273 (2020) states that adhesive or cohesive failures, or both, at the core-to-load plate interface are not acceptable failure modes and noted as invalid. Valid test specimen failure modes according to ASTM C273 (2020) are observed only for coupon specimens 1631-LS-2-01 and 1631-LS-2-01. Complex interface failure modes are observed on the other coupon specimens, as noted in Table 11. Ultimate shear strength in the coupon specimen at failure is calculated by dividing the maximum recorded force given in Table 10 by the calculated shear area from Table 8.

Table 11. Ultimate Shear Strength at Failure and Failure Mode Description

Coupon Specimen ID	Ultimate Shear Strength [MPa]	Failure Mode Description
ABSCCF20-D	4.43	Invalid; interface failure, adhesive to core, entire length
ABSCCF20-1	4.87	Invalid; interface failure, adhesive to core, entire length
ABSCCF20-3	4.59	Invalid; interface failure, adhesive to core, entire length
1631-LS-2-01	1.78	Valid; core shear failure, within core, entire length
1631-LS-2-02	1.70	Valid; core shear, within core, entire length
1631-3-01	2.83	Invalid; interface failure, adhesive-to-steel load plate, majority of entire length
1631-3-02	1.73	Invalid; interface failure, adhesive-to-steel load plate, entire length
1631-3-03	0.978	Invalid; interface failure, adhesive-to-steel load plate, entire length
1631-3-04	4.47	Invalid; interface failure, adhesive to core, various locations
1631-3-05	4.55	Invalid; interface failure, adhesive to core, various locations

Figure 30 shows the invalid core shear failure mode for coupon specimen ABSCCF20-3. This coupon specimen produced an interface failure in the area between the adhesive and core surface and is located throughout the entire length of the interface. The other two ABSCCF20 coupon specimens tested failed similarly. There are significant interbead gaps along the shear failure plane, as shown in Figure 31. These interbead and interlayer gaps exist in all of the 3D-printed thermoplastic specimens and are an artifact of large-scale, polymer-based, additive manufacturing using material extrusion. More research is needed to assess the impact of these gaps and in particular gaps on the order of 1,000 microns on the structural integrity of the 3D-printed parts and if they initiate crack propagation leading to failure.

Figure 30. 3D-printed thermoplastic coupon specimen ABSCCF20-3 after loading to failure. ***Photo by NREL***

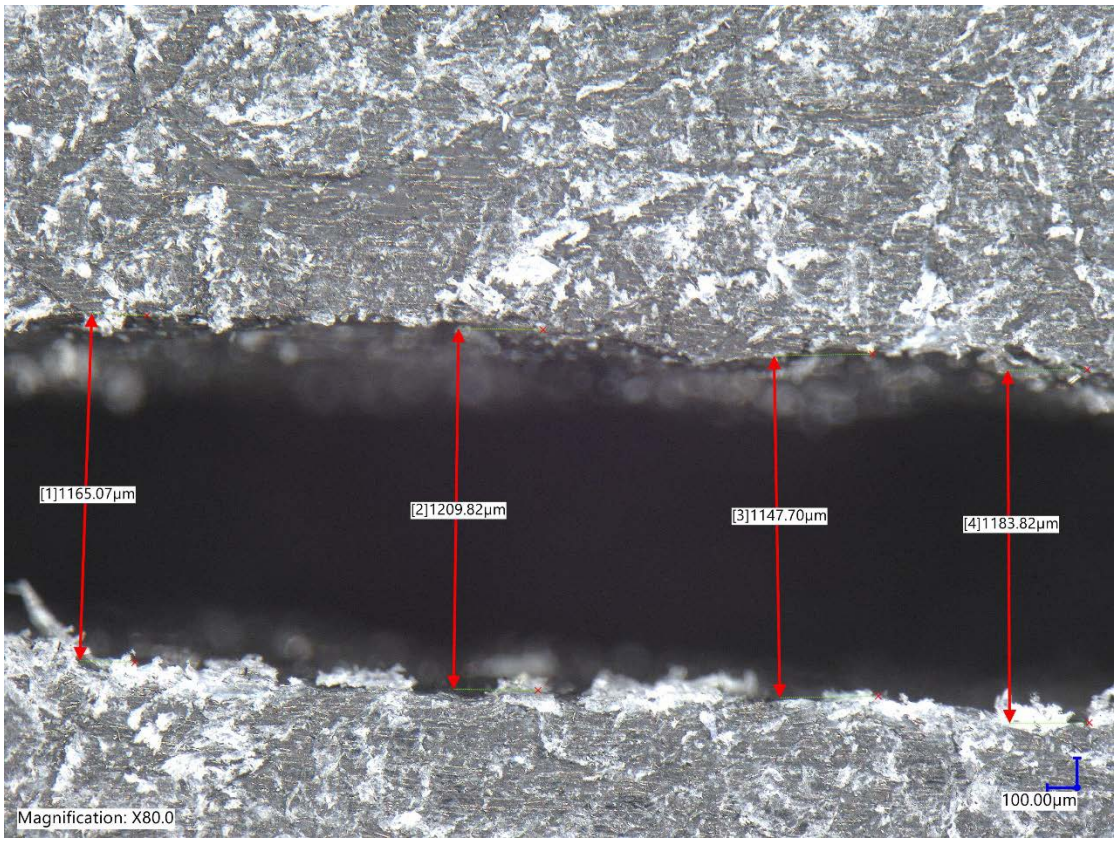

Figure 31. Interbead gaps within the 3D-printed thermoplastic coupon specimen ABSCCF20-3.
Photo by NREL

Figure 32 shows the valid core shear failure modes for coupon specimens 1631-LS-2-01 and 1631-LS-2-02. These coupon specimens produced a core shear failure in an area within the core and located through the entire length of the specimen.

Figure 32. 3D-printed thermoset coupon specimens 1631-LS-2-01 (left) and 1631-LS-2-02 (right) after loading to failure. *Photo by NREL*

Figure 33 shows the invalid core shear failure modes for coupon specimens 1631-3-04 and 1631-3-05. These specimens produced an interface failure in the area between the adhesive and the core surface that is located at various regions along the length of the interface. Coupon specimens 1631-3-01, 1631-3-02, and 1631-3-03 produced interface failures between the Araldite 2013-1 adhesive and the steel-load plates, leaving a shiny steel surface with little-to-no adhesive attached. These failure modes initiated the change to the Plexus 8110 adhesive in coupon specimen 1631-3-04, and the change to Araldite 2013-1 with sand-blasted steel-load plates in coupon specimen 1631-3-05. As shown in Figure 33, the Plexus 8110 adhesive appears to have provided a better bond to both the steel-load plates and the thermoset polymer.

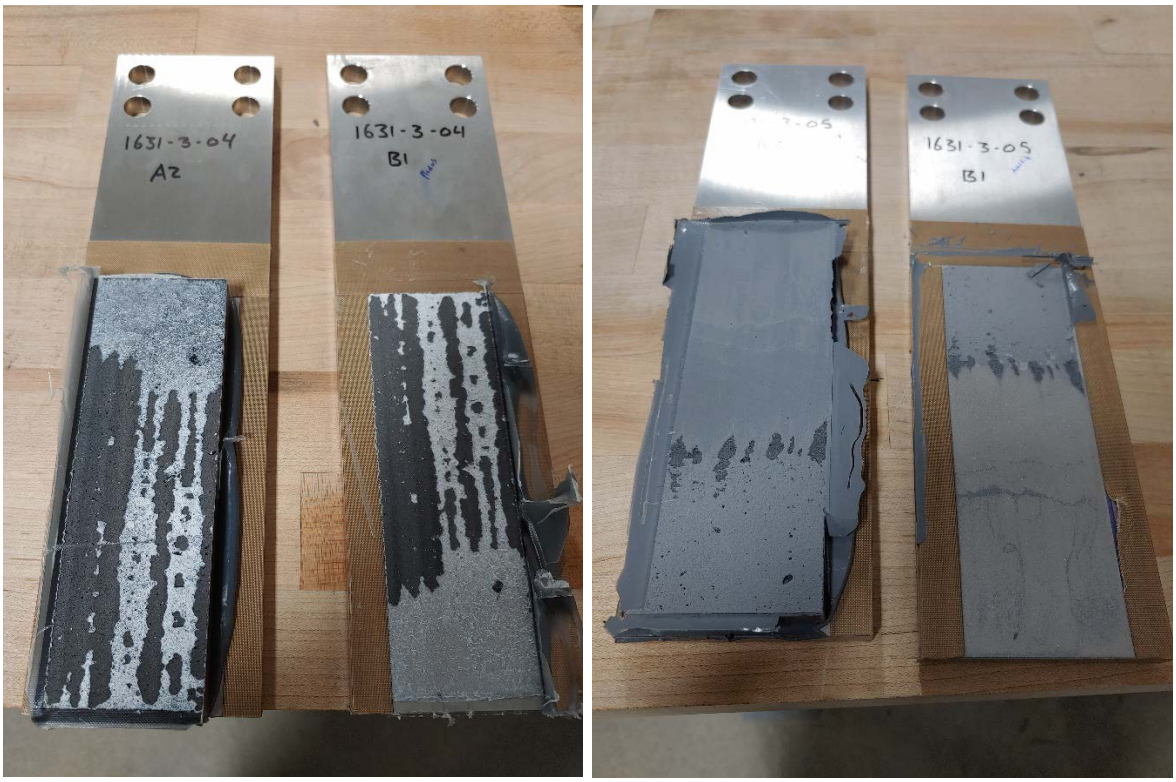

Figure 33. 3D-printed thermoset coupon specimens 1631-3-04 (left) and 1631-3-05 (right) after loading to failure. *Photo by NREL*

5.10 Characteristic Shear Strength

The 3D-printed core shear strength test data for each of the individual coupon specimens are characterized using statistical methods, as described in Section 4.5. Both the mean and characteristic core shear strength values for each of the 3D-printed core materials are provided in Table 12. The ultimate mean shear strength is used to compare against vendor TDS data sheets that report mean values. The characteristic shear strength along with partial material safety factors are applied to calculate the design shear strength used in the structural analysis of the wind turbine blade.

The characteristic 3D-printed ultimate core shear strength (τ_{12}) for the 3D-printed ABSCFF20 material is based on all the coupon specimens tested. The characteristic 3D-printed ultimate core shear strength (τ_{12}) for the 3D-printed PRD-EX1631 material is based on data from only coupon specimens 1631-3-04 and 1631-3-05, as coupon specimens 1631-3-01, 1631-3-02, and 1631-3-03 experienced load-plate-to-adhesive failure. The characteristic 3D-printed ultimate core shear strength (τ_{12}) for the 3D-printed PRD-EX1631-LS material is based on all coupon specimens tested.

Table 12. Characteristic Shear Strength of 3D-Printed Coupon Specimens

3D-Printed Core Material	Sample Size	Mean Shear Strength (MPa)	Standard Deviation	k-multiplier	Characteristic Shear Strength (MPa)
ABSCFF20	3	4.62	0.208	7.656	2.91
PRD-EX1631	2	4.51	0.110	26.26	1.63
PRD-EX1631-LS	2	1.74	0.051	26.26	0.39

5.11 Specific Shear Strength

The specific shear strength for each of the 3D-printed core materials is calculated using mean values from Table 12 and nominal material densities (Kim et al. 2018; Polynt 2021), as shown in Table 13. Specific shear strength is a widely used structural efficiency metric for mass critical structures (Ashby 2011), such as aerospace structures and wind turbine blades. Specific strength is discussed in detail in Section 6.

Table 13. Specific Shear Strength of 3D-Printed Coupon Specimens

3D-Printed Core Material	Mean Shear Strength (MPa)	Nominal Density of Base Material (kg/m^3)	Specific Shear Strength (kNm/kg)
ABSCFF20	4.62	1,140.00	4.05
PRD-EX1631	4.51	860.00	5.24
PRD-EX1631-LS	1.74	860.00	2.02

5.12 Discussion

Large-scale, polymer-based, additive manufacturing processes using material extrusion exhibit a reduction in strength orthogonal to the bead direction due to a weak interlayer bond (Cincinnati Incorporated 2019). Reductions in tensile and compressive strengths of 3D-printed structures are reported (Duty, Drye, and Franc 2015) but little data are reported in public literature on shear strength, which is needed to design core structures. Fortunately, the shear requirements for core structures are modest, making 3D-printed core structures a good entry point for large-scale, polymer-based, additive manufacturing technologies.

To provide the shear properties required, a widely used and commercially available fiber-reinforced thermoplastic feedstock (Duty, Drye, and Franc 2015) is characterized for shear strength. Two additional developmental fiber-reinforced thermoset feedstocks are characterized to explore the potential of interlayer cross-linking to increase shear strength. Mean shear strengths of 4.62 MPa, 4.51 MPa, and 1.74 MPa are calculated from the test data for the 3D-printed ABSCCF20, PRD-EX1631, and PRD-EX1631-LS materials, respectively. In comparison to Gurit Balsaflex 150 balsa core with a mean shear strength of 2.8MPa (Gurit n.d.[b]), the 3D-printed polymer-based material shear strength appears comparable. However, as wind turbine blades are mass-critical structures, the density of the core material must be factored in.

Subsequently, designers of mass-critical structures refer to specific strength. Specific strength is addressed in more detail in the next section but is often used interchangeably with the strength-to-weight ratio as a measure of structural efficiency (Ashby 2011).

In comparison to the specific shear strength of balsa core, the 3D-printed materials are found to have considerably lower performance. Considering a specific shear strength of 18.06 kNm/kg for Gurit Balsaflex 150 balsa core, derived from a mean shear strength of 2.8 MPa and a density of 155 kg/m^3 (Gurit n.d.[b]) the specific shear strength of the 3D-printed materials, as calculated in Table 13 are significantly less. The ABSCCF20 feedstock with a calculated specific shear strength of 4.05 kNm/kg is found to have over four times less shear strength performance. The PRD-EX1631 thermosetting feedstock, with postdeposition cross-linking effects, is found to have improved shear strength performance versus the ABSCCF20 thermoplastic feedstock, but in comparison to balsa core it still has over three times less shear strength performance.

The reduced specific shear strengths of the 3D-printed polymer feedstocks are found to be largely attributable to the weak interlayer bond strength and the density of the extrudable polymer feedstock. The interlayer and interbead gaps, coupled with the internal bead porosities (Duty, Drye, and Franc 2015) are sure to play an additional role with crack initiation and debond, although they are less studied. Methods to improve the specific shear strength are met with challenges. For example, using higher chopped-fiber volume fractions to increase strength are a challenge due to the high polymer volume fraction requirements of the extruder. Reducing polymer density through foaming agents or expandable microspheres is difficult due to a proportional reduction in strength. Lowering the polymer viscosity to fill in the interlayer and interbead gaps is a challenge due to dimensional stability requirements. Heating an enclosed 3D printing chamber to improve interlayer polymer bonding is difficult due to high energy costs. And finally, obtaining material data is a challenge due to high testing costs and the time required.

It is understood that a limited data set is presented and that it is difficult to make definitive conclusions with such small sample sizes. There is no argument that additional coupon testing is needed. Much is still to be learned in characterizing shear properties for 3D-printed materials and standardization needs to be addressed along with additional coupon testing. The ASTM C273 standard might require modification and new or alternative standards may need to be developed. The structural adhesives needed to attach the polymer-based 3D-printed coupon specimens to the test fixtures may also need to be addressed depending on the specific monomer composition and the bond interactions between the polymer and adhesive (Quini and Marinucci 2012).

Despite the limited number of coupon specimens, the data provide an initial assessment of applying large-scale, polymer-based material extrusion technologies to the sandwich composite sections of high-performance wind turbine blade structures. The test results indicate that 3D-printed polymer-based coupon specimens with the materials tested are not competitive on a shear strength-to-weight basis with the incumbent solutions, such as balsa, foam, and honeycomb core. From a purely specific shear strength perspective, it is difficult to justify large-scale, polymer-based, material extrusion technologies using the polymer materials investigated. There is a large performance gap to overcome, and it is unknown if continued technological advancements can overcome these gaps, or if polymer-based honeycomb core-like solutions may be better addressed through alternate manufacturing processes such as injection molding, standard extrusion, or thermoplastic welding. Perhaps other polymer-based 3D-printing materials, such as

polyethylene terephthalate glycol formulations, may demonstrate higher specific strengths. Continued research and development is needed. However, even with lower specific shear strengths, the lower structural efficiency of the 3D-printed core may be offset by improvements made in other areas of the blade structure. For example, if the mass penalty associated with resin uptake in conventional balsa and foam cores can be lowered or eliminated with 3D-printed core structures, then a 3D-printed core may have an advantage. The potential to reduce resin uptake mass penalties and be competitive against the incumbent core solutions in the resin-infused state are investigated in the next section.

6 Techno-Economic Analysis

6.1 Introduction

We performed a techno-economic analysis to assess the technical and economic viability of a 3D-printed polymer-based honeycomb core within a wind turbine blade structure. Although the focus on the wind energy industry, the study applies to all industries that use sandwich composite structures.

Core material is an essential component in the sandwich composite sections of modern wind turbine blade structures. The core materials balsa wood, PVC foam, SAN foam, and PET foam discussed in previous sections are commonly adopted in modern wind turbine blades (Gurit n.d.[a]). End grain balsa with a nominal density of approximately 150 kg/m^3 is commonly used in the highly loaded inboard span of the blade for its high shear-stiffness-to-weight ratio and ability to resist shear crimping (Gurit n.d.[a]). Foam cores with lower shear-stiffness-to-weight ratios are commonly used in the less-loaded outboard spans of the blade to resist face-sheet dimpling and buckling failure modes as well as mitigate the higher resin uptake mass penalties associated with balsa (Gurit n.d.[a]). High-performance foams with improved mechanical properties and lower resin uptake penalties, such as Evonik's rohacryl polymethacrylimide (PMI) foam,[15] are less widely used due to higher material costs (Stoll 2014). Aerospace-grade aluminum honeycomb and Nomex honeycomb cores are not used in conventional wind turbine blades due to the high cost and manufacturing challenges associated with integrating them into the VARTM manufacturing processes used by the industry.

6.2 Specific Shear Strength

An important material metric used by designers of high-performance, mass-critical structures is specific strength (Ashby 2011), which is often used interchangeably with strength-to-weight ratio. Specific strength is not a dimensionless number and is calculated by dividing the material strength in pascals by the material density (kg/m^3) to get the specific strength expressed in units of 10^3 x N*m/kg, or kN*m/kg. The specific shear strength of commercially available balsa core, foam core, and honeycomb core materials is calculated using core shear strength data and core density data obtained from vendor. Specific shear strengths for core materials are calculated and shown in Table 14, and Figure 34. The specific shear strengths for balsa and foam cores are based on the vendor data for mean in-plane shear strength (τ_{12}) tested under the ASTM C273 standard (2020). The specific shear strengths for aluminum and Nomex honeycomb cores are based on the vendor data for in-plane shear strength in both the strong (τ_{12}) and weak (τ_{21}) directions tested using the ASTM C273 standard under the MIL-STD-401B standard (1967). Traditional honeycomb cores have a strong and weak direction due to how they are manufactured, resulting in a double-cell wall thickness in one direction, creating a manufacturing-induced anisotropy.

[15] https://composites.evonik.com/en/products-services/foams/rohacell

Shear strength is not typically presented for 3D-printed materials in vendor data sheets or otherwise and as such-3D printed core shear strengths are determined from material testing of fully dense, or near-zero-porosity, coupon samples under the ASTM C273 standard.

As described in Section 5, the mean ultimate shear strength values obtained by testing to failure are 4.62 MPa for the Electrafil J-1200/CF/20 ABS thermoplastic material, 2.88 MPa for the PRD-EX1631vinyl ester thermoset material, and 1.74MPa for the PRD-EX1631-LS low-shear-viscosity vinyl ester thermoset material, as shown in Table 14. The data in Figure 34 show the specific shear strengths of the fully dense 3D-printed samples to be significantly lower than commercially available core products.

Table 14. Specific Shear Strength (kNm/kg) Data for Core Materials

Core Product	Density (kg/m^3)	Shear Strength (MPa)	Specific Shear Strength (kNm/kg)
Gurit Balsaflex 150 (Balsa)[16]	155	2.8	18.06
Gurit Balsaflex Lite 150 (Balsa)[17]	155	2.8	18.06
Gurit Foam PVC 80 (PVC)[18]	80	1.2	15.00
Gurit Foam Corecell T400 (SAN)[19]	71	0.81	11.41
Gurit Foam Corecell T500 (SAN)[20]	94	1.2	12.77
Gurit Foam Kerdyn Green 80 (PET)[21]	80	0.59	7.38
Evonik Foam Rohacryl 80 (PMI)[22]	80	1.6	20.00
Toray Nomex Honeycomb ANC-4.8-48 (Strong Axis)[23]	48	1.20	25.00
Toray Nomex Honeycomb ANC-4.8-48 (Weak Axis)[24]	48	0.70	14.58
Toray Aluminum Honeycomb AAA-8.1-1/8-20N-5052 (Strong Axis)[25]	130	5.00	38.53
Toray Aluminum Honeycomb AAA-8.1-1/8-20N-5052 (Weak Axis)[26]	130	3.14	24.18
3D-Printed Core (Electrafil J-1200/CF/20 ABS Thermoplastic)[27]	1140	4.62	4.05

[16] (Gurit n.d.[b])
[17] (Gurit n.d.[b])
[18] (Gurit n.d.[c])
[19] (Gurit n.d.[d])
[20] (Gurit n.d.[d])
[21] (Gurit n.d.[e])
[22] (MatWeb 2023a)
[23] (Toray 2020a)
[24] (Toray 2020a)
[25] (Toray 2020b)
[26] (Toray 2020b)
[27] (Kim et al. 2018)

Core Product	Density (kg/m^3)	Shear Strength (MPa)	Specific Shear Strength (kNm/kg)
3D-Printed Core (PRD-EX1631 Vinylester Thermoset)[28]	860	4.51	5.24
3D-Printed Core (PRD-EX1631-LS Vinylester Thermoset)[29]	860	1.74	2.02

[28] (Polynt 2021)
[29] (Polynt 2021)

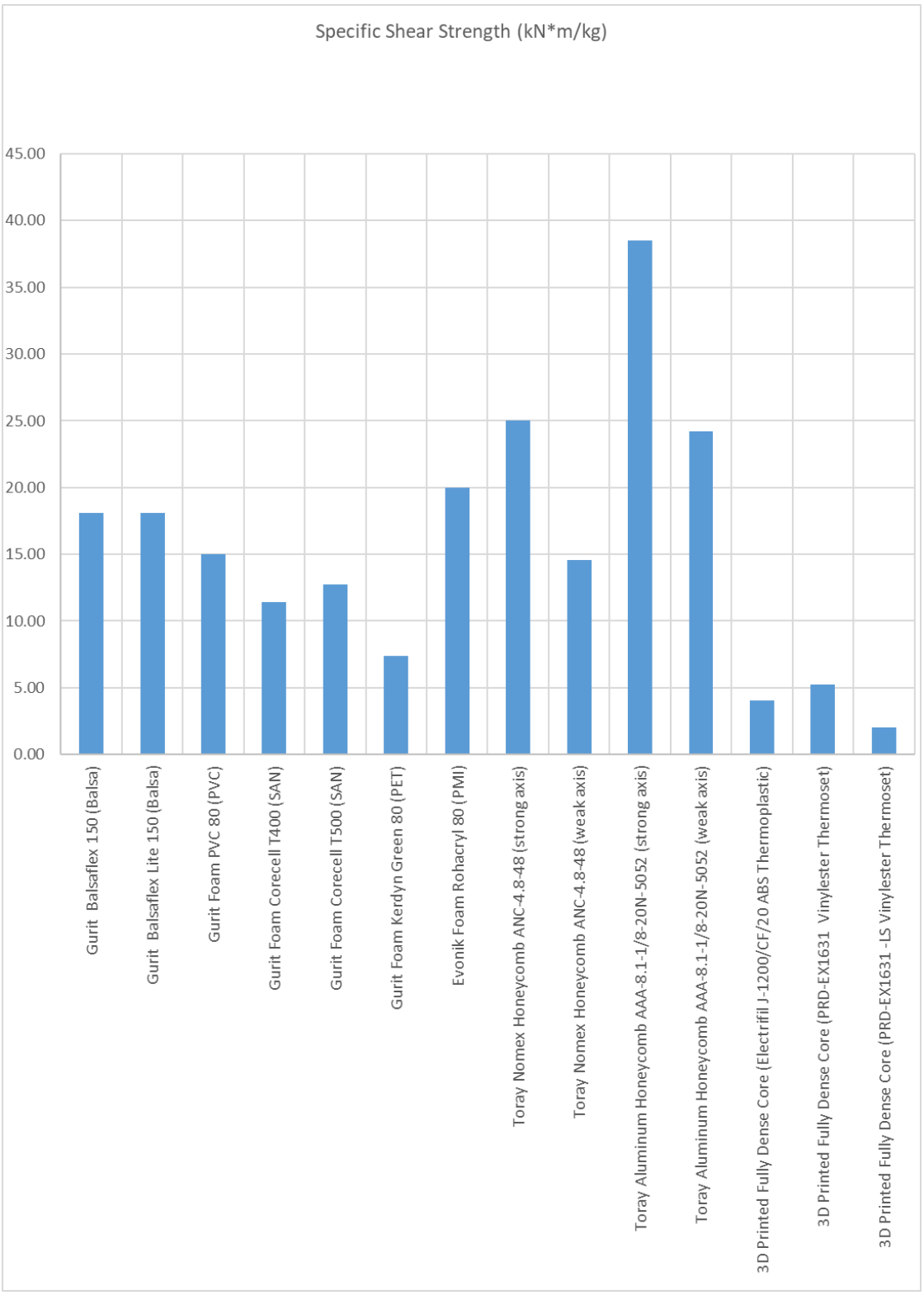

Figure 34. Comparison of specific shear strengths (kN*m/kg)

6.3 Relative Density

It is important to note that the specific strengths of the 3D-printed cores shown in Figure 6.1 are based on fully dense coupons with assumed near-zero porosity. Due to the base density of the polymer feedstock, high-porosity structures are required to meet blade core strength-to-weight metrics. Sparse, or honeycomb coupons with high porosity, will yield a lower shear strength, but also lower densities, which leads to another important metric in developing core structures: the relative density (Gibson and Ashby 1988). Relative density (ρ_R) is the relationship between the density of the final core structure (ρ_c) and the density of the solid material (ρ_s) used to make the core structure, as represented in the following equation:

$$\rho_R = \rho_c / \rho_s \tag{24}$$

The importance of this relationship is that it can be used to assist the designer in developing unit cell geometry as well as estimating the elastic and mechanical properties of 3D-printed core designs. Relationships involving relative density in terms of cell wall thickness (t) and cell wall length (l) for open- and closed-cell core structures have been described by Gibson and Ashby (1988). Additively manufactured core structures add another level of complexity due to bead-to-bead adhesion and the layer-by-layer deposition method. Material testing of both fully dense and sparse coupons is needed to obtain a greater understanding of the relationships between relative density and 3D-printed honeycomb core mechanical properties.

In the absence of material test data from sparse 3D-printed honeycomb coupons, it is assumed that mechanical properties are directly proportional to the relative density. To illustrate this principle, consider the case of tempered 5052 aluminum used in aluminum honeycomb cores. A 5052 aluminum with a H32 temper has a shear strength of approximately 138 MPa with a base density of 2,680 kg/m^3 (MatWeb 2023b). Now considering the Toray aluminum honeycomb with a core density of 130 kg/m^3, as found in Table 14, the relative density is calculated to be 0.048. Without knowledge of the core shear strength, a rough first-order approximation can be made. Multiplying the shear strength of the base 5052 aluminum material by the relative density results in an approximate aluminum honeycomb core shear strength of 6.7 MPa, which is in the ballpark of the vendor TDS data at 5.0 MPa and 3.14 MPa in the strong and weak directions, respectively (Toray 2020b).

Lacking material test data for sparse, high-porosity, 3D-printed honeycomb core structures, this first-order approach is taken for determining 3D-printed honeycomb core mechanical properties from the fully dense 3D-printed core material test data obtained through ASTM C273 testing. It is not exact but emphasizes the fact that further material testing is needed to improve and understand the correlation factors between fully dense and sparse 3D-printed honeycomb core structures.

6.4 Manufactured Core Specific Shear Strength

Another parameter that needs to be considered when comparing core materials is the infused core density. During the manufacture of sandwich composites, each category of core material will incur a manufacturing-induced mass penalty. In wind turbine blades, balsa and foam core will uptake resin into the wood fibers and open foam cells during the resin infusion process, resulting in excess resin mass trapped within the sandwich composite structure. Balsa and foam cores will

further entrap resin within the resin pass-through channels and the kerfs required for contouring rigid core panels. Sandwich composites with honeycomb cores are not typically manufactured using resin infusion but will incur a manufacturing-induced mass penalty through a different mechanism. Honeycomb cores require a thick adhesive to reduce stress concentrations and transfer the shear loads from the thin-walled honeycomb cells to the face sheets, resulting in an adhesive mass penalty. Finally, 3D-printed honeycomb cores will undoubtably incur some form of mass penalty depending on the design, material, and manufacturing process used. This mass penalty can occur through either resin uptake in high-porosity materials and pass-through channels, or through material buildup to alleviate stress concentration factors at bead-to-face-sheet transition zones, or through bonding the honeycomb cells to the face sheets.

Resin uptake values for PVC, SAN, and PET foam core materials are based on Gurit core products (Gurit 2019). Resin uptake values for PMI foam are based on data obtained from Evonik (2019). Foam core data are presented in Table 15 and assume a target product density of 80 kg/m^3 for comparison purposes. Resin uptake in foam core is assumed constant despite changes in thickness, which assumes the blowing agent used to manufacture the closed cell foam produces consistent cellular microstructure that allows resin uptake in the open or broken cells of the foam surface only.

Resin uptake for standard and coated balsa is obtained from Gurit balsa products and is assumed 1.7 kg/ m^2 for standard balsa and 1.2 kg/ m^2 for coated balsa (Gurit 2019), as shown in Table 15. Resin uptake for standard balsa core increases with core thickness due to the fibrous nature of the balsa wood. Fast-drying coatings are applied to balsa core at the manufacturer to limit the amount of resin absorbed into the wood fibers during infusion. As such, resin uptake for coated balsa core is assumed constant with core thickness.

Nomex and aluminum honeycomb cores are not infused, and thus have no resin uptake mass penalty. Instead, a mass penalty is assumed based on a film adhesive present on each side of the honeycomb core. The analysis assumes two plies of Toray MicroPly TC310 film adhesive with a weight of 0.293 kg/ m^2 per ply (Toray 2020c), as shown in Table 15.

The 3D-printed honeycomb cores, as shown in Figure 35, are considered to have three potential solutions to avoid resin from completely filling the open honeycomb cell during infusion. The first solution involves using 3D printing techniques, such as bridging and sparse-to-solid infills (Hershey et al. 2019) to cap the cells during the layer-by-layer deposition process. The mass penalty using this technique can be acceptable for thick core structures or if using very small nozzle diameters. However, for the sandwich composite core thicknesses and larger extruder nozzles required to manufacture large wind turbine blade cores, initial estimates indicate the number of layers required to make the transition from sparse to solid would add significant mass. The second solution is to cap the open cells using an adhesive film, for example. This approach would be challenging from a quality-control, adhesive-cost, resin-pass-through channel alignment, and general VARTM manufacturing process compatibility. The last solution, which initial estimates indicate offers the lowest mass and cost penalty, is to fill the open cells with an extremely low-density closed-cell foam, as shown in Figure 36. This foam will add mass due to additional material within the cell wall, as well as add resin uptake mass due to the open cells on the surface of the closed-cell foam. To quantify the mass penalty, the infill foam is assumed to have a density of 200 kg/m^3, as this is determined to be the lowest density foam achievable

within the constraints of current polymer-based, large-scale 3D printers (Kim et al. 2019; Roschli et al. 2018). We noted that lower-density foams may be achievable through a separate application process outside of the 3D printing process; however, extrudable foam using large-scale additive manufacturing is prioritized.

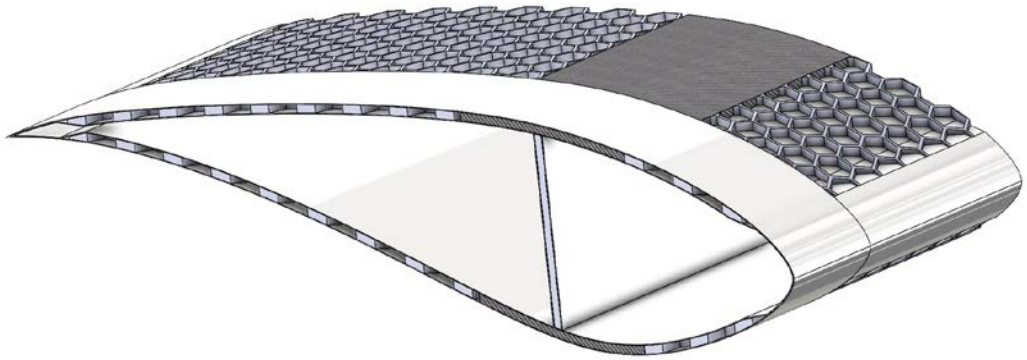

Figure 35. Conceptual representation of a 3D-printed honeycomb core within a wind turbine blade structure (top face sheet removed to view internal core). *Illustration created by W.S. Carron, NREL*

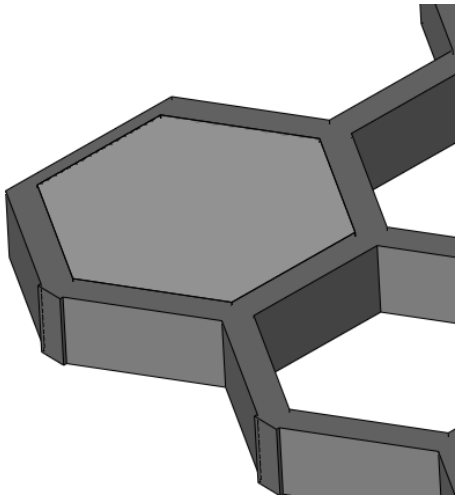

Figure 36. Conceptual representation of a 3D-printed honeycomb core unit cell with a low-porosity cell wall and high-porosity infill. *Illustration created by W.S. Carron, NREL*

To further assess 3D-printed honeycomb cores, we made the following assumptions. The cell wall of the thermoplastic-based honeycomb core unit cell is 3D printed with solid ABSCCF20 feedstock. The ABSCCF20 material is extruded from pelletized feedstock that has a base material density of 1,140 kg/m^3 (Kim et al. 2018). The porosity of the cell wall, or the volume fraction of voids within the ABSCCF20 bead volume, is assumed 0.0%. The porosity of the honeycomb unit cell volume assuming only a solid cell wall with no infill is 69.8%. The cell wall sizing assumes no structural contribution from the foamed infill. Cell sizing is based on the face-sheet dimpling failure mode with a maximum strain of 1.5% within the glass-fiber-reinforced polymer biaxial face sheets. The volumetric or bulk density of the cell wall without the foam

infill within the unit cell is calculated to be 344 kg/m^3 based on the following equation for porosity (P) assuming air-filled voids:

$$P = 1 - \left(\frac{\rho_{volumetric}}{\rho_{base\ material}}\right) \quad (25)$$

To prevent resin infill during infusion, the internal cavity of honeycomb core unit cell is 3D printed with a foamed ABSCCF20 feedstock. Expandable microspheres, such as Nouryon Expancel,[30] are assumed as the blowing agent within the ABS-based feedstock to produce a closed-cell ABSCCF20 foam with a density of 200 kg/m^3. The porosity of the foamed bead, or the volume fraction of voids within the foamed bead, is assumed as 82.5% to achieve the 200 kg/m^3 density from a base ABSCCF200 density of 1,140 kg/m^3. The porosity of the honeycomb unit cell volume assuming only the ABSCCF20 foamed infill with no cell wall present is 87.7%. The volumetric, or bulk density, of the unit cell with just the internal-foamed infill is calculated to be 140 kg/m^3.

Combining the porosity assumptions for the cell wall and the infill at the unit cell level yields a unit-cell volumetric density of 484 kg/m^3, as shown in Table 15. This bulk density assumes a contribution of 344 kg/m^3 from the ABSCCF20 cell wall and a140 kg/m^3 contribution from the ABSCCF20-foamed infill.

In comparison to the density of the ABSCCF20 feedstock, the relative density of the 3D-printed honeycomb core unit cell is calculated to be 0.425, which is derived from a base material density of 1,140 kg/m^3 and a volumetric cell density of 484 kg/m^3. The shear strength of 4.62 MPa, which was obtained from testing fully dense coupons, is adjusted downward by the relative density to obtain a shear strength value of 1.96 MPa for the 3D-printed honeycomb unit cell structure, as shown in Table 15. This is potentially optimistic as it assumes the entire unit cell, including the foam infill, carries the shear load. It must be noted that due to the differences in relative shear modulus between the solid cell wall and the internal foam, it is likely that only the solid cell wall will carry the shear load. In that case, the unit-cell shear strength would need to be further reduced from 1.96 MPa to 1.40 MPa.

We assumed the same process to determine the shear strength of the 3D-printed honeycomb core unit cell using the Polynt PRD-EX1631 and Polynt PRD-EX1631-LS thermoset feedstock. The same porosity is used except that the cell wall is 3D printed with a thermoset material with a base density of 860 kg/m^3. The volumetric, or bulk density, of the cell wall is calculated to be 260 kg/m^3. And the volumetric density of the internal-foamed infill is calculated to be 140 kg/m^3. Combining the porosity assumptions for the cell wall and the infill at the unit-cell level yields a unit-cell volumetric density of 400 kg/m^3 for the thermoset-based core, as shown in Table 15. The relative density of the 3D-printed honeycomb core unit cell is calculated to be 0.465, derived from a base material density of 860 kg/m^3 and a volumetric density of 400 kg/m^3. The shear strengths of 2.88 MPa and 1.74 MPa for the fully dense PRD-EX1631 and PRD-EX1631-LS thermoset coupons is adjusted downward by the relative density to obtain a shear strength value

[30] https://www.nouryon.com/products/expancel-microspheres/blowing-agents/

of 2.10 MPa and 0.81 MPa, respectively, for the 3D-printed thermoset honeycomb unit cell structure, as shown in Table 15.

The resin uptake mass for the 3D-printed foam infill is unknown and would require further testing and characterization. However, in the absence of data, the resin uptake for the foamed infill for all 3D-printed cores is assumed to be 2.18 kg/ m^2 (Table 15). This is double the resin uptake value of Gurit's Kerdyn 80 thermoplastic PET core (Gurit 2019). This increase in resin uptake is based on manufacturing differences between conventional foam sheets and 3D-printed foam. It is assumed that 3D-printed foamed ABSCCF20 with a 200 kg/m^3 density may retain more resin because of factors such as:

- Higher particle distribution of the expandable microspheres within the surface of the bead due to extruder shear
- Increased particle expansion uncertainty resulting from temperature gradients through the extruder
- More fluctuations in toolpath and deposition rates
- Greater irregularities in bead surface integrity, and the presence of bead-to-bead voids.

An additional mass penalty of 12 kg/m^3, as shown in Table 15, is added to the 3Dprinted honeycomb core density to account for the resin remaining in the pass-through channels required to transport resin between the top and bottom face sheets during infusion. This value is based on 3-mm diameter pass-through channels located every 25.4 mm throughout the core (Gurit n.d.[f]).

Because 3D-printed cores can be printed exactly to a contoured shape, the 3D-printed structures assume no kerfs as well as the associated mass penalty due to kerf resin entrapment. Traditional rigid balsa and closed-cell foam cores require kerfs for drapeability and assume a density increase of 50 kg/m^3 for resin entrapment within the kerfs (see Table 15). This value assumes an epoxy resin density of 1,200 kg/m^3 and approximately 4% of the total core volume due to expansion is filled with resin in the kerfs post infusion. We realized that thermoplastic-based closed-cell foam cores may be thermoformed to a shape, avoiding kerfing, but that the tooling and processing cost is assumed to be more than the kerf mass penalty.

Manufactured core specific shear strength data and assumptions for 12.7-mm core solutions are presented in Table 15 and Figure 37. There are several interesting conclusions that can be made when considering infused or manufactured core mass.

First, the calculated specific shear strength of infused 3D-printed honeycomb core is significantly less than aerospace Nomex and aluminum honeycomb core. Considering this large difference, it is unclear if continued research with layer-by-layer deposition using polymer-based extrusion can advance related technologies enough to be comparable to these products.

Second, the infused 3D-printed core specific shear strengths calculated are well below conventional balsa and foam cores used in wind turbine blades except for PET foam core. Despite this gap, and with continued research, 3D-printed honeycomb cores or 3D-printed panel stiffeners may find an entry point into the less loaded outer spans of the wind turbine blade

structure. There may also be an opportunity to incentivize 3D-printing research through potential advanced manufacturing production credits (Public Law 117-169 2022). Alternatively, 3D-printed honeycomb cores may be usable in markets with less demanding structural requirements.

Third, the infused specific shear strength calculated for PMI foam is higher than the calculated infused specific shear strength for balsa. This finding indicates that a more detailed techno-economic analysis on the inner spans of the blade where balsa is commonly used may reveal new opportunities for higher-cost PMI foams, and considering the evolving conditions surrounding supply chain shortages, domestic content, and inflation.

Finally, we must emphasize that the work presented on 3D-printed core structures is considered very early-stage research (i.e., low technology readiness level) based on a limited set of 3D-printed material coupon specimen data. Continued advancements in large-scale 3D printer materials and processes coupled with advancements in material characterization and process standardization are required to make more rigorous scientific conclusions.

Table 15. Manufactured Core-Specific Shear Strength Data and Assumptions

Core Product	Core Density (kg/m^3)	Core Thickness (mm)	Core Uptake/Adhesive Penalty (kg/m^2)	Core Uptake/Adhesive Density (kg/m^3)	Pass-Through Uptake Density (kg/m^3)	Kerf Uptake Density (kg/m^3)	Combined Density (kg/m^3)	Shear Strength (MPa)	Manufactured Core-Specific Shear Strength (kN*m/kg)
Gurit Balsaflex 150 (Balsa)	155	12.7	1.70	133.86	12	50	350.86	2.80	7.98
Gurit Balsaflex Lite 150 (Balsa)	155	12.7	1.20	94.49	12	50	311.49	2.80	8.99
Gurit PVC 80 (PVC)	80	12.7	0.62	48.82	12	50	190.82	1.20	6.29
Gurit Corecell T400 (SAN)	71	12.7	0.56	44.09	12	50	177.09	0.81	4.57
Gurit Corecell T500 (SAN)	94	12.7	0.46	36.22	12	50	192.22	1.20	6.24
Gurit Kerdyn Green 80 (PET)	80	12.7	1.09	85.83	12	50	227.83	0.59	2.59
Evonik Rohacryl 80 (PMI)	80	12.7	0.39	30.71	12	50	172.71	1.60	9.26
Toray Nomex Honeycomb ANC-4.8-48 (Strong Axis)	48	12.7	0.59	46.14	0	0	94.14	1.20	12.75
Toray Nomex Honeycomb ANC-4.8-48 (Weak Axis)	48	12.7	0.59	46.14	0	0	94.14	0.70	7.44
Toray Aluminum Honeycomb AAA-8.1-1/8-20N-5052 (Strong Axis)	130	12.7	0.59	46.14	0	0	176.14	5.00	28.39
Toray Aluminum Honeycomb AAA-8.1-1/8-20N-5052 (Weak Axis)	130	12.7	0.59	46.14	0	0	176.14	3.14	17.83

Core Product	Core Density (kg/m^3)	Core Thickness (mm)	Core Uptake/Adhesive Penalty (kg/m^2)	Core Uptake/Adhesive Density (kg/m^3)	Pass-Through Uptake Density (kg/m^3)	Kerf Uptake Density (kg/m^3)	Combined Density (kg/m^3)	Shear Strength (MPa)	Manufactured Core-Specific Shear Strength (kN*m/kg)
3D-Printed Honeycomb Core ABSCCF20 (Electrafil J-1200/CF/20 ABS Thermoplastic)	484	12.7	2.18	171.65	12	0	667.91	1.96	2.94
3D-Printed Honeycomb Core (PRD-EX1631 Vinyl Ester Thermoset)	400	12.7	2.18	171.65	12	0	583.15	1.34	3.59
3D-Printed Honeycomb Core (PRD-EX1631-LS Vinyl Ester Thermoset)	400	12.7	2.18	171.65	12	0	583.15	0.81	1.39

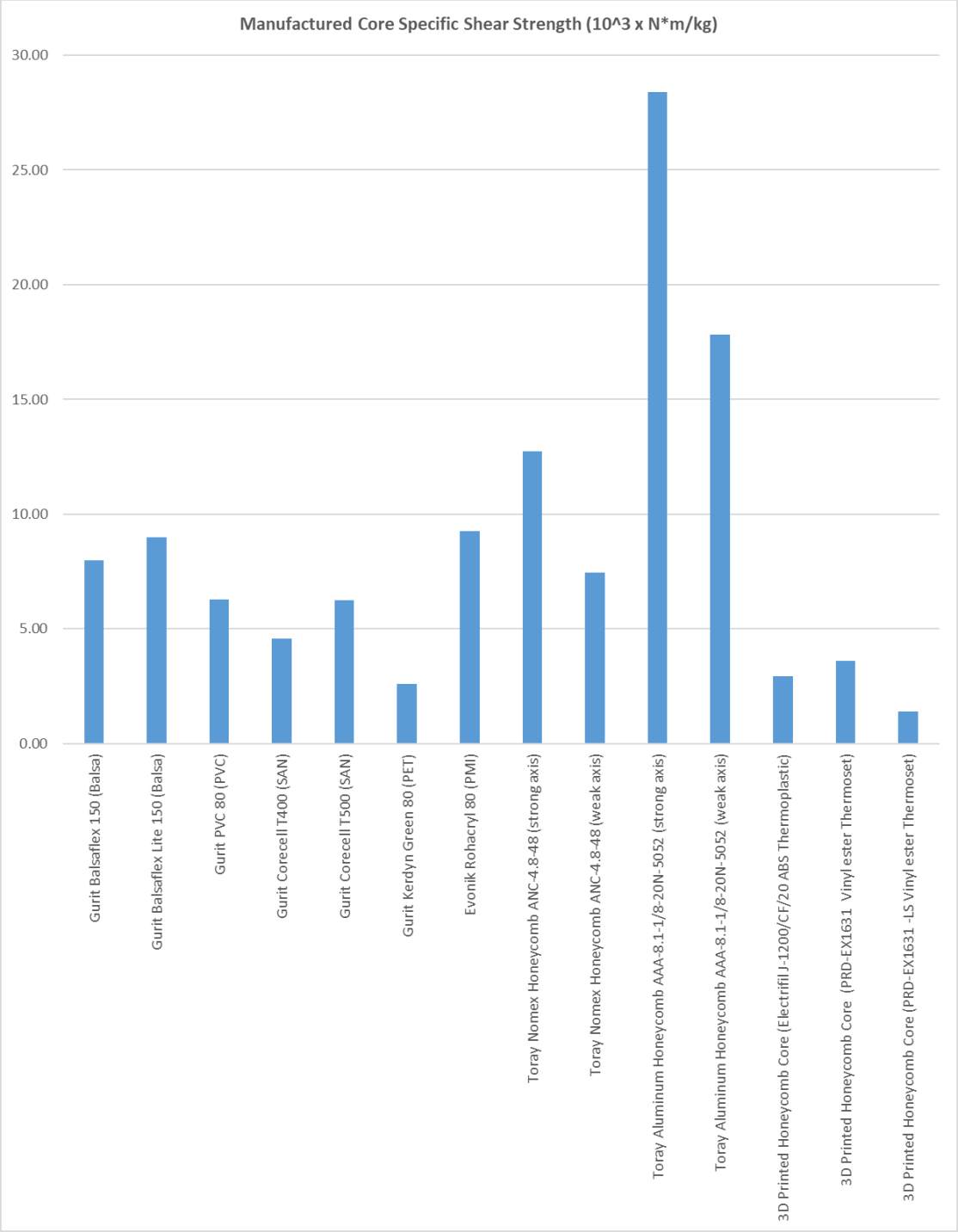

Figure 37. Comparison of manufactured core-specific shear strengths (10^3 x N*m/kg)

6.5 Resin-Infused Balsa Cost

The 13-m NRT blade (Ennis and Paquette 2015) is used as the basis for evaluating the techno-economic feasibility of a 3D-printed honeycomb core. Although small by modern-day standards, the 13-m blade is used as an open-source testbed within the research community due to its cost

effectiveness and scalability to larger blade platforms. A comparison between conventional balsa core and a 3D-printed honeycomb core based on the 13-m blade platform is presented.

The assumptions used to determine the cost of the infused balsa core are presented in Table 16. Balsa is the core material used throughout the sandwich composite sections of the 13-m blade. The balsa core regions within the 13-m blade skins are highlighted in red on the CAD model shown in Figure 38. The CAD model was created with SolidWorks using the 13-m NRT models and drawings. Preliminary studies indicate that the 3D-printed core is more applicable in the less loaded areas of the blade, as described in Section 5.4. As such, only the outer 7.09 m span of the 13-m blade skin containing the 6.35 mm thick balsa core is analyzed (Kelley 2020).

From the CAD model, we estimated that the outer 7.09-m span contains a total of 9.38 m^2 of balsa core. Considering a core thickness of 6.35 mm, the core volume is estimated at 0.06 m^3. The epoxy resin cost is estimated at $3.63/kg (Bortolotti et al. 2019b). The epoxy density was estimated at 1,200kg/m^3. Balsa core material cost for original equipment manufacturers is estimated at $1,023.62/$m^3$ (Bortolotti et al. 2019b) or $2.42 per board feet in North America. This estimate is based on a balsa core cost of $13/$m^2$ and assuming an average blade core thickness of 12.7 mm (Bortolotti et al. 2019b). This cost value is also vetted through the industry advisory committee (IAC). All costs, such as labor and operational costs incurred by the balsa supplier, are assumed to be included in the price. The balsa core resin uptake value of 1.2 kg/m^2 is based on the Gurit Balsaflex Lite 150 product, which is a resin-coated product that reduces resin uptake during the infusion process. The resin uptake value and the core thickness are used to estimate a volumetric resin uptake penalty for the balsa core of 188.98 kg/m^3.

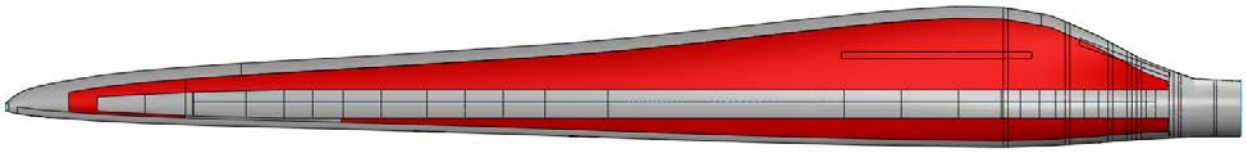

Figure 38. Sandwich composite sections of the 13-m NRT blade skin (shown in red). *Illustration created by W.S. Carron, NREL*

The resin pass-through channel density of 12.32 kg/m^3 is based on the resin filled volume of 1,081 equally spaced 3.0-mm-diameter perforations in a 1,220-mm-by-610-mm balsa panel (Gurit n.d.[f]).

Kerf cost is based on a resin density of 1,200 kg/m^3 and the resin filled volume of 24 knife-cut kerfs of 0.2 mm wide in both the length and width of a 1,220-mm-by-610-mm balsa panel to enable contour fitting within the blade mold (3A Composites 2020). The resin volume trapped in the kerfs is estimated at approximately 1.2% of the total panel volume. A kerf expansion factor of 3.5 is used to estimate a total kerf resin volume fraction of 4.2% while expanded in the blade mold. The total volume fraction is equivalent to an effective density of 50kg/m^3 attributable to the resin trapped in the kerfs.

Kitting cost is estimated as $10.00/$m^2$, which is based on information from an industry source, but also vetted through the IAC. Griffith and Johanns (2013) present a kitting cost estimate of $20/$m^2$, indicating there may be some variability based on supplier, process, and current market conditions.

Considering the assumption described earlier, the resin-infused cost of the balsa core is estimated at $209.10 for the outer span of the 13-m NRT blade. This total infused cost includes the balsa wood material, kitting costs, balsa core resin uptake, kerf resin uptake, and pass-through channel resin uptake, as broken down in Table 17, Figure 39, and Figure 40.

The costs shown in Figure 39 and Figure 40 clearly identify the potential opportunity for 3D-printed honeycomb core structures. As shown in Figure 39, the kitting and kerf costs represent approximately 50% of the total infused balsa core cost. As 3D-printed core structures would not incur kitting or kerf cost penalties, there is potential to reduce overall cost.

Due to the maturity of large-scale 3D printing with ABSCCF20, the 3D-printed honeycomb core solution is based on the ABSCCF20 feedstock.

It is important to note that the costs presented in this study are pre-2020. Labor, lumber, capital, and especially petrochemical-based products such as epoxy resin and polymer feedstock have all experienced significant cost increases since then. However, as this is a comparison study, it is assumed that cost adjustments due to inflation are not necessary to compare the two solutions.

Table 16. Resin-Infused Balsa Core Cost Assumptions

Cost Assumptions	Value	Unit
Epoxy Resin Cost	3.63	$/kg
Epoxy Resin Density	1,200.00	kg/m^3
Balsa Core Cost	2.42	$/board feet
Balsa Core Cost	1,023.62	$/m^3
Balsa Core Area	9.38	m^2
Balsa Core Thickness	6.35	mm
Balsa Core Volume	0.06	m^3
Balsa Core Resin Uptake (both surfaces)	1.20	kg/m^2
Balsa Core Resin Uptake Density	188.98	kg/m^3
Pass-Through Channel Diameter	3.00	mm
Pass-Through Channel Volume	44.89	mm^3
Pass-Through Channels per Sheet	1081	
Pass-Through Channel Resin Density	12.32	kg/m^3
Kerf Resin Volume Fraction	4.17	%
Kerf Resin Density	49.99	kg/m^3
Kitting Cost	10.00	$/m^2

Table 17. Resin-Infused Balsa Core Cost Assumptions

Total Cost Calculations	U.S. Dollars
Balsa Core Material Cost	$60.97
Balsa Core Kitting Cost	$93.80
Core Uptake Resin Cost	$40.86
Pass-Through Channel Resin Cost	$2.66
Kerf Resin Cost	$10.81
Total Infused Core Cost	$209.10

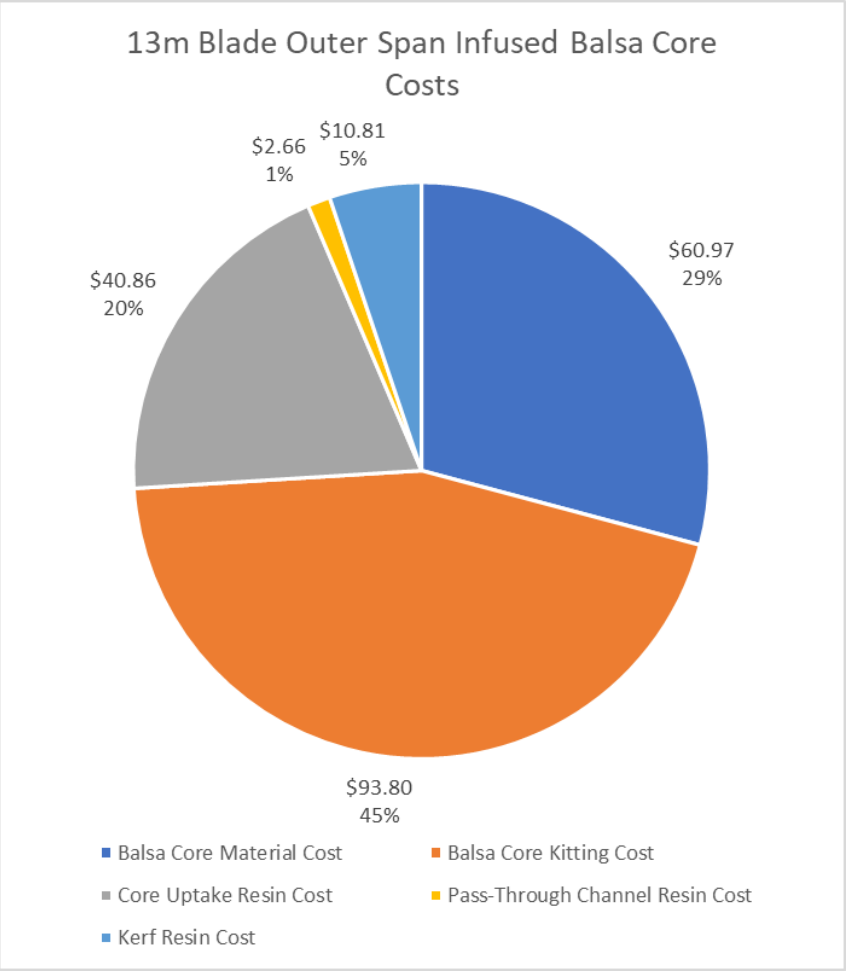

Figure 39. Resin-infused balsa core cost breakdown

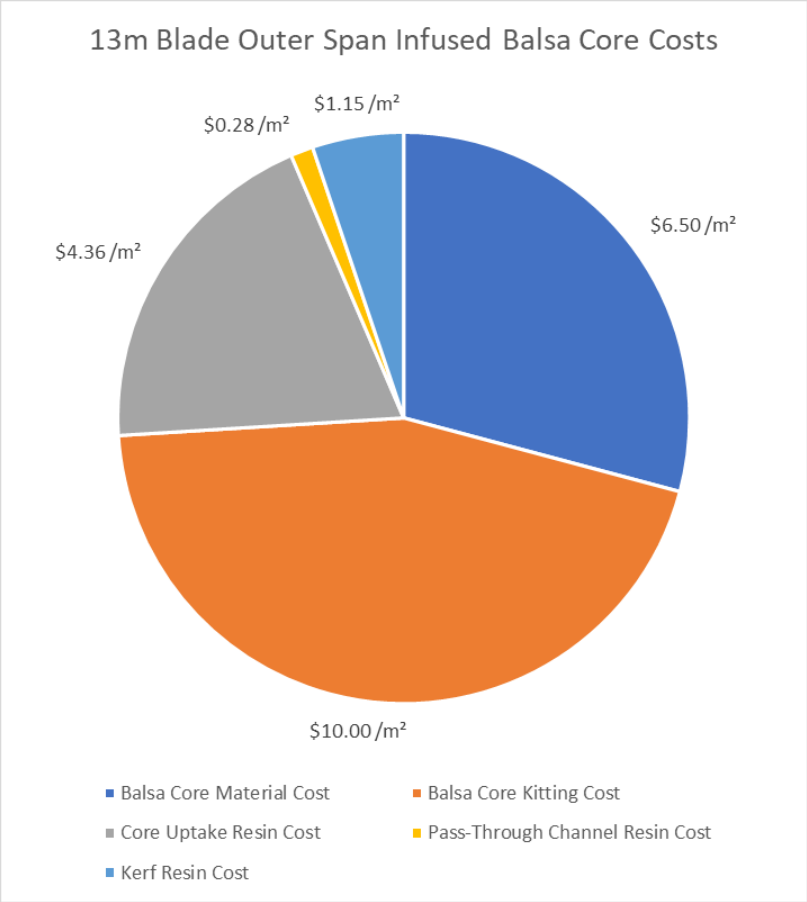

Figure 40. Resin-infused balsa core cost breakdown per area

6.6 Resin-Infused 3D-Printed Honeycomb Core Cost

To compare costs against the resin-infused balsa costs for the outer span of the 13-m NRT blade, we performed a detailed techno-economic analysis on a 3D-printed honeycomb core replacement solution, as presented in Section 5.4. The assumptions used in the analysis are listed in Table 38. The basis for many of the assumptions are covered in Section 5.4.

The ABSCCF20 feedstock cost is estimated at $11.02/kg. Foamed ABSCCF20 costs are increased to $13.22/kg to account for the assumed cost increase of adding expandable microspheres to the base feedstock.

The average deposition rate for 3D printing ABSCCF20 on the BAAM printer using a large 7.62-mm nozzle is estimated to be 22.68 kg/hour (hr) (Post et al. 2021; Roschli et al. 2019). Considering the complexities of a 3D-printed core and the need to use a smaller 5.08-mm nozzle for the cell wall, we assumed that the deposition rate for ABSCCF20 is reduced to 11.31kg/m^3 or approximately half. The deposition rate for foamed ABSCCF20 is assumed to be 22.68kg/m^3, as it is expected that higher rates can be achieved with the foamed infill and the larger 7.62-mm nozzle.

The large-scale 3D printer costs of $150.00/hr assumes a machine cost of roughly $1.5 million amortized over 7 years at 7% with 150 hours of use per month (Post et al. 2021). BAAM operator labor costs are estimated at a fully burdened rate of $35/hr (Post et al. 2021). Preprocessing and postprocessing times on the BAAM printer are assumed to be 15 minutes each due to assumed serial production efficiencies. BAAM-related consumable costs, such as the build plate, are assumed to be $100 per 3D-printed core Post et al. 2021). Large-scale CNC router costs required to machine the 3D printed core to tolerance is estimated at $50/hr and is based on an amortized machine cost of $500,000 (Post et al. 2021). Large-scale CNC router operator labor costs are estimated at a fully burdened rate of $35/hr (Post et al. 2021). Large-scale CNC router material removal rates are assumed to be .032 m^2/min roughly based on a 25.4-mm diameter end mill and a feed rate of 25.4 mm/second. A more accurate material removal rate will need to be quantified experimentally considering the ABSCCF20 material, layer-by-layer deposition, heat produced, depth of the cut, and various other machining considerations. Pre- and postprocessing times on the large-scale CNC are assumed to be 15 minutes each due to assumed serial production efficiencies (Post et al. 2021).

Table 18. 3D-Printed Honeycomb Core Cost Assumptions

3D-Printed Honeycomb Core Cost Assumptions	Value	Unit
Core Surface Area	9.38	m^2
Core Thickness	6.35	mm
Core Volume	0.06	m^3
Epoxy Resin Cost	3.63	$/kg
Epoxy Resin Density	1,200.00	kg/m^3
3D-Printed Core Resin Uptake (Both Surfaces)	2.18	kg/m^2
ABSCCF20 Feedstock	11.02	$/kg
ABSCCF20 Density	1,140.00	kg/m^3
ABSCCF20 Deposition Rate	11.31	kg/hr
ABSCCF20-Foamed Feedstock	13.22	$/kg
ABSCCF20-Foamed Density	200.00	kg/m^3
ABSCCF20-Foamed Deposition Rate	22.68	kg/hr
3D-Printed Honeycomb Cell Wall Porosity	0.698	
3D-Printed Honeycomb Cell Wall Density	344.74	kg/m^3
3D-Printed Honeycomb Cell Wall Mass	20.53	kg
3D-Printed Honeycomb Cell Wall Deposition Time	1.82	hr
3D-Printed Honeycomb Cell Wall Material Cost	226.28	$
3D-Printed Honeycomb Cell Infill Porosity	0.302	
3D-Printed Honeycomb Cell Infill Density	139.52	kg/m^3

3D-Printed Honeycomb Core Cost Assumptions	Value	Unit
3D-Printed Honeycomb Cell Infill Mass	8.31	kg
3D-Printed Honeycomb Cell Infill Deposition Time	0.37	hr
3D-Printed Honeycomb Cell Infill Material Cost	109.86	$
3D-Printed Honeycomb Core Resin Uptake Mass	20.45	kg
3D-Printed Honeycomb Core Resin Uptake Cost	74.23	$
3D-Printed Honeycomb Core Resin Pass-Through Channel Diameter	3.00	mm
3D-Printed Honeycomb Core Resin Pass-Through Channel Volume	44.89	mm^3
3D-Printed Honeycomb Core Resin Pass-Through Channels per Sheet	1,081	
3D-Printed Honeycomb Core Resin Pass-Through Channel Resin Density	12.32	kg/m^3
3D-Printed Honeycomb Core Resin Pass-Through Channel Resin Mass	0.73	kg
3D-Printed Honeycomb Core Resin Pass-Through Channel Resin Cost	2.66	$
3D-Printed Honeycomb Core Density	484.26	kg/m^3
3D-Printed Honeycomb Core Mass	28.84	kg
3D-Printed Honeycomb Core Deposition Time	2.18	hr
3D-Printed Honeycomb Core Material Cost	336.14	$
Large-Scale 3D Printer Hourly Cost	150.00	$/hr
Large-Scale 3D Printer Labor Costs (Fully Burdened)	35.00	$/hr
Large-Scale 3D Printer Preprocessing Time	0.25	hr
Large-Scale 3D Printer Postprocessing Time	0.25	hr
Large-Scale 3D Printer Consumables Costs	100.00	$
Large-Scale 3D Printer Operational Costs	402.29	$
Large-Scale 3D Printer Labor Costs	93.87	$
Large-Scale CNC Router Hourly Costs	50.00	$/hr
Large-Scale CNC Router Labor Costs (Fully Burdened)	35.00	$/hr
Large-Scale CNC Router Material Removal Rate	0.03	m^2/min
Large-Scale CNC Router Surfacing Time	4.85	hr
Large-Scale CNC Router Preprocessing Time	0.25	hr
Large-Scale CNC Router Postprocessing Time	0.25	hr
Large-Scale CNC Router Operational Costs	267.32	$
Large-Scale CNC Router Labor Costs	187.12	$

3D-Printed Honeycomb Core Cost Assumptions	Value	Unit
3D Printed Honeycomb Core Material Costs	513.03	$
3D Printed Honeycomb Core Operational Costs	669.61	$
3D Printed Honeycomb Core Labor Costs	280.99	$
3D Printed Honeycomb Core Total Infused Cost	1463.63	$
3D Printed Honeycomb Core Total Cycle Time	8.03	hr
3D Printed Honeycomb Core Total Infused Mass	50.03	kg

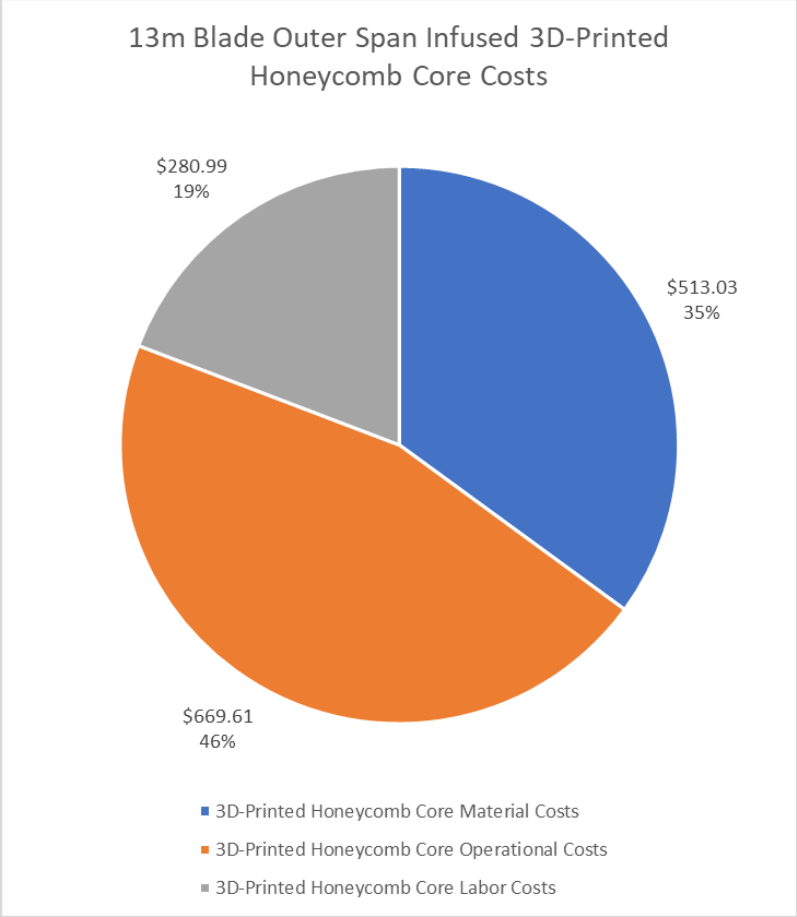

Figure 41. Resin-infused 3D-printed core cost breakdown

6.7 Core Storage Costs

To address all comparative advantages of a 3D-printed core, we investigated the benefits of just-in-time on-site manufacturing. The approach was to estimate blade core storage and staging costs based on a 70-m modern wind turbine and blade manufacturing facility. The relationships between core storage and staging costs and total blade cost for the 70-m blade were then applied

to the 13-m NRT blade. The storage and staging costs for the 13-m blade were then used to offset the total 3D-printed core costs, effectively reducing the 3D-printed honeycomb core cost.

Table 19 describes the assumptions used to determine storage costs. The out-the-door blade cost for the 70-m blade was based on the estimated cost of $154,090 for the 63-m International Energy Agency (IEA) land-based reference wind turbine blade (Bortolotti et al. 2019b). The blade cost is increased from $154,090 for the 63-m blade to $250,000 for the 70-m blade based on the additional 7 m of blade span, as well as an increase in the burdened labor rate from $20/hr to $35/hr (Bortolotti et al. 2019b). The blade manufacturing facility is assumed to produce 2,400 blades per year over six manufacturing lines, using internet-based research on blade manufacturing industry press releases during peak production, discussions with industry sources, research publications (Bortolotti et al. 2019b), and the IAC. We assumed that 60 days or 2 months of kitted blade core is kept as inventory on hand, which is based on balsa being an imported material and from discussions with an industry source. Rental cost for a 40-foot (ft) container on a long-term business lease is assumed at $115/month, which is based on discussions with an industry source. It is estimated that three sets of kitted blade cores can be stored in each 40-ft shipping container, which is based on a 40-ft container volume of 67.7m^3 (Reference 2020) and an estimate of 20 m^3 of core per 70-m blade (Bortolotti et al. 2019b). Because the 13-m NRT blade is a research blade the serial production costs are unknown. As a result, we estimated the 13-m blade cost to be $35,000, which is based on a blade mass of 537 kg material costs (Bortolotti et al. 2019b), and the labor and overhead costs to manufacture a prototype blade at a research facility. It is noted that lower serial production costs would decrease the relative cost savings; therefore, the 13-m NRT blade cost assumption of $35,000 is considered optimistic.

As shown in Table 19, traditional blade core storage costs are estimated at approximately .03% of the total blade cost. For a 70-m blade with an assumed out-the-door cost of $250,000, blade core storage costs are minimal and amount to approximately $76.67 per blade. Transferring this relationship to the 13-m NRT blade with an assumed out-the-door cost of $35,000, blade core storage costs would amount to approximately $10.73 per blade. Eliminating blade core storage costs effectively reduces the real 3D-printed core cost by $10.73. Considering the total infused cost estimate of the 13-m NRT core of $1,463.63, as shown in Table 18, a reduction of $10.73 translates into an effective savings of approximately 0.7%. Despite these positive results, larger cost savings are needed.

Table 19. Blade Core Storage Cost Savings assumptions

Blade Core Storage Costs	Value	Unit
Blade Length	70	m
Blade Cost	250,000.00	$
Blade Lines	6	

Blade Core Storage Costs	Value	Unit
Blades Manufactured (per Month)	200	blades/month (mo)
Blades Manufactured (annually)	2,400	blades/year (yr)
Blade Core Inventory in Storage	2	mo
Storage Container Size	40	feet
Storage Container Rental Cost	115.00	$/container/mo
Number of Blade Cores (per Container)	3	
Number of Storage Containers Required On-Site	134	
Blade Core Storage Costs (Monthly)	15,333	$/mo
Blade Core Storage Costs (Annual)	184,000.00	$/yr
Blade Core Storage Costs (per Blade)	76.67	$/blade
Blade Core Storage Costs (as a Percentage of Blade Cost)	0.03067	%
13-m NRT Blade Cost (Estimated)	35,000.00	$
13-m NRT Blade Core Storage Costs (per Blade)	10.73	$

6.8 Staging Costs

Table 20 describes the assumptions used to determine staging costs. Staging costs are based on the manufacturing floor space needed to stage the core material alongside the blade mold during manufacturing. Average industrial real estate rental costs across the United States are estimated at $75.00/m^2 based on information gathered from internet-based data (Shaver 2021; Popescu 2021). Although wind turbine blade manufacturing is often located outside city centers, it is realized that industrial real estate rental costs are market-driven and may be significantly higher based on location. The staging area is estimated at 20 m^2 and is based on a standard 40-ft shipping container and pallet dimensions for North America. Specifically, it is assumed that a 40-ft shipping container has an internal volume of 67.7 m^3 and a standard pallet has a footprint of 1.49 m^2. As three blade core kits are estimated to fit within a 40-ft container, it is assumed each blade core kit on average occupies an estimated 22.57 m^3 of volume. With an internal 40-ft container height of 2.39 m, the pallets are assumed to be stacked two high for an individual pallet height of 1.20 m. The total footprint of one blade core kit is estimated as 18.81 m^2 obtained by dividing the blade core kit volume by the pallet height. The footprint of 18.81 m^2 is increased to a staging area of 20.00 m^2 to provide additional margin and access.

As shown in Table 20, staging costs are estimated at .0015% of the total blade cost. For a 70-m blade with an assumed out-the-door cost of $250,000, blade core staging costs amount to approximately $3.75 per blade. For the 13-m NRT blade with an assumed out-the-door cost of $35,000, blade core staging costs would amount to approximately $0.53 per blade. Eliminating

blade core staging costs through just-in-time additive manufacturing effectively reduces the real 3D-printed core cost by $0.53Considering the total infused cost of the 13-m NRT core of $1,463.63, as found in Table 18, $0.53 is determined to be a negligible cost savings.

Table 20. Blade Core Staging Cost Assumptions

Blade Core Staging Costs	Value	Unit
Average Industrial Real Estate Costs (Annual)	75.00	$/m^2
Blade Core Staging Area	20	m^2
Number of Blade Manufacturing Lines	6	
Blade Core Staging Area Costs (Annual)	9,000	$/yr
Blades Manufactured (Annually)	2,400	blades/yr
Blade Core Staging Area Costs (per Blade)	3.75	$/blade
Blade Cost	250,000.00	$
Blade Core Staging Area Costs (As a Percentage of Blade Cost)	0.0015	%
13-m NRT Blade Cost (Estimated)	35,000.00	$
13-m NRT Blade Core Staging Area Costs (per Blade)	0.53	$

6.9 Discussion

We performed a technoeconomic analysis to compare the cost of a resin-infused balsa core against the cost of a comparable 3D-printed core. The analysis captures all of the relevant mass penalties associated with both cores in their final manufactured state.

As shown in Table 18, the resin-infused, 3D-printed honeycomb core cost within the sandwich composite sections of the outer span of the 13-m NRT blade is estimated at $1,463.63. In comparison, Table 16 shows the resin-infused balsa cost is estimated at $209.10.

The cost of the 3D-printed core solution is significantly more than the conventional balsa core. To assess whether there are viable pathways to close this cost gap, we investigated the individual cost components. As shown in Figure 41, most of the cost of the 3D-printed core solution, or approximately 81%, comes from machine and labor costs. As large-scale 3D printing machine capital costs are driven by steel tonnage, there is likely little wiggle room for significant cost decreases. However, there is potential in the future for automated 3D printing to eliminate labor, but that would only reduce the cost by $280.99, bringing the total 3D-printed part cost estimate down from $1,463.63 to $1,182.64. Even without the labor costs, a 3D- printed core is still projected to be over five times the cost of the conventional balsa solution.

In addition to the large cost increase, the mass increase for the infused 3D-printed honeycomb core against the balsa core is found to be roughly double. This mass increase is based on the ratio

of infused densities listed in Table 15 between coated balsa and ABSCCF20 3D-printed core, reported as 311.49kg/m^3 and 667.91kg/m^3, respectively. Efforts to reduce the mass of the 3D-printed honeycomb core by increasing or varying the cell wall diameter invited face-sheet dimpling failure modes in the blade skins.

There is the potential to use large-scale additive-manufacturing technologies on the blade manufacturing line to directly 3D print the core into the blade. A vision of a blade factory of the future with a fully autonomous manufacturing line is shown in Figure 42. In this scenario, blade core storage and staging costs would be eliminated. As such, blade core storage and staging costs at the manufacturer are explored to further assess all potential cost saving opportunities to offset the higher costs of a 3D-printed core. Any savings associated with eliminating these costs through large-scale, polymer-based, material extrusion technologies are found to be insignificant.

A direct comparison of the total bill of materials (BOM) costs between a wind turbine blade manufactured using conventional core materials versus 3D-printed core materials is not presented; however, it is not difficult to conclude that using a 3D-printed core solution with a higher cost structure will significantly increase the BOM costs. For example, for the IEA land-based reference wind turbine blade with a 130-m rotor, the balsa core cost is listed as roughly 23% of the total BOM cost, based on a balsa cost of $17,090.18 and a total BOM cost of $73,638.82 (Bortolotti et al. 2019b). If the balsa core is replaced with a 3D-printed core solution that is seven times more expensive, as shown in the techno-economic analysis, then the IEA land-based reference wind turbine blade BOM costs increase by approximately 139%, based on a new core cost of $119,631.26 and a new total BOM cost of $176,179.30.

Perhaps there are areas within the blade, such as at the blade tip, where the cost increase of 3D-printed structures might be justified. Findings indicate that the infused specific shear strength of the 3D-printed core is similar to a conventional PET foam core product. Or perhaps there are other design alternatives than the honeycomb approach explored in this analysis, such as stiffened panels, wherein the strength or stiffness reduction might be justified in the outer span of the blade. However, the takeaway is that to apply to mass-critical, high-performance, sandwich composite blade structures, manufacturing costs need to be driven significantly lower, and the specific shear strength of the 3D-printed material needs to be driven significantly higher. Transitioning the technology from rapid prototyping and tooling applications to 3D-printed core structures is challenging on both a cost and mass basis.

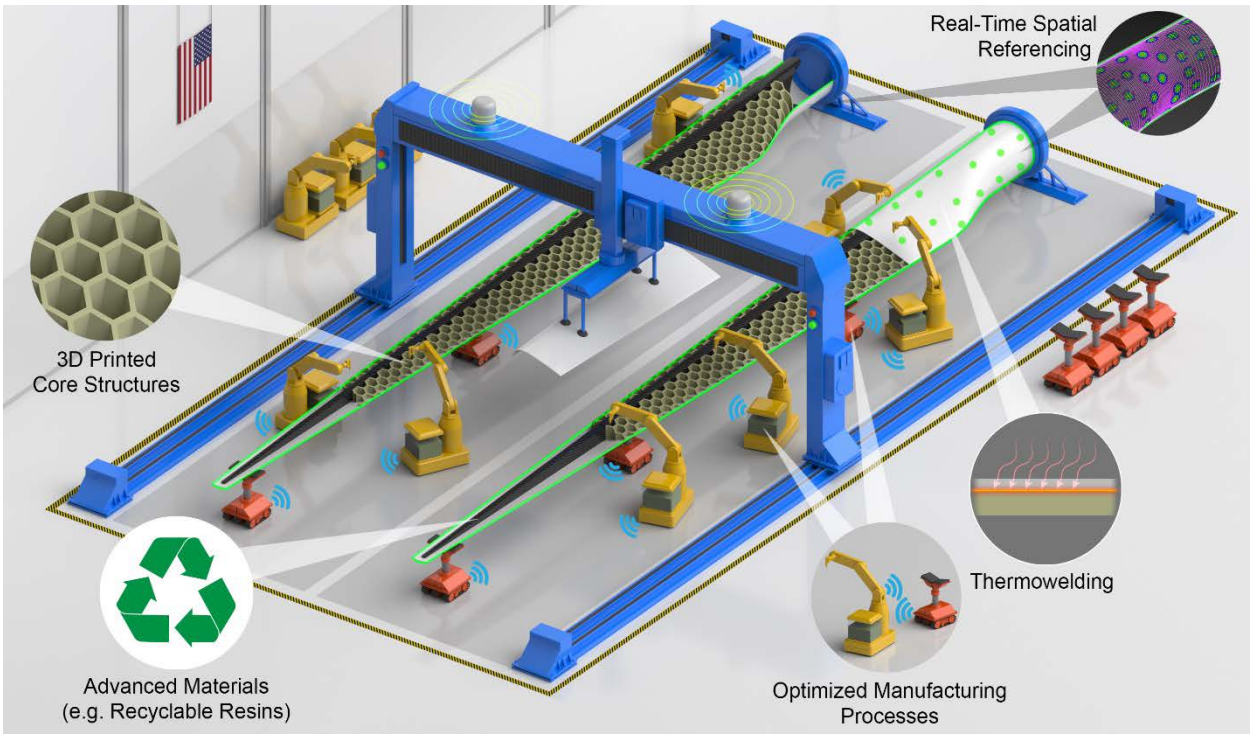

Figure 42. Vision of a factory with an automated blade manufacturing line. ***Illustration created by Besiki Kazaishvili and W.S. Carron, NREL***

7 Industry Advisory Committee

An IAC was assembled and convened in March 2022. The committee was comprised seven experts from the wind turbine blade industry and four experts from the additive manufacturing industry. A project overview is provided by the project team to the IAC along with a list of discussion questions. The purpose of meeting with the committee was to gather feedback to align the project team toward developing an innovative wind blade core that will be commercially viable for wind turbine blade manufacturing. A summary of the IAC feedback is documented as follows.

7.1 IAC Disclaimer

The following is the disclaimer provided to the IAC:

This advisory committee is a volunteer position, no travel is required, and input received from the committee should not contain any proprietary information (no nondisclosure or formal agreements are planned). The intent with this advisory committee is not to develop consensus, but rather to gather stakeholder input to help align this U.S.-Department-of-Energy-funded project toward impactful results for the wind turbine blade industry. Participating in this committee will provide you with insights into the research from this project. The goal of this advisory committee is to facilitate an exchange of information and facts, and to solicit and obtain your individual feedback to identify the most promising research pathways, required innovations, and areas most appropriate for research and development investment to overcome these challenges.

7.2 IAC Feedback Summary

The following is a summary of IAC feedback from the discussions in March 2022. The feedback is categorized by cost, material properties, innovation opportunities, and innovation risks:

- Cost:
    - New blade core materials and processing must offer a cost advantage over existing baseline balsa core to be used in commercial wind turbine blade manufacturing. Cycle time and BOM costs are most important in blade manufacturing with little room for anything but decreases in costs. A new blade core that increases BOM material cost must offset through labor savings to be feasible for commercial blade manufacturing.
    - The project team's \$23.45/m^2 cost target for a ¼-inch-thick 3D-printed blade core is a good target, considering 3D printing costs should go down with time. Research must remain financially grounded to have an impact on wind turbine blade manufacturing.
    - It is important to consider comprehensive cost models for core utilization in wind turbine blades, such as material and processing, transport, storage, factory floor space utilization, labor to position core into blade molds, resin uptake into core, and so on.
- Material properties:

- The core of a wind turbine blade has important structural properties including (but not limited to): local buckling resistance, strength and modulus for transverse and in-plane shear, shear-crimping resistance, face-dimpling resistance, and wrinkling resistance. Adhesive strength between the core and surrounding composite laminate and layer-to-layer strength within the core is important. Properties in all directions are important for the nonhomogeneous printed core.
- It is important to plan material testing at different scales (material properties at the microscale and structural properties at the macroscale). New blade core materials should be characterized first at the coupon level to evaluate performance and to make meaningful comparisons with baseline materials to assess performance. Then, core structures with face sheets should be mechanically characterized. Blade core mechanical properties are essential for blade designers. Fatigue properties of the blade core should be considered. Interlayer shear strength of 3D-printed material is particularly important.
- Temperature-related properties of the blade core include:
  - Heat-deflection temperature (i.e., capability of the printed core to maintain shape at elevated temperatures)
  - Coefficient of thermal expansion factors (i.e., avoid a gross mismatch with surrounding materials)
  - Glass-transition temperature (i.e., avoid low glass-transition polymers with printed core)

- Innovation opportunities with 3D-printed core for wind turbine blades (note: the following examples are only possibilities at this time, as research is required to qualify the opportunities):
  - Traditional blade core has many manufacturing variabilities, whereas 3D-printed blade core may reduce variabilities through an automated manufacturing process.
  - 3D printing may allow micro/macro porosity where needed. Targeted control and placement of porosities in a wind turbine blade core may lead to structural optimization.
  - Blade core must either conform to complex curved surfaces or be produced as the net shape. It may be possible to produce 3D-printed blade core into the net shape required for the blade core structure.
  - Contemporary methods for producing joints within a wind turbine blade structure are cheap but inefficient. A 3D-printed blade core may be more efficient and may enable on-site blade assembly in the field.
  - Custom design details in core such as thickness changes, chamfers, and edges may improve over baseline methods with 3D-printed core.
  - Optimizing 3D-printed core design may be possible based on directional properties analyzed with design loads.
  - If wind blade core 3D printing occurs within or near the blade manufacturing facility, then the supply chain may be simplified for general wind blade core.

- Innovation risks with 3D-printed core for wind turbine blades identified by the IAC include the following (note: the list of items brought up by the IAC is not intended to be comprehensive). The IAC expressed it is uncertain:
    - If net costs from 3D-printed blade core will improve the baseline core, which is essential to be a viable product for commercial wind turbine blade manufacturers
    - If 3D-printed blade core will have adequate mechanical properties. Thickening face sheets to compensate for inadequate core properties is counter-productive
    - If repeatable and acceptable material properties in the z-axis and between deposition layers can be achieved with a 3D-printed blade core
    - How 3D-printed blade core will scale (properties and cost) with larger wind turbine blade sizes
    - How 3D-printed core will compare with traditional blade core materials in thicker configurations (i.e., balsa is a very favorable baseline material as it has thicker 1-inch cores)
    - How 3D-printed blade core will withstand delamination of face sheets to the cellular core from hail or other impacts/defects
    - How a 3D-printed blade core made into a cellular structure will prevent filling with resin during vacuum infusion processing
    - How a 3D-printed blade core may influence end-of-life recycling options
    - If a 3D-printed blade core may add mass over baseline blades.

8 Technology Development Risks

The project risk management plan in Table 21contains some of the prioritized technical risks identified by the project team, along with the planned response, timing, recommendations, and action items. These risks may apply to a future project researching 3D-printed blade core. These risks do not consider other risks that may be important during a research project, such as those pertaining to resources, time, and scope management.

Table 21. Project Risk Management Plan

Risk	Risk Description **and** Impacts	Risk Priority	Risk Response	Risk Response Timing	Recommendations **and** Action Items
Structural Viability for Wind Turbine Blade Manufacturing	If 3D-printed core and sandwich do not at least meet requirements for balsa structural performance, then it may not offer any value as a core material for the wind turbine blade industry	High	Test 3D-printed core using standard test methods and compare to baseline metrics	As soon as possible; validation to metrics at each technology phase	1) Establish/reconfirm performance metrics 2) Validate against performance metrics at each technology phase
Economic Viability for Wind Turbine Blade Manufacturing	If the 3D-printed core net material and processing costs for wind turbine blade application costs more than baseline materials (balsa), then it may not offer any value as a core material for the wind turbine blade industry	High	Develop a techno-economic model (TEM) that assesses the overall costs for 3D-printed materials and processing, with comparisons to baseline methods, for wind turbine	TEM developed and maintained during each project quarter	1) Develop and maintain TEM throughout project using current data 2) Use TEM to inform technology development decisions throughout project

Risk	Risk Description **and** Impacts	Risk Priority	Risk Response	Risk Response Timing	Recommendations **and** Action Items
			blade manufacturing		
Shear Strength (per Unit Density) From 3D-Printed Core	3D-printed core shear strength-to-density must at least meet balsa to achieve project objectives	High	Understand current material properties, design effects, and then consider ways to improve it; consider effects from layer to layer and face sheets to core	ASAP	1) Characterize current best- candidate materials for thermoset and thermoplastics 2) If needed, develop plan to improve shear strength to density
3D-Printed Core Vacuum Integrity for VARTM	3D-printed core must have vacuum integrity to prevent leakage of resin during VARTM processing for wind turbine blade manufacturing	Medium	Develop and validate core design and processing that has vacuum integrity (past work with dual-head closed-cell foam may be a solution)	Validated at each project phase: sandwich, subcomponent, and blade core	1) Develop list of possible methods to produce 3D-printed core with vacuum integrity 2) Assess methods in TEM 3) Validate vacuum integrity throughout each relevant development phase
3D-Printed Core-Crushing Resistance from VARTM Vacuum Pressure	Printed core must not be crushed from vacuum pressure	Medium	Validate compressive strength of core from vacuum pressure	Validated at each project phase: sandwich, subcomponent, and blade core	1) Validate 3D-printed-core crushing resistance throughout each relevant development phase
3D-Printed Core With Curvature	Core for wind turbine blades must	Medium	Consider ways for core to	Validated at each project phase:	1) Develop list of possible methods to

Risk	Risk Description **and** Impacts	Risk Priority	Risk Response	Risk Response Timing	Recommendations **and** Action Items
	allow for curvature from an airfoil shape		have curvature (e.g., material compliance, printed with curvature, postprint machining)	subcomponent and blade core	enable core to comply with airfoil shape 2) Assess methods in TEM 3) Validate core curvature throughout each relevant development phase
Material Flow Rates for High- Volume Manufacturing	Material flow rates for 3D-printed core must be sufficient to enable an economically viable solution for wind turbine blade manufacturing; this risk is especially important if blade tooling is needed as a print surface	Medium	Model material deposition flow rates in TEM to understand economic impacts	Validated at each project phase: subcomponent and blade core	1) Develop TEM with flow rates 2) Consider ways to improve flow rates to improve economic viability in wind blade manufacturing
Cell Size for Microbuckling Resistance	The printed cell size must be large enough to meet density requirements, but not too large that micro-buckling occurs with the core and laminate	High	Consider this risk during 3D-printed cell design and extruder nozzle diameter selection	Validated at each project phase: sandwich, subcomponent, and blade core	1) Develop structural model (core and laminate) with core cell size and nozzle diameter as key parameters 2) Manage this risk while optimizing core design
Overall Recyclability of Core Material in Wind Blade	If balsa is replaced with a new 3D-printed core material, then overall wind blade	Low	Consider recyclability of new 3D-printed-core materials and	Considered at each project phase	1) Consider 3D-printed core material recyclability when evaluating materials

Risk	Risk Description **and** Impacts	Risk Priority	Risk Response	Risk Response Timing	Recommendations **and** Action Items
	recyclability could become more difficult (costly), or could be improved (less costly)		its impact on overall wind turbine blade recyclability		2) Consider recyclability of core materials in TEM
Core Compatibility With Infused Resin (Thermoset and Thermoplastic)	3D-printed-core material must be compatible with resin used during wind turbine blade skin infusion from VARTM processing otherwise there may be inadequate bonding between the core and skin, resulting in inadequate structural performance	High	Consider the core compatibility with VARTM resin before selecting materials; validate this compatibility by conducting structural testing of the core-to-facing bond	Validated at each project phase: sandwich, subcomponent, and blade core	1) Consider the core compatibility with VARTM resin before selecting materials 2) Validate material compatibility through structural testing sandwiches: • Static tensile strength of core-to-facing bond for sandwich (ASTM C297) (ASTM 2016c) • Static shear strength of core-to-facing bond for sandwich (ASTM C393) • Fatigue strength of core-to-facing bond for sandwich (ASTM C393)
Research Value Demonstration	A large-scale demonstration of technology developed through this project may not demonstrate	Medium	Plan research development to deliver research value at each project phase	Considered at each project phase	1) Plan research value delivered to wind industry at each project phase 2) Ensure research value delivered is

Risk	Risk Description **and** Impacts	Risk Priority	Risk Response	Risk Response Timing	Recommendations **and** Action Items
	research value to relevant external wind energy stakeholders				commensurate with costs to develop research
Fatigue Resistance	3D-printed core material must have acceptable fatigue resistance to be an acceptable wind blade core	Medium	Consider fatigue material characterization for 3D-printed-core materials as part of validation plans	TBD	1) Establish baseline metrics for balsa fatigue resistance 2) Develop fatigue test plans for 3D-printed-core material 3) Execute fatigue test plans
Field Wind Blade Repair	3D-printed blade core must be field repairable on an installed wind blade to be acceptable	Medium	Consider field repair methods for a wind turbine blade manufactured with a 3D-printed core	Subsequent project phases	Consider field repairability of 3D-printed blade core in subsequent project phases
Inspection Methods	There must be means to ensure the quality of a 3D-printed core is acceptable during blade manufacturing (e.g., under vacuum, during infusion, post cure)	Medium	Consider nondestructive inspection methods to ensure core quality during blade manufacturing	Subsequent project phases	Consider nondestructive inspection method development in subsequent project phases

9 Summary and Future Work

Two primary research pathways are described here to assess the techno-economic feasibility of a 3D-printed wind turbine blade core structure using large-scale polymer-based material extrusion technologies. First, a material characterization process is developed to determine the shear capacity of several 3D-printed core materials, including thermoplastics and thermosets. Second, a techno-economic model provides a comparative assessment of a 3D-printed core structure against commercially available core materials, including balsa core, using the 13-m NRT blade as a testbed. Results indicate additional research is needed in the areas of applicability, design for additive manufacturing, structural integrity, material science, and material characterization:

- Advancing additive manufacturing technologies from rapid prototyping and tooling applications into mass-critical, high-performance, wind turbine blade structural applications has unearthed many new challenges. Wind turbine blade designers need a full suite of material properties to assess the structural integrity of 3D-printed materials under static, fatigue, and buckling load conditions. In this work, obtaining the shear properties for the 3D-printed coupon specimens using the ASTM C273 test standard with common structural adhesives presented unexpected challenges. Despite these challenges, the preliminary test results using the ASTM C273 test methods showed a significant reduction in specific shear strength between the 3D-printed coupon specimens and conventional balsa core. In comparison to the specific shear strength of standard balsa core, the ABSCCF20, PRD-EX1631, and PRD-EX1631-LS 3D-printed materials showed a decrease of 77.6%, 71.0%, and 88.8%, respectively. In comparison to the specific shear strength of resin infused balsa core, ABSCCF20, PRD-EX1631, and PRD-EX1631-LS 3D-printed materials showed a decrease of 67.3%, 60.1%, and 84.5%, respectively. Foam cores were also investigated, and the 3D-printed materials were found to be more comparable to conventional PET foam core, indicating that lower-performance structures might be a better entry point for large-scale, polymer-based, material-extrusion additive technologies.

- Design for additive manufacturing is another area of interest that requires additional research and development. Exploring its potential in blade manufacturing to expand the design space, lower costs, reduce part count, decrease mass, reduce material testing times, and increase cycle times is easy to visualize. For example, topology optimization can be used to optimize core cell diameters, extruder nozzles can be changed to modify cell wall thicknesses, functionally graded materials can be used to optimize core densities, and core tapers, curvatures, and resin pass-through channels can be integrated directly into a single 3D-printed core. Realizing this potential is much more challenging. Each step of the additive manufacturing process will need to be qualified for each type of 3D printer including all the variable subprocesses and nuances, such as material properties, extruder dynamics, thermal signatures, deposition layer times, and nozzle diameters. Additional tools may need to be developed to reduce qualification times and cost as well as facilitate the implementation of design for additive manufacture into the blade design process.

- Of upmost concern for wind turbine blade structures is structural integrity. Using an additive manufacturing layer-by-layer deposition process introduces new risks. For large-scale, polymer-based, material-extrusion technologies to provide the structural integrity required for wind turbine blade structures, these risks need to be addressed. Continued research and development are needed on improving layer-to-layer strength while meeting wind turbine blade manufacturing cost metrics. Improvements in large-scale, polymer-based, material-extrusion technologies should include processes and methods that address voids and porosities within 3D-printed structures or investigate introducing matrix material to improve load transfer between beads and prevent crack initiation. It should also include continued research into extruder technologies that can deposit higher percentages, by volume, of fiber to enable high strength-to-weight ratio structures. Also, continued research should investigate reducing the cost and scaling up of alternate additive manufacturing technologies that can increase layer-to-layer strength, such as binder jetting, and polymer-based powder bed fusion. Finally high-performance structures commonly need secondary machining processes to meet tolerance specifications, and further research is needed on 3D printing near net shape structures and the impact of postprocessing on structural integrity and cost, such as thermal degradation, cooling lubricant, end mill dynamics, material removal rates, and the amount of time needed for subtractive operations.

- Material science is found to be another area in need of continued research and development to support large-scale, polymer-based additive manufacturing. Three-dimensional-printed polymer-based blade core structures require bonding methods to enable them to be both fixed to steel load plates for material characterization as well as integrated into larger blade structures. Current resin and structural adhesive chemistries do not consider the complexities of 3D-printed polymer-based feedstocks. Chemicals and additives may be included in the polymer feedstock to provide manufacturing improvements to the 3D-printed structure, such as dimensional stability, improved extrudability, increased heat retention, decreased densities, and reduced shear stress within the extruder nozzle. However, the impact of these additives versus neat polymers on the resin and structural adhesive systems needs to be investigated. New resin and structural adhesive formulations may need to be developed specifically for 3D-printed polymer-based materials. Additionally, the impact of these additives on the overall structural performance needs to be investigated. For example, adding chopped carbon fiber to increase the dimensional stability of a 3D-printed structure may reduce overall structural integrity under certain loading conditions due to fiber realignment or interface failures in the resin or adhesive.

- Perhaps the greatest area for continued research and development is in the field of 3D-printed material property characterization. For designers and engineers to use large-scale, polymer-based material extrusion as a method to manufacture advanced wind turbine blade structures, orthotropic 3D-printed materials properties are required at a minimum. Shear properties are needed in addition to tension and compression properties as the technology moves from tooling applications into blade structures with complex loading. The standard used by the industry to characterize shear strength and modulus of core materials is ASTM C273. Characterizing 3D-printed polymer-based coupon specimens using this method is found to be a challenge. As 3D-printed material characterization is

both costly and time-consuming, a combined effort in developing standards focused on 3D-printed materials and processes is needed. Additional resources are needed to develop new wind-turbine-specific standards such as adding partial material safety factors in IEC 61400-5 for 3D-printed materials. Less-costly and time-consuming alternatives that support the building-block approach to material property development is also merited. New models that can predict 3D-printed material properties based on base constituents and additive manufacturing processes can avoid costly coupon specimen testing, fast-tract preliminary design, and aid in certification by analysis. Continued research and development in material property characterization is considered essential in increasing the adoption of large-scale, polymer-based, material-extrusion technologies and unleashing the design potential of additive manufacturing through computational analysis and topology optimization tools.

In summary, the techno-economic analysis identified the opportunity space for additively manufactured wind turbine blade core structures. Advantages such as reducing resin uptake mass penalties and eliminating core kitting processes can lower costs, but higher manufacturing costs and weak interlayer strengths provide substantial headwinds. Continued research is needed to unlock the potential of additive manufacturing technologies to manufacture high-performance blade structures, enable longer blades, and drive down levelized cost of energy. Collaboration between standards committees, the research community, and the additive manufacturing, material science, and blade manufacturing industries is essential.

References

3A Composites. 2020. “Overview Finishing Options.” https://www.3accorematerials.com/zh/uploads/documents/25-03-20_CMA-Finishing-Options-210x297.pdf.

Ashby, Michael F. 2011. *Materials Selection in Mechanical Design*, 4th ed. Butterworth-Heinemann. ISBN 9781856176637. https://doi.org/10.1016/C2009-0-25539-5.

American Society for Testing and Materials. 2014 “Standard Test Method for Determining Strength of Adhesively Bonded Rigid Plastic Lap-Shear Joints in Shear by Tension Loading.” ASTM D3163-01. West Conshohocken, PA. https://www.astm.org/d3163-01r23.html.

___. 2016a. “Standard Test Method for Core Shear Properties of Sandwich Constructions by Beam Flexure.” ASTM C393/C393M-16. West Conshohocken, PA. https://www.astm.org/c0393_c0393m-20.html.

___. 2016b. “Standard Terminology of Adhesives.” ASTM D907-15. West Conshohocken, PA. https://www.astm.org/d0907-15.html.

___. 2016c. “Standard Test Method for Flatwise Tensile Strength of Sandwich Constructions.” ASTM C297/C297M-16. West Conshohocken, PA. https://www.astm.org/c0297_c0297m-16.html.

___. 2017. “Standard Test Method for Strength Properties of Adhesively Bonded Plastic Lap-Shear Sandwich Joints in Shear by Tension Loading.” ASTM D3164-03. West Conshohocken, PA. https://www.astm.org/d3164-03r17.html.

___. 2019. “Standard Test Method for Apparent Shear Strength of Single-Lap-Joint Adhesively Bonded Metal Specimens by Tension Loading (Metal-to-Metal).” D1002-10. West Conshohocken, PA. https://www.astm.org/d1002-10r19.html.

___. 2020. “Standard Test Method for Shear Properties of Sandwich Core Materials.” ASTM C273/C273M-20. West Conshohocken, PA. https://www.astm.org/standards/c273.

Baltek. 2014. “Baltek SB.” Data Sheet 10.2014. http://www.compositesone.com/wp-content/uploads/TDS-BALTEK-SB-E.pdf.

Berg, Jonathan, Josh Bryant, Bruce LeBlanc, Brian Naughton, Josh Paquette, Brian Resor, Jonathan White. 2013. “Scaled Wind Farm Technology Facility Overview.” American Institute of Aeronautics and Astronautics. https://energy.sandia.gov/wp-content/gallery/uploads/SAND2013-10632.pdf.

Borrega, M., P. Ahvenainen, R. Serimaa, L. Gibson. 2015. “Composition and structure of balsa (Ochroma pyramidale) wood.” *Wood Sci Technol* 49. https://link.springer.com/article/10.1007/s00226-015-0700-5.

Bortolotti, Pietro, Helena C, Tarres, Katherine L. Dykes, Karl Merz, Latha Sethuraman, David Verelst, and Frederick Zahle. 2019a. *IEA Wind TCP Task 37: Systems Engineering in Wind Energy - WP2.1 Reference Wind Turbines*. Golden, CO: National Renewable Energy Laboratory (NREL). NREL/TP-5000-73492. https://www.nrel.gov/docs/fy19osti/73492.pdf.

Bortolotti, Pietro, Derek S. Berry, Robynne Murray, Evan Gaertner, Dale S. Jenne, Rick R. Damiani, Garrett E. Barter, Katherine L. Dykes. 2019b. *A Detailed Wind Turbine Blade Cost Model*. Golden, CO: National Renewable Energy Laboratory (NREL). NREL/TP-5000-73585. https://www.nrel.gov/docs/fy19osti/73585.pdf.

Bortolotti, Pietro, Derek Berry, William Scott Carron, Todd Anderson, Molly Chann. 2023. "Toward the Advanced Manufacturing of Land-Based Wind Turbine Blades." Presented at the American Institute of Aeronautics and Astronautics, January 23-27, 2023. https://www.nrel.gov/docs/fy23osti/84397.pdf.

Callister, W. D. Jr. 2006. *Materials Science and Engineering: An Introduction, 7th Edition*. John Wiley & Sons, Inc.

Chapra, Steven C., and Raymond P. Canale. 2010. *Numerical Methods for Engineers*. Boston: McGraw-Hill Higher Education.

Cincinnati Incorporated. 2019. "Design Guidelines for BAAM." BAAM-Design-Guidelines.pdf (e-ci.com).

da Silva, Lucas Filipe Martins. 2008. Modeling of Adhesively Bonded Joints. Springer-Verlag Berlin. https://doi.org/10.1007/978-3-540-79056-3.

Det Norske Veritas. 2010. *Design and Manufacture of Wind Turbine Blades, Offshore and Onshore Wind Turbines*. DNV-DS-J102. https://rules.dnv.com/docs/pdf/dnvpm/codes/docs/2022-06/DS-J102.pdf.

Duty, Chad E., Tom Drye, and Alan Franc. 2015. *Material Development for Tooling Applications Using Big Area Additive Manufacturing (BAAM)*. Oak Ridge National Laboratory, United States. https://info.ornl.gov/sites/publications/files/Pub54566.pdf.

Ennis, Brandon Lee, and Joshua A. Paquette. 2015. *NRT Rotor Structural/Aeroelastic Analysis for the Preliminary Design Review*. Sandia National Laboratories, United States. https://www.osti.gov/servlets/purl/1225852.

Evonik. 2019. "Rohacryl - Findings from an independent study conducted by Aero Dynamik Consult GmbH - Resin uptake savings benefit wind blade designs."

Feng, J., J. Fu, Z. Lin, C. Shang, B. Li. 2018. "A review of the design methods of complex topology structures for 3D printing." *Vis. Comput. for Ind. Biomed. and Art* 1, 5 (2018). https://doi.org/10.1186/s42492-018-0004-3.

Gage, Bill, Michael Desmond, and Scott Hughes. 2019. *Static Proof Load Testing of the Sandia SWiFT 13m Blades*. Sandia National Laboratories, United States. https://www.osti.gov/servlets/purl/1567986.

Gage, Bill, Ryan Beach, and Scott Hughes. 2021. *Laboratory Wind Turbine Blade Static Testing of the Sandia National Rotor Testbed 13-Meter Wind Turbine Blade*. Golden, CO: National Renewable Energy Laboratory (NREL). NREL/TP-5000-79416. https://www.nrel.gov/docs/fy21osti/79416.pdf.

Gibson, L. J., and M. F. Ashby. 1988. *Cellular solids: Structure & properties*. Pergamon Press, Oxford.

Griffith, T., and W. Johanns. 2013. *Large Blade Manufacturing Cost Studies Using the Sandia Blade Manufacturing Cost Tool and Sandia 100-meter Blades*. Sandia National Laboratories. SAND2013-2734. https://energy.sandia.gov/wp-content/uploads/dlm_uploads/SAND_SNLLargeBladeManufacturingCostTrendsAnalysis_SAND2013-2734.pdf.

Gurit. 2019. "Core Materials: Processing Guide." Revision 5. https://www.gurit.com/wp-content/uploads/2022/09/structuralcoreprocessingguidere-2.pdf.

___. No date[a]. "Product Overview: Core Materials." Core Bro-21-0322. https://www.gurit.com/wp-content/uploads/2022/11/Core_brochure-2.pdf.

___. No date[b]. "Gurit Balsaflex: Balsa Wood Core Material." PDS-Balsaflex-12-0321. https://www.gurit.com/wp-content/uploads/bsk-pdf-manager/2022/08/balsaflex.pdf.

___. No date[c]. "Gurit PVC: Structural Foam Core." PDS-Gurit PVC-11-0618. https://www.gurit.com/wp-content/uploads/2022/11/gurit-pvc-1.pdf.

___. No date[d]. "Gurit Corecell T: Structural Foam Core." Gurit Corecell T-13-0618.

___. No date[e]. "Gurit Kerdyn Green: Recyclable Structural Foam." PDS-Kerdyn Green-9-0521. https://www.gurit.com/wp-content/uploads/2023/01/Kerdyn-Green-product-sheet.pdf.

___. No date[f]. "Gurit Balsaflex." Balsaflex Bro-2-0315. https://mobile.gurit.com/-/media/gurit/datasheets/balsa-brochure.pdfHamdi, Marouen, Mohamed Nasr Saleh, and Johannes A. Poulis. 2020. "Improving the adhesion strength of polymers: effect of surface treatments." *Journal of Adhesion Science and Technology*, 34:17, 1853-1870, DOI: 10.1080/01694243.2020.1732750. https://doi.org/10.1080/01694243.2020.1732750.

Hassen, Ahmed Arabi, Robert Springfield, John Lindahl, Brian Post, Lonnie Love, Chad Duty, Uday Vaidya, R. Byron Pipes, Vlastimil Kunc. 2016. "The Durability of Large-Scale Additive Manufacturing Composite Molds." Presented at CAMX – The Composite and Advanced Materials Expo, Anaheim, CA. https://www.researchgate.net/publication/324391116_The_Durability_of_Large-Scale_Additive_Manufacturing_Composite_Molds.

Hershey, Christopher, John Lindahl, Stian Romberg, Alex Roschli, Ben Hedger, Mike Kastura, Brett Compton, and Blastimil Kunc. 2019. "Large-Scale Reactive Extrusion Deposition of Sparse Infill Structures with Solid Perimeters." United States. https://www.osti.gov/servlets/purl/1570906.

Hoff, N. J. and S. E. Mautner. 1945. "The Buckling of Sandwich Type Panels." *Journal of the Aeronautical Sciences*, Vol. 12, No 3, pp 285-297. https://doi.org/10.2514/8.11246.

International Electrotechnical Commission. 2005. "Wind turbines - Part 1: Design requirements." IEC 61400-1. Third edition. https://webstore.iec.ch/preview/info_iec61400-1%7Bed3.0%7Den.pdf.

___. 2014. "Wind turbines – Part 23: Full-scale structural testing of rotor blades." IEC 61400-23. https://webstore.iec.ch/preview/info_iec61400-23%7Bed1.0%7Den.pdf.

___. 2019. "Wind energy generation systems – Part 1: Design requirements." IEC 61400-1. Fourth edition. https://webstore.iec.ch/publication/64648.

___. 2020. "Wind energy generation systems - Part 5: Wind turbine blades." IEC 61400-5:2020. https://webstore.iec.ch/publication/33236.

Joglekar, Anand M. 2003. *Statistical Methods for Six Sigma: In R&D and Manufacturing*. Hoboken: John Wiley & Sons, Incorporated. https://www.wiley.com/en-us/Statistical+Methods+for+Six+Sigma:+In+R&D+and+Manufacturing-p-9780471203421.

Kelley, Chris. 2020. "NRT Design and Testing Documentation." GitHub. https://github.com/ckelley2/NRT.

Kim, Seokpum, Gregory D. Dreifus, Bentley T. Beard, Andrew Glick, Andrew K. Messing, Ahmed A. Hassen, John M. Lindahl, Peng Liu, Tyler Smith, Jordan A. Failla, Brian K. Post, John C. Bowers, Kenneth Stephenson, Lonnie J. Love, and Vlastimil Kunc. 2018. "Graded Infill Structure of Wind Turbine Blade Accounting for Internal Stress in Big Area Additive Manufacturing." https://www.osti.gov/servlets/purl/1479756.

Krishnamoorthy, Kalimuthu, and Thomas Mathew. 2009. *Statistical Tolerance Regions: Theory, Applications, and Computation*. Wiley. Hoboken. https://onlinelibrary.wiley.com/doi/book/10.1002/9780470473900.

Kumar, S., and K. Mittal. 2013. *Advances in Modeling and Design of Adhesively Bonded Systems*. Wiley. https://onlinelibrary.wiley.com/doi/book/10.1002/9781118753682.

Kunc, V., J. Ikka, S. Voeks, J. Lindahl. 2019. *Vinylester and Polyester 3D Printing*. Oak Ridge, TN. Oak Ridge National Laboratory. https://info.ornl.gov/sites/publications/Files/Pub120300.pdf.

Love, Lonnie. 2015. "3D Printed Shelby Cobra." Oak Ridge, TN: Oak Ridge National Laboratory. https://www.osti.gov/sciencecinema/biblio/1330345.

MatWeb. 2023a. “Evonik ROHACELL 80 WIND-F Polymethacrylimide Foam.” https://www.matweb.com/search/DataSheet.aspx?MatGUID=73dffc32ed2645d58264bb10bfe82379&ckck=1.

___. 2023b. “Material Property Data, Aluminum 5052-H32.” https://www.matweb.com/search/DataSheet.aspx?MatGUID=96d768abc51e4157a1b8f95856c49028&ckck=1.

Meink, T. E. 1998. “Composite grid vs. composite sandwich: a comparison based on payload shroud requirements.” 1998 IEEE Aerospace Conference Proceedings (Cat. No.98TH8339). Vol. 1. IEEE, 215–220 vol.1. 10.1109/AERO.1998.686820. https://ieeexplore.ieee.org/abstract/document/686820.

Murray, Robynne, Jason Roadman, and Ryan Beach. 2019. “Fusion joining of thermoplastic composite wind turbine blades: Lap-shear bond characterization.” *Renewable Energy*, Volume 140, 2019, Pages 501-512, ISSN 0960-1481. https://doi.org/10.1016/j.renene.2019.03.085.

Murray, Robynne, Ryan Beach, David Barnes, David Snowberg, Derek Berry, Samantha Rooney, Mike Jenks, Bill Gage, Troy Boro, Sara Wallen, Scott Hughes. 2021. “Structural validation of a thermoplastic composite wind turbine blade with comparison to a thermoset composite blade.” *Renewable Energy*, Volume 164, 2021, Pages 1100-1107, ISSN 0960-1481, https://doi.org/10.1016/j.renene.2020.10.040.

Norris, C. B. 1964. *Short-column compressive strength of sandwich constructions as affected by size of cells of honeycomb core materials*. U.S. Forest Service Research Note FPL- 026, Forest Product Laboratory, Wisconsin. https://www.amazon.com/-/he/Norris-C-B/dp/B09SHTV3DV.

Oñate. 2013. *Structural Analysis with the Finite Element Method. Linear Statics.* Springer Netherlands. Volume 2: Beams, Plates and Shells (1st ed. 2013.). https://doi.org/10.1007/978-1-4020-8743-1.

Polynt. 2021.“PRD-EX1631: Thermoset Print Media for Low Density Additive Manufacturing.” Product Bulletin.

Popescu, A. 2021. “CommercialEdge National Industrial Report February 2021.” CommercialEdge. https://www.commercialedge.com/blog/commercialedge-national-industrial-report-february-2021/.

Post, Brian K., Bradley Richardson, Randall Lind, Lonnie J. Love, Peter Lloyd, Vlastimil Kunc, Breanna J. Rhyne, Alex Roschli, Jim Hannan, Steve Nolet, Kevin Veloso, Parthiv Kurup, Timothy W. Remo, and Dale S. Jenne. 2017a. “Big Area Additive Manufacturing Application in Wind Turbine Molds, Solid Freeform Fabrication 2017.” Proceedings of the 28th Annual International Solid Freeform Fabrication Symposium – An Additive Manufacturing Conference, United States. 74522.

Post, Brian, Bradley Richardson, Peter Lloyd, Lonnie Love, Stephen Nolet, James Hannan. 2017b. *Additive Manufacturing of Wind Turbine Molds*. Oak Ridge, TN: Oak Ridge National Laboratory. ORNL/TM-2017/290, CRADA NFE-16-06051, doi:10.2172/1376487. https://info.ornl.gov/sites/publications/Files/Pub75291.pdf.

Post, B., B. Richardson, S. Palmer, L. Love, D. Lee, P. Kurup, T. Remo, D. S. Jenne, M. Mann. 2017c. *The Current State of Additive Manufacturing in Wind Energy Systems*. Oak Ridge, TN: Oak Ridge National Laboratory, ORNL/TM-2017/479. https://info.ornl.gov/sites/publications/Files/Pub103095.pdf.

Post, Brian, Celeste Atkins, Amiee Jackson, Phillip Chesser, Alex Roschli, Abby, Barnes, Andrzej Nycz, Luke, Meyer, Peter, Jensen, Martin, Vcelka, Scott Carron. 2021. *A Comparative Study of Direct and Indirect Additive Manufacturing Approaches for the Production of a Wind Energy Component*. Oak Ridge, TN: Oak Ridge National Laboratory. ORNL/SPR-2021/1095. doi:10.2172/1809969. https://info.ornl.gov/sites/publications/Files/Pub154003.pdf.

Public Law 117-169. 2022. https://www.govinfo.gov/content/pkg/PLAW-117publ169/pdf/PLAW-117publ169.pdf.

Quini, Josué, and Gerson Marinucci. 2012. "Polyurethane structural adhesives applied in automotive composite joints." *Materials Research*. 15. 434-439. https://doi.org/10.1590/S1516-14392012005000042.

Reference. 2020. "How Many Cubic Meters Are in a 40-Foot Container?" https://www.reference.com/science-technology/many-cubic-meters-40-foot-container-254e8fb7f0d1dddc.

Roschli, Alex C., Phillip C. Chesser, and Lonnie J. Love. 2018. *Additive Manufacturing for Highly Efficient Window Inserts CRADA Report*. Oak Ridge, TN: Oak Ridge National Laboratory. ORNL/LTR-2018/484. https://www.osti.gov/servlets/purl/1436039.

Roschli, Alex, Katherine T. Gaul, Alex M. Boulger, Brian K. Post, Phillip C. Chesser, Lonnie J. Love, Fletcher Blue, Michael Borish. 2019. "Designing for Big Area Additive Manufacturing." *Additive Manufacturing*, Volume 25, 2019, Pages 275-285, ISSN 2214-8604. https://doi.org/10.1016/j.addma.2018.11.006.

Shaver, L. 2021. "Industrial Pricing Jumps to $145 Per Square Foot." *GlobeSt.com*. https://www.globest.com/2021/03/11/industrial-pricing-jumps-to-145-per-square-foot/?slreturn=20221023160219.

Stoll, Frederick. 2014. "Optimal Design of Sandwich Core for Wind Turbine Blade Buckling Resistance." 32nd ASME Wind Energy Symposium. 10.2514/6.2014-0175. https://arc.aiaa.org/doi/10.2514/6.2014-0175.

Sutherland, Herbert, and Paul S. Veers. 1999. "The Development of Confidence Limits for Fatigue Strength Data." 19th Wind Energy Symposium, American Society of Mechanical Engineering, Reno, NV. https://www.osti.gov/biblio/14833.

Tadich J. K., J. Wedel-Heinen, and P. Petersen. 2005. "New guidance for the development of wind turbine blades." Det Norske Veritas – Global Wind Energy Conference, Copenhagen, Denmark. https://www.semanticscholar.org/paper/New-guidance-for-the-development-of-wind-turbine-Tadich-Wedel-Heinen/a204c1db27fa55f875e11105ab9a3eac9cd9b226.

Toray. 2020a. "Nomex Honeycomb: Commercial Grade." NomexHC-Comm_PDS_v7_2020-06-12. https://www.toraytac.com/media/30396566-fe5f-4b41-8efb-9ee196e8c846/IRmINQ/TAC/Documents/Data_sheets/Adhesives_and_Core/Honeycomb_core/Nomex-Honeycomb-Core-Commercial-Grade_PDS.pdf.

___. 2020b. "Aluminum Honeycomb: Aerospace Grade." AlumHC-Aero_PDS_V10.1_2020-01-22. https://www.toraytac.com/media/b87edd4f-ad6e-470f-9d40-1faf98a28323/Vv6QeA/TAC/Documents/Data_sheets/Adhesives_and_Core/Honeycomb_core/Aluminum-Honeycomb-Core-Aerospace-Grade_PDS.pdf.

___. 2020c. "Toray MicroPly TC310." TORAY_MicroPly_TC310_PDS_v4.0_2020-02-28. https://www.toraytac.com/media/10583e68-10ed-4952-8cad-c20025329165/WQq1hA/TAC/Documents/Data_sheets/Adhesives_and_Core/Film_adhesives/MicroPly%20TC310_Epoxy_PDS.pdf.

Turner, M. J., and Grande, D. L. 1978. *Study of Advanced Composite Structural Design Concepts for an Arrow Wing Supersonic Cruise Configuration*. National Aeronautics and Space Administration, CR-2825. https://apps.dtic.mil/sti/pdfs/ADA305026.pdf.

U.S. Department of Defense. 1967. "MIL-STD-401B, Military Standard: Sandwich Constructions and Core Materials, General Test Methods." http://everyspec.com/MIL-STD/MIL-STD-0300-0499/MIL-STD-401B_5654/.

___. 1987. "MIL-HDBK 691B, Military Handbook: Adhesive Bonding." http://everyspec.com/MIL-HDBK/MIL-HDBK-0600-0699/MIL-HDBK-691B_2468/.

___. 2002. "MIL-HDBK-17/2F (Vol 2 of 5) Department of Defense Handbook: Composite Materials Handbook - Polymer Matrix Composites Materials Properties." http://everyspec.com/MIL-HDBK/MIL-HDBK-0001-0099/MIL_HDBK_17_2F_250/.

___. 2021. "DoD Instruction 5000.93 Use of Additive Manufacturing in the DoD." https://www.esd.whs.mil/Portals/54/Documents/DD/issuances/dodi/500093p.PDF?ver=JM7vpZGnbXAFX5uv91rXOQ%3D%3D.

Vectorply. No Date [a]. "E-T 1200." https://vectorply.com/wp-content/uploads/2015/06/ET1200.pdf.

___. No Date [b]. "E-BX 2400." https://vectorply.com/wp-content/uploads/2015/06/EBX2400.pdf.

Zenkert, D. 2005. *An Introduction to Sandwich Structures: Student Edition*. FULLTEXT01.pdf (diva-portal.org).